

**TOWARDS ALL-PRINTED LATERAL FLOW  
BIOSENSORS**

# **TOWARDS ALL-PRINTED LATERAL FLOW BIOSENSORS**

By

YUANHUA LI, B.Eng. M. Eng.

A Thesis Submitted to the School of Graduate Studies  
in Partial Fulfillment of the Requirements  
for the Degree Doctor of Philosophy

McMaster University

© Copyright by Yuanhua Li, July 2019

Ph.D. Thesis – Yuanhua Li          McMaster University – Chemical Engineering  
DOCTOR OF PHILOSOPHY (2019)          McMaster University  
  
(Chemical Engineering)                          Hamilton, Ontario

TITLE:                          Towards All-Printed Lateral Flow Biosensors

AUTHOR:                      Yuanhua Li

B.Eng. (South China University of Technology,  
China)

M.Eng. (South China University of Technology,  
China)

SUPERVISOR: Dr. Robert H. Pelton

NUMBER OF PAGE: ix, 112

## **Lay Abstract**

Many devices in our day-to-day lives incorporate lateral flow biosensors, for example, home pregnancy test kits. These tests allow users to obtain results within 30 minutes by simply applying a few droplets of urine onto a test strip. However, these biosensors are largely manufactured using manual processes: workers cut strips (also called substrates) from sheets, deposit reagents onto the strips, and then assemble the pretreated strips into devices. As such, these processes are time consuming and less productive. To accelerate the manufacturing process, we developed printable porous substrates and a clog-free printing process for depositing expensive reagents onto the substrates.

Novel porous media can be flexibly printed into complex patterns using pigment-based inks. Moreover, the use of different pigments within the designed patterns enables these porous media to control wicking velocity. In addition to printable porous substrates, the research in this thesis shows that the manufacturing process can be improved by using piezoelectric inkjet printers. The use of these printers not only allows the expensive reagents to be precisely deposited onto the substrates, but it also offers a more cost-effective method of doing so. Finally, in order to ensure the printing process remained clog-free, we systematically investigated clogging mechanisms by printing with different polymers and nanoparticles.

## Abstract

Lateral flow biosensors are analytical devices that detect biomaterials with physicochemical signals, such as optical signals. Unlike other biosensors, lateral flow biosensors are based on porous membranes, which use capillary force to transport biomaterials spontaneously. However, lateral flow biosensors are fabricated in batch mode, which means that membranes need to be cut from the rolls, pretreated, and assembled using a step-by-step process. Thus, there is a need for a more efficient manufacturing process. This thesis aims to accelerate the fabrication process by developing a method wherein the whole device is printed directly, including the printable substrates, as well as by developing a clog-free process for depositing expensive reagents.

These novel printable porous media were developed using printing inks that contained various pigments and polymer binders. To this end, candidate formulations were screened from nine hundred inks formulations via wicking experiments. The results of these tests showed that the most promising formulations were based on calcium carbonates and latex polymers. This formulation was then used to develop printable porous media that can easily be printed into complex patterns, with changeable wicking speeds within each pattern. In addition, a bio-colorimetric assay of alkaline phosphates conducted on these porous media showed strong color signals that were comparable to the traditional membrane-based lateral flow strips.

Clog-free printing processes were investigated by using a piezoelectric inkjet printer to print silica sols and six nanoparticle inks. The results of these tests showed that the vibration of the piezoelectric layer and the deposition of particles on the printhead surfaces induced clogging issues. Over time, the silica sols formed multilayer deposits on the print head surface, which subsequently detached due to the vibration of the piezoelectric layer. Consequently, these large sheets of silica clogged the nozzles during printing. This clogging issue was eliminated by adjusting the pH value of the silica sol inks to 3.1. The hydrophobic cationic polystyrene nanoparticles form a sub-monolayer on the printhead surface, which causes air entrainment and promotes air bubble adhesion into the interior of the print head surface when the piezoelectric layer deforms. Thus, alternate surface chemistries for the print head and ink particle surfaces may be required in order to print hydrophobic ink materials. Overall, this enhanced understanding of these clogging mechanisms helps to explain why printer performance varies when different particles are used.

## Acknowledgements

First and foremost, I would like to express my deepest gratitude to my Ph.D. supervisor, Pro. Robert Pelton, for his support, guidance and mentorship throughout my research. Thanks for offering me such a gorgeous opportunity to study and to work with so many world-top scientists at McMaster University. His keen interest and endless passion for research always inspire me to a better scientist. He gave me remarkable freedom and financial support for my research, making me no hesitation to explore the unknown tasks in my work. I'm fortunate to have him to be my supervisor.

I would also like to thank my co-supervisors, also my committee instructors—Pro. Carlos Filipe and Pro. John Brennan. Pro. Carlos Filipe offered me invaluable help and suggestion on my research. His positive attitude encourages me to face difficulties. I would also want to thank Pro. John Brennan that he always provides me excellent suggestions and discussions on sol-gel science and bio-experiments. I'm happy to have them to supervise me during my Ph.D. study.

Furthermore, I would like to thank Pro. Raja Ghosh for letting me be a teaching assistance of his course over three years. He encouraged me to communicate with students and offered me much freedom in tutoring classes. It was valuable experience in my study.

Special thanks to China Scholarship Council for their financial support over the four years, let me start an extraordinary journey in Canada.

I also want to thank Mr. Paul Gatt from Mechanical Technician of the Chemical Engineering Department, for his kindness in helping me prepare samples and customizing experimental designs. As well as Dr. Mehdi Keramane, he always helped me with setting up printers or other instruments. I would also want to thank our laboratory manager Mr. Doug Keller, instrumentation technologist Mr. Michael Clarke, lab technician Mr. Time Stephens, and administrative secretary Ms. Sally Watson for their great help in the past years. I would appreciate an editor Mr. Kris Pikel for his excellent English proofing in my writings. I would also want to thank every staff and technician at Chemical Engineering Department, Biointerfaces Institute (BI), Canadian Centre for Electron Microscopy (CCEM), Electron Microscopy Facility of Health Science for their kindness help.

I would express my gratitude to those who offered me valuable support for my research at McMaster University. Especially to my lab's members including Dr. Songtao Yang, Dr. Zhen Hu, Dr. QiangFu, Dr. Xiaofei Dong, Dr. Carla Abarca, Dr. Dong Yang, Fengyang Wang, Hongfeng Zhang, Gaoyin He, and Xiao Wu. I really

enjoy working with you. I also want to thank my two lovely summer students, Omar Dahhan and Lisa Tran, for their efficient work on this project. I would also want to appreciate all the staffs and students from Pro. Carlos Filipe, Pro. John Brennan, Pro. Shiping Zhu, Pro. Cranston Emily, Pro. Todd Hoare, Dr. Li Xi, Dr. Charles de Lannoy group for their valuable discussions and excellent training.

Many thanks to my friends Fan E, Janice Lao, Lisha Zhao, Hyejin Lee, Qianqian Zhang, Xiaodan Ni, Lingli Liu, Lu Zhu, Dongyang Li, Qun Zhou, *etc.* for spending such wonderful time with me in Canada.

Great thanks to my best friend Dongjun Xuan for her countless support and encouragement. Although we are busy with our own lives, she always comforts me and tells me never to give up.

Finally, I want to share this happiness with my parents, my siblings and my grandparents. Their endless love and support always warm me up through my life.

# Table of Contents

<b>Lay Abstract</b> .....	<b>iii</b>
<b>Abstract</b> .....	<b>iv</b>
<b>Acknowledgements</b> .....	<b>v</b>
<b>Table of Contents</b> .....	<b>vii</b>
<b>List of Abbreviations</b> .....	<b>ix</b>
<b><i>Chapter 1</i></b>	
Introduction and objectives .....	1
Literature review .....	2
1.1 Lateral flow biosensors .....	2
1.1.1 Overview of a lateral flow biosensor .....	2
1.1.2 Assembly of a commercial lateral flow test strip.....	5
1.2 Inkjet printing for fabricating biosensors.....	6
1.2.1 The mechanisms of inkjet printers.....	7
1.2.2 Inkjet printing inks .....	7
1.2.3 Inkjet printing for immobilizing the bioreceptors and reagents.....	8
1.2.4 Inkjet printing for structure patterning on biosensors.....	9
1.2.5 Clogging mechanisms during inkjet printing.....	10
1.3 Porous substrates for lateral flow biosensors.....	12
1.3.1 Nitrocellulose membranes .....	12
1.3.2 Filter papers. ....	13
1.3.3 Wicking behaviors of porous materials .....	14
1.4 Calcium carbonate-based porous structures.....	16
1.5 Objectives .....	18
1.6 Thesis outline .....	19
Reference .....	20
<b><i>Chapter 2</i></b>	
Silica Sol-Gel Inkjet Printing.....	26

Supporting Information .....	35
------------------------------	----

**Chapter 3**

Model Nanoparticle Inks Inkjet Printing .....	45
Supporting Information .....	54

**Chapter 4**

Rapid Screening of Pigments and Binders for Printable Lateral Flow Media.....	63
Introduction.....	64
Experimental .....	64
Results and Discussion .....	68
Conclusion .....	75
Supporting Information.....	77
Acknowledgement .....	82
References.....	83

**Chapter 5**

Printable Porous Substrates for Lateral Flow Media .....	85
Abstract.....	86
Introduction.....	86
Experimental .....	88
Results.....	92
Discussion .....	100
Conclusions.....	102
Acknowledgements.....	102
Supporting Information.....	103
Index Graphic.....	108
References.....	108

**Chapter 6**

My Contributions .....	111
------------------------	-----

---

**List of Abbreviations**

---

---

ATCh	Acetylthiocholine iodide
AChE	Acetylcholinesterase from <i>Electrophorus electricus</i>
ALP	Alkaline phosphatase
AMG-120	Anionic microgel with diameter of 120 nm
APS-28	Anionic polystyrene carboxyl latexes with diameter of 28 nm
APS-530	Anionic polystyrene sulfate latexes with diameter of 530 nm
BCIP	5-bromo-4-chloro-3-indolyl hydrogen phosphate
CI	Color intensity
CMG-450	Cationic microgel prepared with diameter of 450 nm
CPS-510	Cationic polystyrene amidine latexes with diameter of 510 nm
CPS-90	Cationic polystyrene amidine latexes with diameter of 90 nm
DEA	Diethanolamine
DEAW0	Diatomaceous earth, acid washed before calcination, ALMDE-AW
DEAW1	Diatomaceous earth, acid washed before calcination, LOMDE-AW
DEC	Diatomaceous earth, calcinated, Celpure-C100
DEN0	Diatomaceous earth, natural, Celite 221-M
DEN1	Diatomaceous earth, natural, Celpure-C25
DEN2	Diatomaceous earth, natural, ALMDE
DEN3	Diatomaceous earth, natural, LOMDE
DLS	Dynamic Light Scattering
DTNB	5,5'-dithiobis(2-nitrobenzoic acid)
FP	Filter paper
GCC0	Ground calcium carbonate, Covercarb 85
GCC1	Ground calcium carbonate, Hydrocarb 90
LFDs	Lateral flow devices
MCC	Modified calcium carbonate, OmyaJet 5010
NBT	Nitro-blue tetrazolium chloride
NC	Nitrocellulose
PCC0	Precipitated calcium carbonate, Syncarb S160
PCC1	Precipitated calcium carbonate, ViCALity Light
PCC2	Precipitated calcium carbonate, ViCALity ALBAFIL
PCC3	Precipitated calcium carbonate, ViCALity Extra Light
PCC4	Precipitated calcium carbonate, ViCALity Heavy
PE	Polyester
pNPP	p-nitrophenyl phosphate, disodium salt
QCM-D	Quartz crystal microbalance with dissipation monitoring
SSA	Specific surface area
THF	Tetrahydrofuran

---

# *Chapter 1*

## **Introduction and objectives**

---

People are presently living longer and healthier lives than ever before. Indeed, the global life expectancy was 72.0 years as of 2016, which denotes an increase of 5.5 years since 2000, when it was 66.5 years.<sup>1</sup> One of the key reasons for this increase has been the development of effective early disease warning systems and diagnostic tools,<sup>2</sup> such as biosensors. Biosensors are widely used in our daily lives, with applications ranging from food-quality testing,<sup>3</sup> to health monitoring,<sup>4 5</sup> to the detection of environmental contamination.<sup>6</sup>

Compared to traditional analytical techniques, which are time consuming and difficult to operate, biosensors are speedy and simple. Thus, the global biosensor market is projected to exceed more than US\$ 26 billion by 2022.<sup>7</sup>

Lateral flow biosensors are commercially promising for two main reasons: (1) they can be fabricated using traditional materials (e.g., nitrocellulose membrane, paper sheets),<sup>8</sup> and (2) they can be patterned using techniques such as screen printing,<sup>9</sup> lithography,<sup>10</sup> and inkjet printing.<sup>11</sup> Inkjet printing is a particularly useful technique because it is flexible, low cost, and efficient.<sup>11</sup> However, in order to ensure a reproducible fabrication process, it is critical that the inkjet printing process be clog-free. This is particularly important for commercial products.<sup>12</sup> Unfortunately, in addition to being expensive, inkjet print heads have a high clogging-potential.<sup>13</sup> Thus, it is necessary to understand and remedy the sources of clogging if inkjet printing is to be meaningfully applied for the mass production of biosensors. This chapter begins with a discussion of the background of lateral flow biosensors before moving on to an overview of inkjet printing's various applications in relation to biosensor fabrication, as well as the associated challenges.

In general, the mass-production of commercial lateral flow devices is time consuming, as it requires the use of a discontinuous process.<sup>12</sup> As such, a process that would allow the substrate to be fabricated and patterned simultaneously would be highly attractive. Therefore, the second objective of this chapter is to review the properties of existing porous substrates in order to identify the most promising porous media, consisting of pigments, for use as a substrate in lateral flow biosensors.

## Literature review

### 1.1 Lateral flow biosensors

Biosensors are analytical tools that detect physiochemical signals created by biological components. Through specific conjugations between bioreceptors or biomolecules (e.g., proteins, enzymes, antibodies) and analytes, transducers transform signals into physiochemical signals, such as optical, electrochemical, and piezoelectric signals.<sup>14</sup> Decades of development have resulted in the availability of simple, easy-to-use biosensors that can be used in a broad range of fields, including healthcare, food safety, and environmental science.<sup>15</sup>

Since biomolecules are expensive<sup>16</sup> and sample volumes tend to be limited, researchers have focused on miniaturizing biosensors in order to lower the costs associated with materials and manufacturing.<sup>17</sup> Molecules are transferred to target zones along small channels using syringe pumps,<sup>18</sup> electrolytic force,<sup>19</sup> or capillary force.<sup>20</sup> Unlike syringe pumps or electrolytic force, which require the use of external devices, capillary force is provided naturally by porous media, such as soil, membranes, or paper sheets.<sup>21</sup> As a result, lateral flow biosensors function via capillary-driven microfluidics.<sup>22 23 24</sup>

#### 1.1.1 Overview of a lateral flow biosensor

A classic lateral flow immunoassay biosensor is shown in Figure 1 - 1. As can be seen, lateral flow biosensors consist of four components.<sup>25 26</sup> A **sample pad**, which stores and transfers liquid analyte mixtures. A **conjugate pad**, which stores labeled (e.g., gold nanoparticle) antibodies that have a specific conjugation with the analytes. Analytes and antibodies form bound structures that continue to migrate along the strip to the **reaction pad**. The reaction pad is patterned with a test line and a control line. A positive result is indicated by optical or fluorescent signals on the test line where the immobilized antibodies on the membrane surface interact with bound structures. Meanwhile, the excess bound structures move forward to the control line that contains immobilized anti-antibodies. Since these anti-antibodies did not interact with bound structures, the optical or fluorescent signals are differed to signals in the control line. Thus, the control line is used to indicate negative result. The final component of the lateral flow biosensor is the **wicking pad**, which is responsible for wicking all of the analytes through the reaction pad.

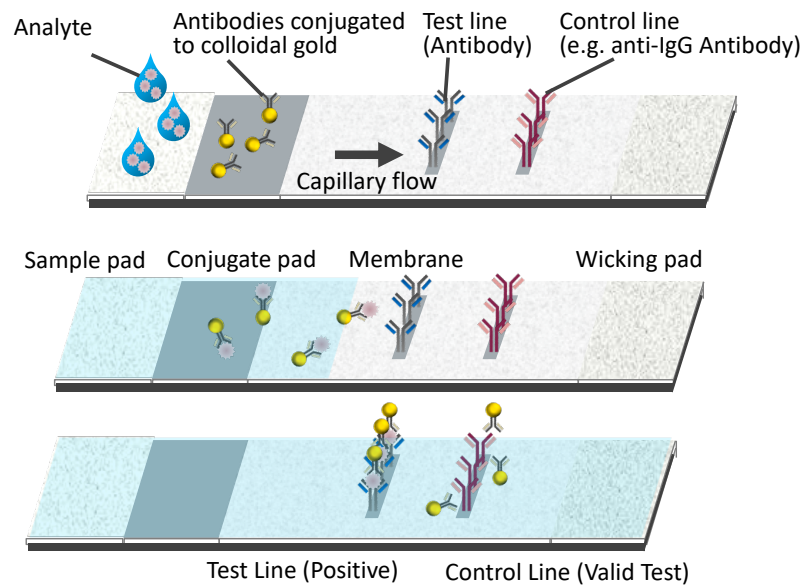


Figure 1 - 1. I Illustrative graph of a classic lateral flow immunoassay. Modified from Ref.<sup>26</sup>

Since the EMD Millipore Company is the primary producer of nitrocellulose membranes for lateral flow biosensors, our discussion of the key aspects of test strip design and device assembly will be based on a Millipore model strip.<sup>27 28 29</sup> A brief structural schematic for an EMD Millipore commercial lateral flow immunoassay test strip is provided in Figure 1 - 2.

### 1.1.1.1 Membrane

The membrane plays the most important role in a lateral flow strip, as it is where the signal is observed by users. Reagents and bioreceptors are immobilized onto the surface, forming as a test line and a control line. Conjugated analytes flowing through the membrane are captured by the bioreceptors on the test line, producing signals. Thus, another function of this membrane is to provide enough wicking ability to transport the analytes. The capillary flow rate is influenced by a number of membrane parameters, such as pore size, pore size distribution, and porosity. EMD Millipore currently offers 5 types of nitrocellulose membrane, HF180, HF135, HF120, HF090, and HF075, where the number represents sec/4 cm.

The capillary rate affects signal generation by controlling the amount of time the moved analytes come into contact with the immobilized bioreceptors on the test line. Because test strips only have one direction of flow, the analytes cannot bind onto immobilized bioreceptors once they pass the test line. Thus, for a good signal generation, users need to choose a suitable flow-rate membrane and optimize the

position of the test line. For example, a ‘slower’ nitrocellulose membrane (e.g., HF180) is ideal for high sensitivity tests.

The membrane consists of nitrocellulose and nitrocellulose/cellulose acetate, resulting in a hydrophobic surface, and the addition of detergents and surfactants during the production process allows the membranes to wet easily in aqueous solutions. During production, the membrane can be cast onto a polyester film, which provides higher mechanical strength and prevents membrane breakage during routine operation. For lateral flow tests, the membrane usually cut into straight sections using a Guillotine cutter.<sup>30</sup>

### **1.1.1.2 Sample pad**

The sample pad ensures that the analytes are evenly distributed to the conjugate pad and prevents the overflowing of samples in the device.

Cellulose fibers and woven meshes are the most commonly used materials in sample pads. Aside from even sample distribution, woven meshes provide the advantage of good tensile strength, which allows them to retain their shape after cutting and packaging. However, woven meshes are limited by their low hold-up volume, normally 1-2  $\mu\text{L}/\text{cm}^2$ , which may not allow sufficient sample transfer to the test line. Hence, cellulose fibers are more commonly used, as they are less expensive and offer larger hold-up volumes of up to 25  $\mu\text{L}/\text{cm}^2$ .

During production, sample pads are pretreated with blocking agents via dipping in order to eliminate binding between analytes and the membrane. Since sample pads become weak after dipping, it is important to handle wet sample pads with care and to allow them to dry before cutting.

### **1.1.1.3 Conjugate pad**

The analytes interact with detector reagents (e.g., gold nanoparticle) on the conjugate pad before being transferred to the membrane. The amount of conjugated complex that is ultimately transferred to the membrane is what determines the biosensor’s sensitivity. Thus, the ideal conjugate pad should offer low non-specific binding, consistent flow rate, and good web handling. As such, treated glass fibers (less expensive) and cellulose filters are the most commonly used materials for conjugate pads, as they provide low nonspecific binding and good tensile strength.

During the production process, conjugate pads are dipped into buffers and held up in order to reduce excess liquid. After the excess liquid has been allowed to drain, the wet pad is carefully placed on a nonabsorbent surface to dry. Once dried, the pads can be cut into strips.

### 1.1.1.4 Absorbent pad

The absorbent pad, or wicking pad, increases the volume of liquids transported through the test strip. These extra liquids are useful because they wash unbound conjugated analytes away from the membrane, thus lowering the background signal. However, optimal sensor functionality can be achieved through proper test designs, for example, using a longer membrane or positioning the test line closer to the conjugate pad. Thus, an absorbent pad is not mandatory for a test strip; to lower the cost of a finished strip, users can simply use inexpensive cellulose fibers. Since there is no specific need to incorporate an absorbent pad, it can be cut directly from the list of required raw materials.

### 1.1.1.5 Housing

Commercial lateral flow strips are installed in a plastic housing, which protects the rest of the strip from exposure to the sample. To ensure easy-to-read test results, manufacturers can label the positions of test line and control line on the plastic housing. However, plastic housings must be biocompatible, as they use internal pins to hold the strip, thus making contact with it inevitable.

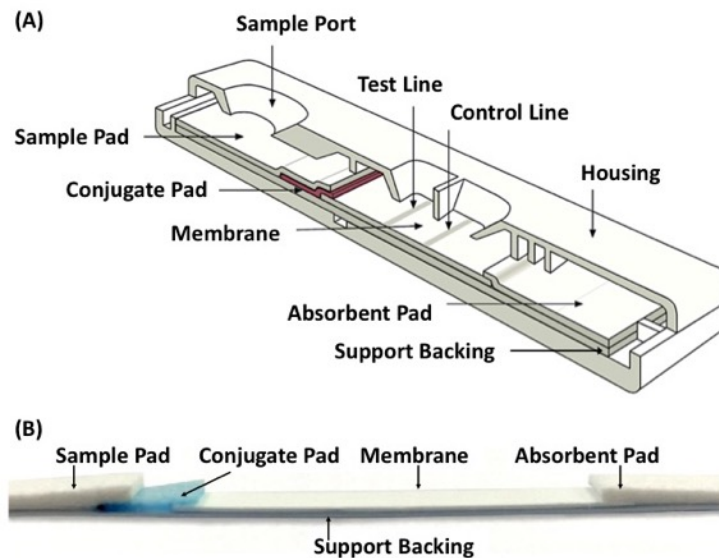


Figure 1 - 2. (A, B) Schematic image of a commercial lateral flow test device. Adapted for Ref.<sup>27 29</sup>

## 1.1.2 Assembly of a commercial lateral flow test strip

Table 1 - 1 lists the preparation process for each part of the test strip. In order to functionalize the device, the membrane, conjugate pad, sample pad, and absorbent pad must be aligned sequentially on an adhesive card (Figure 1 - 3), which consists

of a plastic support, an adhesive layer, and a release liner. To ensure a continuous flow during the test, these pads are aligned in a partially overlapping manner. The scored release line helps the user to position the pads and membrane.

After alignment, the pads or membrane are fastened to the adhesive card using a lamination process. This pressure created by this process helps to bind the pads to the card and to reduce the space between them. Once the lamination process has been completed, the card can be cut into individual strips and secured in a plastic housing.

Table 1 - 1.      Brief summary of the preparation process used for each part of a commercial lateral flow test strip.

	Materials	Preparation
Membrane	Nitrocellulose membrane	Cut
Sample pad	Cellulose filter or woven mesh	Dip into buffer, dry, and cut
Conjugate pad	Glass fiber	Dip into solution, dry, and cut
Absorbent pad	Cellulose filters	Cut
Housing	Biocompatible plastic	Customer design

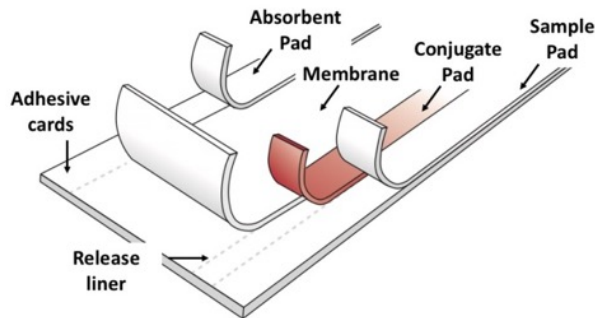


Figure 1 - 3.      Schematic for laminating pads on an adhesive card. Adapt from Ref. <sup>27</sup>

## 1.2 Inkjet printing for fabricating biosensors

As noted above, the membrane is the most important component of a lateral flow strip, as it is where the test line, which consists of bioreceptors and other reagents, is located.<sup>27</sup> It is important to ensure that the bioreceptors are not washed off of the test strip when the fluid containing the labeled analytes particles flows through it. However, since test lines are often only 1 mm to a few millimeters wide,<sup>27</sup> the volume of the deposited solution with bioreceptors is usually small. Assuming a 135  $\mu\text{m}$  x 5 cm nitrocellulose membrane with 70% porosity, the volume of liquid required to fill a 1 mm width pattern would be 2  $\mu\text{L}$ . Thus, it is critical to select a

technique that is capable of accurately depositing these materials. One technique that has been used by many researchers in biosensor production is inkjet printing, which can print pico-sized droplets.<sup>11, 31-33</sup>

### 1.2.1 The mechanisms of inkjet printers

While there are a variety of inkjet printers available in the market,<sup>34</sup> this chapter will only focus on the drop-on-demand (DOD) piezoelectric inkjet printer. DOD piezoelectric inkjet printers operate via pressure difference, which is produced by the deformation of a piezo-ceramic material (see Figure 1 - 4).<sup>35</sup> The deformation process involves vibrating the thin layer (~500 μm) of piezo-ceramic material, known as lead zirconated titanate, under an electric pulse for few hundred μs, thus resulting in a high printing frequency (1-100 kHz).<sup>13</sup> The volume of an ejected ink droplet can reach to few picolitres.<sup>36</sup>

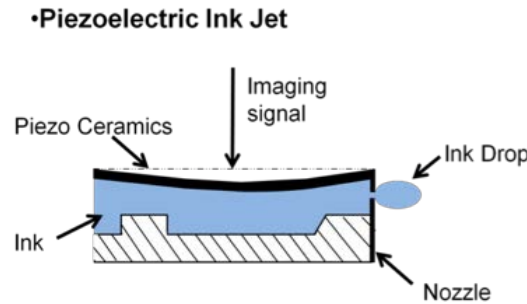


Figure 1 - 4. Overview of a piezoelectric drop-on-demand inkjet printer. Modified from Ref.<sup>11</sup>

### 1.2.2 Inkjet printing inks

The properties of an ink largely determine printing quality and the reproducibility of the printing system. Inks primarily consist of target printing materials (e.g., enzyme, protein, DNA) and additives (e.g., surfactant, viscosity modifiers, humectants), which serve to adjust the ink's surface tension and viscosity and to ensure good printability. An ink's printability can be assessed by analyzing three critical parameters: Reynolds number (Re), Weber number (We), and Ohnesorge number (Oh). Printability is often expressed as a Z parameter that is based on these three dimensionless physical parameters<sup>34</sup>:

$$Z = \frac{1}{Oh} = \frac{Re}{\sqrt{We}} = \frac{\frac{\rho u L}{\eta}}{\sqrt{\frac{\rho u^2 L}{\gamma}}} = \frac{\sqrt{\gamma \rho L}}{\eta} \quad \text{Equation 1 - 1}$$

Where  $\rho$  is the density of a fluid (kg/m<sup>3</sup>),  $u$  is the velocity (m/s),  $\gamma$  is the surface tension (N/m), and  $\eta$  is the dynamic viscosity of a fluid (Pa·s).

When the value of  $Z$  is too low, droplets will not be ejected due to energy dissipation in the nozzle; when the value of  $Z$  is too high, satellite droplets will form. As a general rule, stable ink jetting can be achieved by ensuring that the value of  $Z$  is between 1 and 14,<sup>37</sup> but this has been questioned by researchers such as Lee *et al.*, who have suggested that the printable range for ZnO nanoparticles is  $2.5 < Z < 26$ <sup>38</sup>, and Reis *et al.*, whose findings suggested that  $Z$  values between 1 and 10 may be more suitable.<sup>39</sup>

### 1.2.3 Inkjet printing for immobilizing the bioreceptors and reagents

Enzyme-immobilization methods fall into one of two categories: physical entrapment or chemical attachment.<sup>40-42</sup>

Sassolas *et al.*<sup>40</sup> conducted a thorough review of enzyme-immobilization approaches that included: (1) entrapment in a three-dimensional matrix, such as gel or polymer; (2) adsorption with solid support via physical forces (e.g., electrostatic interaction); (3) covalent bonding to a polymeric substrate; (4) cross-linking to glutaraldehyde or inert proteins; (5) affinity binding between a protein sequence (e.g., biotin) and a functional group (e.g. avidin).

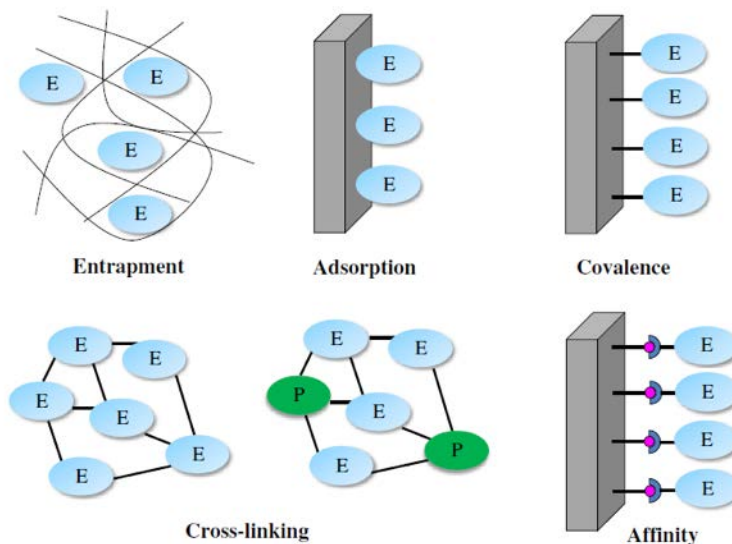


Figure 1 - 5. Different enzyme-immobilization methods. E: enzyme; P: inert protein. This figure is adapted from Ref.<sup>40</sup>

Brennan's group used a sol-gel-derived matrix to physically entrap enzymes on a paper structure in their successful development of a paper-based biosensor that is able to detect pesticides, heavy metals, and *E. coli*.<sup>41, 43-44</sup> First, they used piezoelectric inkjet printer to print an initial layer of a cationic polymer in order to

transform the paper's surface from anionic to cationic. Next, they printed a layer of silica sol onto the cationic layer where immobilized the silica sol layer via electrostatic force. Once this had been done, another liquid layer of biomolecules was printed onto the silica sol layer, which was followed by the application of a final layer of silica sol. These silica sol-gel layers encapsulate the biomaterials by controlling the polymerization of silica sol in pH condition.

When the pH is between 2 and 7, the monomer of aqueous silicates first hydrolyses with the product of water to form particles; these particles then link into chains before finally gelling into a porous three-dimension network,<sup>45</sup> which entraps the enzymes. The entrapped enzymes form a sandwich-like structure that enables excellent colorimetric assays without enzyme leaching. Furthermore, their work also revealed that, in addition to entrapping enzymes, thin sol-gel layers also protected the enzymes from denaturization in the cationic layer and oxidization from the ambient environment.

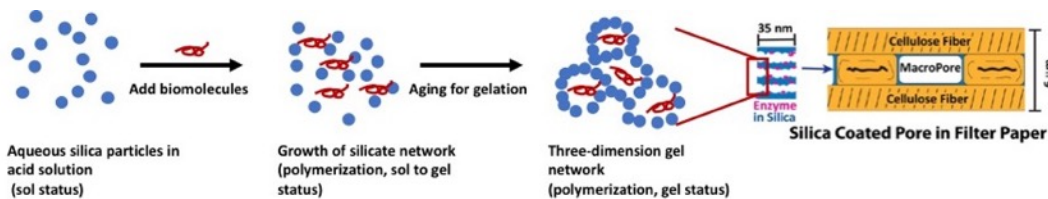


Figure 1 - 6. Entrapment of biomolecules within a silica-sol-gel 3-D structure on a filter paper. Modified from Ref.<sup>41</sup>

### 1.2.4 Inkjet printing for structure patterning on biosensors

When developing a lateral flow biosensor, it is necessary to functionalize the sensor so that multiple tests can be integrated on one strip. To achieve this, different lateral flow channels must be created on the filter paper or nitrocellulose membrane. There are two common methods for creating channels on a substrate: separating the channels by printing chemical barriers (e.g., hydrophobic polymers),<sup>46-47</sup> or mechanically cutting the channels.<sup>48-49</sup>

Unlike the cutting technique, which usually requires an experienced technician, inkjet printing with hydrophobic inks is easy, requires no particular expertise, and can be used to design and print customize patterns onto a substrate.<sup>50-52</sup> Wax is commonly used as a hydrophobic ink because the low cost (~\$900/ton) and simple printing treatment that wax melts when heated (>120°) then solids at room temperature.<sup>33</sup> Carrilho *et al.* used a Xerox Phaser 8560N color printer to apply wax to chromatography paper in order to create complex microfluidic channels. The Xerox Phaser 8560N ejects liquid wax as 50-60 μm droplets, forming an effective hydrophobic barrier less than 300 μm width. This printing process is efficient and can print full wax patterns onto an 8.5 x 11-inch sheet in approximately 5 min.<sup>50</sup>

Jingyun *et al.* used piezoelectric inkjet printing to explore the performance of 3 hydrophobic barriers: wax, alkyl ketene dimer (AKD), and sol-gel-derived methysilsesquioxane (MSQ).<sup>51</sup> The wax barriers were printed using a wax printer (Xerox Phaser 6580), the AKD ink was printed using a Canon PIXMA MP280 inkjet printer, and the MSQ ink was printed using a Dimatix inkjet printer. Three rectangular (7.5 x 30 mm) were patterned on filter papers by these printed barriers of three polymers (1.5 mm wide).

Although three barriers performed well for aqueous solutions, the MSQ barrier was the only one capable of maintaining its performance in cell lysing solutions and surfactant solutions (e.g., Triton X-100, CTAB, SDS).

In addition to printing hydrophobic polymer on nitrocellulose membranes and filter paper, Koivunen *et al.* used an inkjet printer (Dimatix 2800) to print barriers of polystyrene and AKD onto calcium carbonate coated surfaces where multiple parallel channels were separated by hydrophobic barriers.<sup>52</sup> By printing different amounts of hydrophobic polymers, they were able to change the rate of wicking. Koivunen *et al.* also used an inkjet printer (Dimatix 2800) to print polystyrene and AKD hydrophobic barriers onto a porous functionalized calcium carbonate coating surface.<sup>52</sup> The patterned hydrophobic widths ranged from 0.5 to 1.0 mm, while the channels ranged from 0.2 to 2 mm.

## **1.2.5 Clogging mechanisms during inkjet printing**

A typical piezoelectric printhead has a total ink-channel length of 5–20 mm and an orifice width of 0.01–0.05 mm.<sup>13</sup> As such, piezoelectric printers can encounter problems with clogging, depending on the material being printed.<sup>38 41 52</sup> Prior studies on printhead clogging<sup>53-58</sup> have identified 4 main causes: **(1) filtration; (2) jamming; (3) deposition; and (4) air bubbles.**

**Filtration** refers to channel blockage that occurs when the size of a regular particle or the geometry of anisotropic particles exceed width of the microchannels (shown in Figure 1 - 7 (A)). This is especially common with regular particles, such as polystyrene and silver particles, as they will block the channel if their particle-size diameter exceeds the width of the channel.<sup>59</sup> For these particles, blockage problems can be remedied by sieving or filtering the large particles. Similarly, anisotropic rigid particles will cause clogging if one of the particle dimensions exceeds the size of a channel.<sup>60</sup> This problem can be mitigated by controlling the orientation of the particles as they flow through the channel.

**Jamming** occurs when the volume fraction of a colloidal stable dispersion reaches its jamming limit, thus causing a bridge-like structure in particle flow (Figure 1-7 (B)).<sup>61</sup> Since the particle/particle and particle/wall<sup>61</sup> interactions are repulsive under this situation, the bridge structure is fragile that can only withstand large forces in

a direction. As such, jamming can be prevented by changing the fluid direction, such as using rotating vortices.<sup>62</sup>

**Aggregation** refers to the clumping of particles, which can occur via deposition or adsorption onto surfaces in stable and unstable suspensions. In view of the aggregation caused by self-assembly of colloidal particles present at high concentrations, as they are close to each other that they aggregate due to the attractive van de Waals forces.<sup>63</sup> In dilute suspensions, the aggregation occurs when particles first deposit on walls, followed by successive deposition between particles and walls, driven by van der Waals forces, gravitational and hydrodynamics forces.<sup>64</sup>

**Air bubbles** from the nozzle plate can cause a piezoelectric oscillated inkjet printer to stop printing.<sup>65-68</sup> If air bubbles are not expelled from the printhead, they will keep growing due to rectified diffusion<sup>69</sup> and eventually block the flow of ink. A series of papers from the Netherlands has documented detailed experimental and computation studies of air inhalation from the nozzle plate of a piezo-driven inkjet printer.<sup>65-68</sup> These studies found that air bubble retention is promoted by the formation of an ink film on the nozzle plate. The same group also reported that air entrainment was influenced by the presence of dispersed ink particles on the print head.<sup>66</sup>

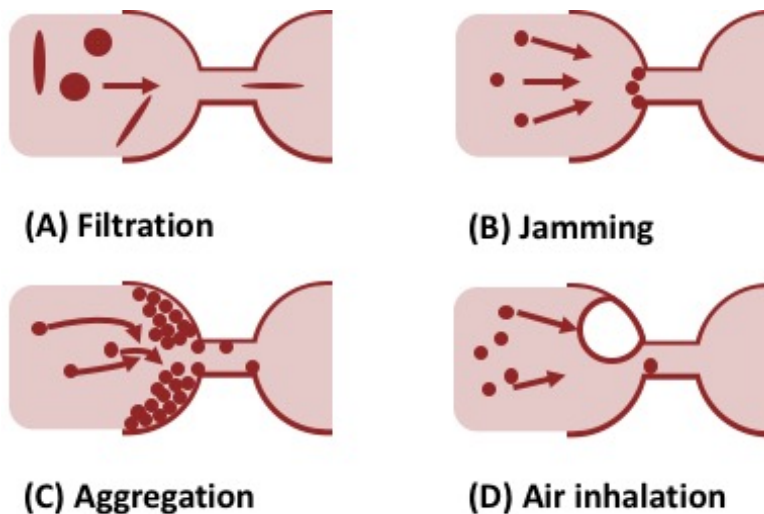


Figure 1 - 7. Different clogged mechanisms of a microchannel at a constriction. Modified from Ref.<sup>53 70</sup>

### 1.3 Porous substrates for lateral flow biosensors

Nitrocellulose membranes are the most commonly used membrane for commercial lateral flow test device (e.g., pregnancy test strip<sup>71-72</sup>), while filter paper or chromatography paper are most commonly examined in academic publications.<sup>27</sup>

#### 1.3.1 Nitrocellulose membranes

Nitrocellulose membranes are cellulose nitrate that cellulose treated with nitric acid, which replaces the cellulose hydroxyl groups with nitrate groups, turning cellulose into cellulose nitrate.<sup>73-74</sup> The nitrocellulose membrane is produced by dissolving nitrocellulose in an organic solvent, which is evaporated in a nonsolvent liquid, resulting in a precipitated and porous nitrocellulose membrane (see Figure 1 - 8).<sup>75</sup> Since nitrocellulose is naturally hydrophobic, surfactant and detergent are introduced during the manufacturing process.

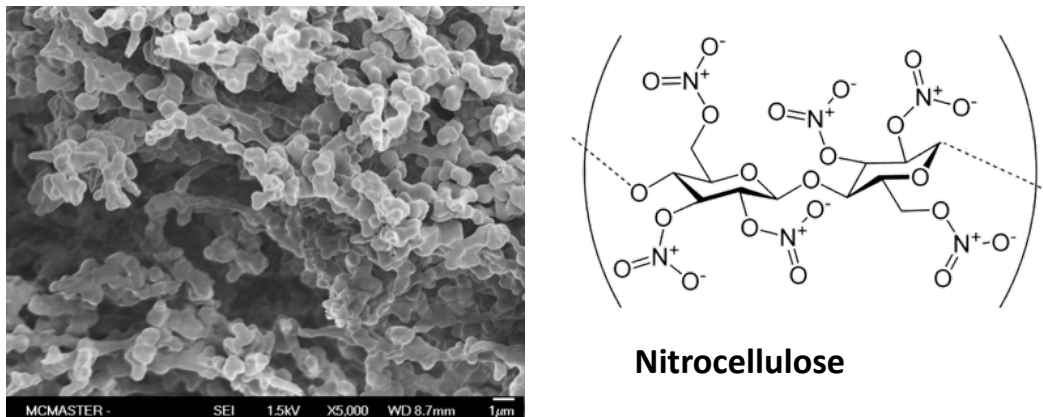


Figure 1 - 8. An SEM image of a nitrocellulose membrane (HF18002, EMD)

The EMD Millipore Corporation is the main manufacture of nitrocellulose membranes. By controlling the solvents, evaporation rate, temperature, and humidity during membrane production, the Millipore Company has developed 5 Hi-Flow™ plus nitrocellulose membranes with different porosities and pore sizes for lateral flow tests.<sup>28</sup> Specifically, the 5 developed membranes are the HF075, HF090, HF120, HF135, and HF180, where the number represents the sec/ 4cm wicking rate. The sensitivity of these membranes increases from HF075 (lowest) to HF180 (highest).<sup>27</sup>

The Sartorius Stedim Biotech Company is another cellulose membrane manufacturer that is noted for its UniSart® nitrocellulose membranes.<sup>76</sup> Besides offering nitrocellulose membranes with different capillary speeds, named UniSart® CN membranes, this company has designed a novel strip engraved with multiplex channels, as shown in Figure 1 - 9. This multiplex-patterned test strip, known as the

UniSart StructSure® membrane, fulfills the goal of being able to test several targets with one device.

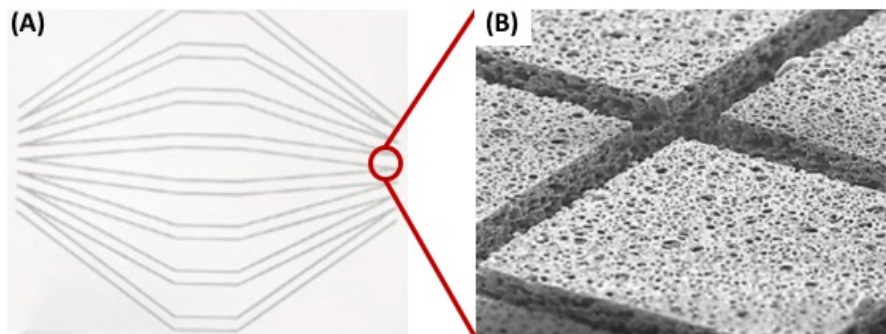


Figure 1 - 9. (A) Image of a multi-channel UniSart StructSure membrane. (B) An image of patterns cut into a UniSart StructSure® membrane. Adapted from Ref.<sup>76</sup>

### 1.3.2 Filter papers.

Paper is a natural, three-dimensional, porous, composite material that is mainly comprised of cellulose fibers. Cellulose fibers are hollow tubes that are typically 1-3 mm long, 3-5  $\mu\text{m}$  thick, and have a circular cross section that is 20-30  $\mu\text{m}$  in diameter.<sup>77</sup> Cellulose is a polysaccharide consisting of  $\beta$ -1,4 linked glucose units<sup>78</sup> (Figure 1 - 10), and it is this high density of hydroxyl groups that gives filter paper its hydrophilic qualities. In an attempt to capitalize on this porous structure and the hydrophilic surface, VTT (a research organization in Finland) explored the use of filter paper as a substrate of bioactive-paper.<sup>22</sup> This seminal research was built upon by Whitsides's group at Harvard University<sup>10</sup> and Pelton's group at McMaster University,<sup>20</sup> both of whom tested the efficacy of filter paper for lateral flow bioassays.

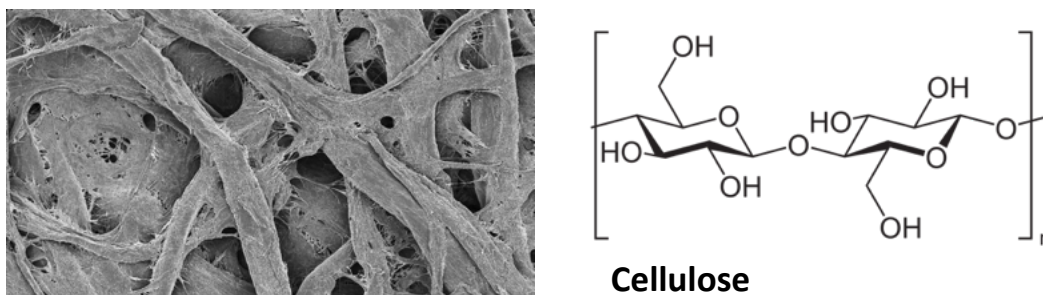


Figure 1 - 10. An SEM image of a filter paper (Whatman #1 filter paper).

### 1.3.3 Wicking behaviors of porous materials

Porous materials are used as substrates in lateral flow devices because their natural wicking ability eliminates the need for an external pump. This advantage makes lateral flow biosensors attractive compared to other biosensors, such as electric field-driven immunosensors.<sup>79</sup> Indeed, this wicking behavior is critical for completing tests with a lateral flow biosensor. The wicking behavior of a fluid relates to its characteristic (e.g., viscosity, surface tension), the porous structure, and the contact angle of the liquid on the solid surface.<sup>21 80</sup>

**Viscosity of a liquid.** In Newtonian fluids, the dynamic viscosity is the ratio of the shear stress between two walls to the rate of shear velocity (Figure 1 - 11 (A) and Equation 1 - 2. ), expressed as the derivative of a liquid speed in the direction perpendicular to the plates.<sup>81</sup> An increased viscosity can increase friction resistance, which will result in a slower wicking velocity.

$$\tau = \mu \frac{\partial u}{\partial y} \quad \text{Equation 1 - 2}$$

Where,  $\mu$  is the viscosity of the fluid, Pa • s,  $\tau$  is the shear rate, and  $\frac{\partial u}{\partial y}$  is the local shear velocity.

**Surface tension of a liquid.** Surface tension is the net result of intermolecular liquid-liquid attraction and air-liquid interface attraction (Figure 1 - 11 (B)). Surface tension can be defined as the increased Gibbs free energy that accompanies an increased surface area. This relationship is expressed as,<sup>82</sup>

$$\gamma = \left[ \frac{\partial G}{\partial A} \right]_{T,V,n} \quad \text{Equation 1 - 3}$$

Where,  $\gamma$  is the surface tension of the liquid, mJ/m<sup>2</sup>,  $G$  is the Gibbs free energy, mJ,  $A$  is the surface area, m<sup>2</sup>,  $T$  is the absolute temperature, K,  $V$  is the total volume, m<sup>3</sup>, and  $n$  is the number of molecules.

**Contact angle** can be calculated from the sum of the interfacial tensions applied on the contacting line (also called triple line, Figure 1 - 11 (C)). This triple line is obtained from three phases: liquid (L), solid (S), and the gas (G). As such, the sum of these equilibrium forces on the triple line can be expressed as Equation 1 – 4, also known as Young’s relation:<sup>83</sup>

$$\gamma_{SG} - \gamma_{SL} - \gamma_{LG} \cos\theta = 0 \quad \text{Equation 1 - 4}$$

Where  $\gamma_{SG}$ ,  $\gamma_{SL}$ , and  $\gamma_{LG}$  represent the interfacial energy of solid-gas, solid-liquid, and liquid-gas, respectively, and  $\theta$  is the measured contact angle.

**Porosity and effective pore size** are the two main properties of porous media. Porosity refers to the ratio of the volume of empty or void space to the total volume.<sup>84</sup> Effective porosity, which refers to the ratio of the volume of connecting voids over the total volume, is more meaningful for wicking flow<sup>84</sup> because it relates to the total volume of liquid absorbed by the porous structure. The effective pore size is obtained through experiments<sup>85</sup> wherein the micropore ( $d < 2$  nm) and mesopore ( $2 \text{ nm} < d < 50$  nm) are measured with a Brunauer–Emmett–Teller (BET) machine,<sup>86</sup> and the macropore ( $d > 50$  nm) is measured via mercury porosimetry.<sup>87</sup>

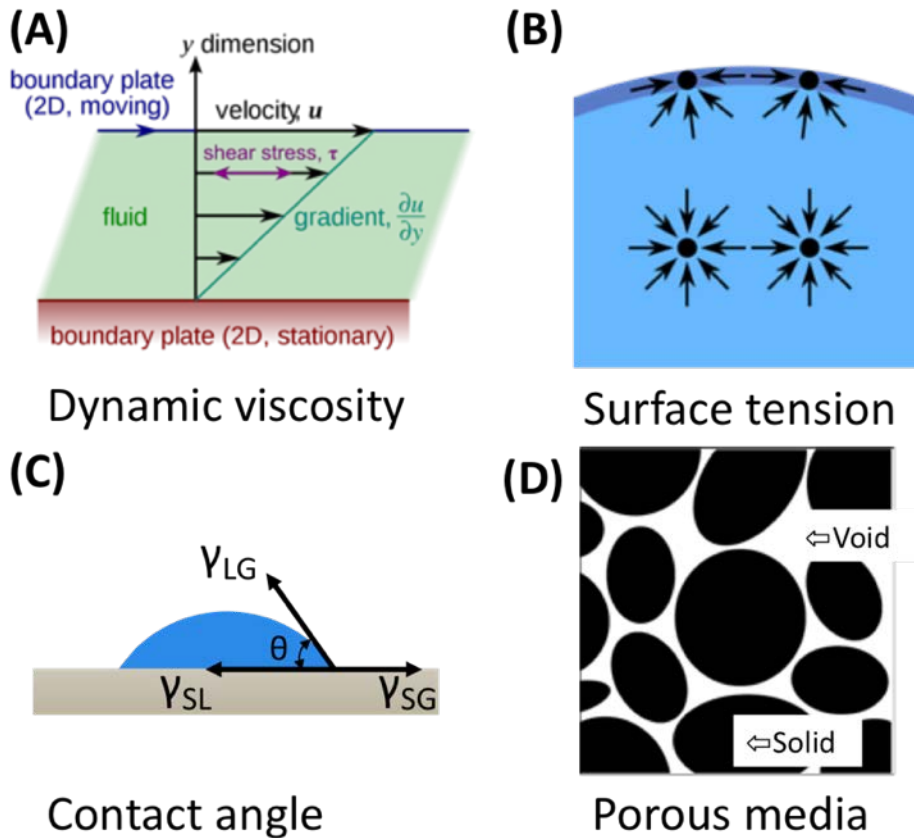


Figure 1 - 11. Illustration of the properties of the wicking fluid: (A) the viscosity of the fluid; (B) the surface tension of the liquid; (C) the liquid contact angle on the solid surface. (D) porosity and pore size, which constitute the properties of the porous media

### 1.3.3.1 The Lucas-Washburn equation

The application of the Lucas-Washburn (LW) model<sup>88</sup> to calculate the fluid wicking distance into a dry porous media is based on the following assumptions or facts:

1. Although most porous media are tortuous, they are most approximated as a bundle of straight pores.<sup>74</sup>
2. In porous media, where most of the Reynolds numbers are  $\sim 10^{-3}$ , flow is laminar.<sup>89</sup>

3. Since little solution is imbibed within the structure, the effect of gravity is negligible.
4. Fluid evaporation is ignored.
5. The boundaries do not exert any effect.

Thus, the LW model can be expressed as follows:

$$L = \sqrt{\frac{\gamma r \cos\theta}{2\mu}} t \quad \text{Equation 1 - 5}$$

Where,  $L$  is the length of fluid migration into the porous media,  $m$ ,  $\gamma$  is the vapor–liquid interface tension,  $N/m^2$ ,  $r$  is the effective pore radius,  $m$ ,  $\theta$  is the contact angle,  $\mu$  is the fluid dynamic viscosity,  $Pa \cdot s$ , and  $t$  is the time,  $s$ .

### 1.3.3.2 Darcy's law

When the porous media is fully wetted, Darcy's law governs the laminar flow in a given porous media, and is expressed by Equation 1 – 6<sup>90</sup>:

$$Q = -\frac{\kappa A \Delta P}{\mu L} \quad \text{Equation 1 - 6}$$

Where,  $Q$  is the total volumetric flow rate,  $m^3/s$ ,  $\kappa$  is the intrinsic permeability of the porous medium,  $m^2$ ,  $A$  is the cross-sectional area of the flow,  $L$  is the length of the fluid flows through the media,  $m$ ,  $\Delta P$  is the pressure drop over that length,  $Pa$ , and  $\mu$  is the fluid dynamic viscosity,  $Pa \cdot s$ .

Both the LW model and Darcy's law have been widely used to demonstrate the wicking behavior of fluids in paper and nitrocellulose-based biosensors.<sup>91-96</sup>

## 1.4 Calcium carbonate-based porous structures

While reading the literature on producing lateral flow biosensors, we realized that neither nitrocellulose membranes nor filter papers are ideal substrates. For example, it has been reported<sup>27</sup> that only the top 10  $\mu m$  layer of nitrocellulose membranes contribute to the generation of a visual signal. The typical thickness of a nitrocellulose membrane or a filter paper is  $\sim 180 \mu m$ ,<sup>97</sup> which means  $\sim 80\%$  volume of the porous media does not contribute to signal generation and unnecessary increases the volume of sample needed as well as the volume of expensive solutions containing the biomolecules needed to run the assay. In addition, the velocity of liquid is constrained by having a uniform porosity throughout the nitrocellulose membranes or filter papers<sup>27</sup> - to provide additional level of spatial control over velocity profiles, researchers have resorted to printing various polymers on substrates,<sup>98</sup> or by folding the substrates,<sup>99</sup> which require an additional step in the fabrication process. Thus, the development of new media for

a lateral flow biosensor is a necessary and attractive endeavor. This media should feature a porous structure, be composed of low-cost biocompatible materials, and easy to fabricate.

Calcium carbonate is one strong candidate, as it can be fabricated to have a porous structure, which allows it to use capillary force to transport molecules. This medium has been used for applications such as calcium-carbonate-coated paper and calcium-carbonate thin-layer chromatography.<sup>100</sup> Calcium carbonate is also abundant in nature or can be easily produced as precipitations, thus making it low cost. Furthermore, calcium carbonate is commonly used as an additive in food and medicine,<sup>101-102</sup> which indicates that it is biocompatible.

Gane's group from Aalto University has extensively studied ink absorption on calcium-carbonated-coated papers and have recently turned their focus to the application of calcium carbonates in biosensors.<sup>103-110</sup> Specifically, they tested their 'Pore-Cor' model using a mercury intrusion porosimetry instrument in order to simulate ink absorption in a ground calcium-carbonate-based coating (Figure 1 - 12 (A)). They visualized the wetting process using a three-dimensional structure constructed with cylindrical tubes, which represented the calcium-carbonate particles and the connective pores between them.<sup>103-104</sup> Later, a modified 'Por-Cor' model was developed by rebuilding the three-dimensional structure using connected double-conical shapes. This updated model was able to simulate and predict the absorption of ink onto these porous calcium-carbonate coating structures.<sup>105</sup> Gane *et al.*'s work emphasized how the inertial force of printing inks impacts overall ink absorption, such that the fine pores increase ink absorption in the first few milliseconds. After this initial period, however, overall ink absorption depends on the permeability of the coating structure.<sup>106</sup>

Realizing the function of these fine pores, Gane *et al.* then modified the ground calcium-carbonate surface into a nano-dimensional structure (see Figure 1 - 12 (B)). These modified calcium-carbonates particles allowed them to create bi-modal pore-size-distribution structures, wherein the fine pores accelerated ink absorption over a short period of time, and the larger pores increased overall permeability.<sup>106</sup>

When applied on coating paper, these calcium carbonates need a binder (e.g., polyvinyl alcohol, latex binders) in order to bind to the paper surface. In a subsequent study, Lamminmaki, a member of Gane's group, studied liquid flow in porous structures—constructed from paper, calcium carbonates, and binders—during the inkjet printing process.<sup>108</sup> She concluded that swellable binders, such as polyvinyl alcohol, blocked the fine pores, resulting in slow ink absorption and low absorption capacity. In addition this swellable layer also fixed inks (e.g. dyes) in the structures, leaving a clear pattern on top of a coating layer. Conversely, the non-swellable binder, which was applied later, facilitated faster ink absorption and

capacity, but poor color-fixing abilities. To improve the color fixing on the coating layers, Lamminmaki introduced cationic additives, such as PolyDADMAC.<sup>111</sup>

Recently, Gane's group explored the application of calcium carbonates on the biosensor area. Using a pilot-scale blade coater, they coated the calcium carbonates, especially the modified calcium carbonates, with different binders on a polyester film. Subsequent testing of the aqueous inks' wicking speeds showed that these coating structures, which consisted of modified calcium carbonates and microfibrillated cellulose, provided changeable wicking behaviors. The wicking distances of a liquid during the testing period can be expressed as  $d = kt^{0.5}$ , which corresponds to the Lucas-Washburn equation.<sup>110</sup> Gane *et al.* then used this porous coating media (modified calcium carbonate and MFC) to pattern a test strip by inkjet printing hydrophobic barriers (see Figure 1 - 12 (C)). The resultant test strip was then applied as a lateral flow test strip to screen for the compound, 7-hydroxycoumarin, in a cytochrome P450 assay.<sup>109</sup> This research was the first documented application of a modified calcium-carbonate coating layer as a lateral flow test strip substrate in cytochrome P450 metabolism research, and it demonstrated that calcium-carbonate-based porous media has considerable promise as a lateral flow biosensor substrate.

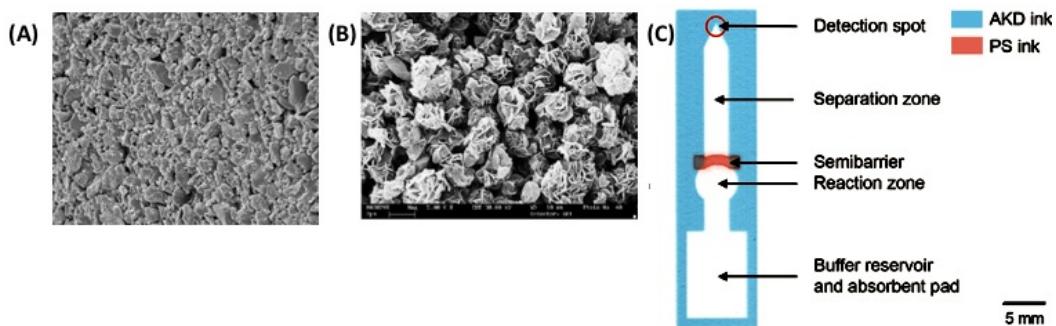


Figure 1 - 12. (A) An SEM image of ground calcium carbonate. (B) Modified calcium carbonate with hydroxyapatite, formed into a nano-dimensioned structure. Adapted from Ref.<sup>106</sup> (C) A lateral flow test strip detecting 7-hydroxycoumarin in a cytochrome P450 assay. The test substrate is a blade coated with a modified calcium-carbonate-based layer, which was patterned with hydrophobic inks by an inkjet printer. Adapted from Ref.<sup>109</sup>

## 1.5 Objectives

The overall objective of this thesis was to contribute with methods, techniques and materials that facilitate the fabrication of lateral flow biosensors. The specific goals were:

1. To design an accelerated screening process for obtaining promising formulations of pigments and binders for printing.

2. To develop proofs of concept that a printable porous media is applicable for lateral flow test bioassays.
3. To identify the clogging mechanisms associated with the printing of silica sols, which is used as a protective layer for enzyme immobilization, and to evaluate possible solutions.
4. To understand the clogging mechanisms associated with the printing of six model inks of dilute colloidal nanoparticles, each with a different particle charge, particle size, and softness.

## **1.6 Thesis outline**

*Chapter 1.* This chapter reviews the background of this project, highlights the challenges associated with applying piezoelectric inkjet printing for biosensor fabrication, and introduces a promising porous substrate for lateral flow biosensors.

*Chapter 2.* This chapter investigates colloidal stability and silica deposition on surfaces, both under normal flow and piezoelectrically driven oscillating flow through an inkjet cartridge. An extended silica-sol printing method is also investigated by modifying the pH values. This work has been published in *Journal of Sol-Gel Science and Technology*, 2018, 87, 3, 657-664.<sup>112</sup>

*Chapter 3.* This chapter investigates the print head clogging mechanisms associated with six colloidal nanoparticle inks with different sizes, surface charges, and softness. Printing experiments were combined with nanoparticle deposition studies and with experiments wherein inks were pumped through printheads at a constant flow rate with a syringe pump. This work has been published in *Langmuir*, 2019, 35, 16, 5517-5524.<sup>113</sup>

*Chapter 4.* This chapter develops an accelerated process for screening pigments and binders that can be used to construct a porous media for use in a lateral flow test strip. This accelerated process includes an automated sample preparation, a parallel coating process, and parallel wicking tests.

*Chapter 5.* This chapter introduces a novel printable porous media as a lateral flow biosensor substrate. In addition, the wicking behaviors and biocompatibility of this printed media are also investigated. This work has been submitted to *Industrial & Engineering Chemistry Research*.

*Chapter 6.* Conclude my contribution.

## Reference

1. DESA, U. Life Expectancy and Healthy Life Expectancy Data by Country. <http://apps.who.int/gho/data/node.main.SDG2016LEX?lang=en>.
2. DESA, U., Status of the Health-related SDGs. *New York United Nations Department of Economic & Social Affairs* **2018**.
3. Yetisen, A. K.; Akram, M. S.; Lowe, C. R., Paper-based microfluidic point-of-care diagnostic devices. *Lab Chip* **2013**, *13* (12), 2210-51.
4. Choi, D.-H.; Seob Kim, J.; Cutting, G. R.; Searson, P. C., A wearable potentiometric chloride sweat sensor: the critical role of the salt bridge. *Analytical Chemistry* **2016**.
5. Romeo, A.; Leung, T. S.; Sanchez, S., Smart biosensors for multiplexed and fully integrated point-of-care diagnostics. *Lab on a Chip* **2016**.
6. Fu, Q.; Wu, Z.; Xu, F.; Li, X.; Yao, C.; Xu, M.; Sheng, L.; Yu, S.; Tang, Y., A portable smart phone-based plasmonic nanosensor readout platform that measures transmitted light intensities of nanosubstrates using an ambient light sensor. *Lab on a Chip* **2016**, *16* (10), 1927-1933.
7. Engine, M. R. Biosensor Market By Application (Point of Care, Home Diagnostics, Research Labs, Biodefense, Environmental Monitoring); By Type (Electrochemical Biosensors, Piezoelectric Biosensors, Optical Biosensors, Thermal Biosensors, Nano mechanical Biosensors); By Product Type (Wearable Biosensors, Non-Wearable Biosensors) and by Regional Analysis - Global Forecast by 2018 - 2024. <https://www.marketresearchengine.com/biosensor-market-report>.
8. Biermann, C. J., *Handbook of pulping and papermaking*. Elsevier: 1996.
9. Dungchai, W.; Chailapakul, O.; Henry, C. S., A low-cost, simple, and rapid fabrication method for paper-based microfluidics using wax screen-printing. *Analyst* **2011**, *136* (1), 77-82.
10. Martinez, A. W.; Phillips, S. T.; Butte, M. J.; Whitesides, G. M., Patterned paper as a platform for inexpensive, low-volume, portable bioassays. *Angewandte Chemie International Edition* **2007**, *46* (8), 1318-1320.
11. Li, J.; Rossignol, F.; Macdonald, J., Inkjet printing for biosensor fabrication: combining chemistry and technology for advanced manufacturing. *Lab on a Chip* **2015**, *15* (12), 2538-2558.
12. Akyazi, T.; Basabe-Desmonts, L.; Benito-Lopez, F., Review on microfluidic paper-based analytical devices towards commercialisation. *Analytica chimica acta* **2018**, *1001*, 1-17.
13. Wijshoff, H., The dynamics of the piezo inkjet printhead operation. *Physics reports* **2010**, *491* (4), 77-177.
14. Turner, A. P. F., Biosensors: sense and sensibility. *Chem Soc Rev* **2013**, *42* (8), 3184-3196.
15. Bahadir, E. B.; Sezginurk, M. K., Applications of commercial biosensors in clinical, food, environmental, and biothreat/biowarfare analyses. *Anal Biochem* **2015**, *478*, 107-120.
16. Sadana, A.; Sadana, N., *Biomarkers and Biosensors: Detection and Binding to Biosensor Surfaces and Biomarkers Applications*. Newnes: 2014.
17. Mahato, K.; Srivastava, A.; Chandra, P., Paper based diagnostics for personalized health care: Emerging technologies and commercial aspects. *Biosensors and Bioelectronics* **2017**, *96*, 246-259.

18. Zaytseva, N. V.; Goral, V. N.; Montagna, R. A.; Baeumner, A. J., Development of a microfluidic biosensor module for pathogen detection. *Lab on a Chip* **2005**, *5* (8), 805-811.
19. Shinwari, M. W.; Deen, M. J.; Landheer, D., Study of the electrolyte-insulator-semiconductor field-effect transistor (EISFET) with applications in biosensor design. *Microelectronics Reliability* **2007**, *47* (12), 2025-2057.
20. Pelton, R., Bioactive paper provides a low-cost platform for diagnostics. *Trac-Trend Anal Chem* **2009**, *28* (8), 925-942.
21. De Gennes, P.-G.; Brochard-Wyart, F.; Quéré, D., *Capillarity and wetting phenomena: drops, bubbles, pearls, waves*. Springer Science & Business Media: 2013.
22. Aikio, S.; Gronqvist, S.; Hakola, L.; Hurme, E.; Jussila, S. *Bioactive Paper and Fibre Products: Patent and Literary Survey*; 2007.
23. Martinez, A. W.; Phillips, S. T.; Whitesides, G. M.; Carrilho, E., Diagnostics for the Developing World: Microfluidic Paper-Based Analytical Devices. *Analytical Chemistry* **2010**, *82* (1), 3-10.
24. Songok, J.; Tuominen, M.; Teisala, H.; Haapanen, J.; Makela, J.; Kuusipalo, J.; Toivakka, M., Paper-Based Microfluidics: Fabrication Technique and Dynamics of Capillary-Driven Surface Flow. *Acs Appl Mater Inter* **2014**, *6* (22), 20060-20066.
25. Yetisen, A. K.; Akram, M. S.; Lowe, C. R., Paper-based microfluidic point-of-care diagnostic devices. *Lab on a Chip* **2013**, *13* (12), 2210-2251.
26. Koczula, Katarzyna M.; Gallotta, A., Lateral flow assays. *Essays In Biochemistry* **2016**, *60* (1), 111-120.
27. Millipore, Rapid Lateral Flow Test Strips Considerations for Product Development. *In Lit. No. TB500EN00EM Rev. C 12/13* **2013**.
28. Millipore, Hi-Flow™ Plus Membranes and Surewick® Pad Materials. *In Lit. No. PB1267EN00* **2008**.
29. Millipore, Performance of Estapor® Microspheres and Hi-Flow™ Plus Membranes in a Lateral Flow Assay for Human Chorionic Gonadotropin (hCG). **2014**.
30. Fujita, K.; Ouchiyama, K.; Katayama, E., Guillotine cutter. Google Patents: 2008.
31. Fujifilm, Dimatix materials printer-DMP2831. **2014**.
32. Rackus, D. G.; Shamsi, M. H.; Wheeler, A. R., Electrochemistry, biosensors and microfluidics: a convergence of fields. *Chem Soc Rev* **2015**.
33. Yamada, K.; Shibata, H.; Suzuki, K.; Citterio, D., Toward practical application of paper-based microfluidics for medical diagnostics: state-of-the-art and challenges. *Lab on a Chip* **2017**, *17* (7), 1206-1249.
34. Hoath, S. D., *Fundamentals of inkjet printing: the science of inkjet and droplets*. John Wiley & Sons: 2016.
35. Le, H. P., Progress and trends in ink-jet printing technology. *Journal of Imaging Science and Technology* **1998**, *42* (1), 49-62.
36. Fujifilm, FUJIFILM Dimatix Materials Printer DMP-2800 Series User Manual.
37. Jang, D.; Kim, D.; Moon, J., Influence of Fluid Physical Properties on Ink-Jet Printability. *Langmuir* **2009**, *25* (5), 2629-2635.
38. Lee, A.; Sudau, K.; Ahn, K. H.; Lee, S. J.; Willenbacher, N., Optimization of Experimental Parameters to Suppress Nozzle Clogging in Inkjet Printing. *Ind Eng Chem Res* **2012**, *51* (40), 13195-13204.
39. Reis, N.; Derby, B. In *Ink jet deposition of ceramic suspensions: Modeling and experiments of droplet formation*, MRS proceedings, Cambridge Univ Press: 2000; p 65.

40. Sassolas, A.; Blum, L. J.; Leca-Bouvier, B. D., Immobilization strategies to develop enzymatic biosensors. *Biotechnol Adv* **2012**, *30* (3), 489-511.
41. Wang, J. PRINTING AND CHARACTERIZATION OF INKS FOR PAPER-BASED BIOSENSORS. McMaster University, 2014.
42. Jahanshahi-Anbuhi, S., Development of Ready-to-Use Biosensors for Diagnostics and Biosensing. **2015**.
43. Hossain, S. Z.; Luckham, R. E.; McFadden, M. J.; Brennan, J. D., Reagentless bidirectional lateral flow bioactive paper sensors for detection of pesticides in beverage and food samples. *Analytical chemistry* **2009**, *81* (21), 9055-9064.
44. Hossain, S. Z.; Luckham, R. E.; Smith, A. M.; Lebert, J. M.; Davies, L. M.; Pelton, R. H.; Filipe, C. D.; Brennan, J. D., Development of a bioactive paper sensor for detection of neurotoxins using piezoelectric inkjet printing of sol-gel-derived bioinks. *Analytical chemistry* **2009**, *81* (13), 5474-5483.
45. Brinker, C. J.; Scherer, G. W., *Sol-gel science: the physics and chemistry of sol-gel processing*. Academic press: 2013.
46. Maejima, K.; Tomikawa, S.; Suzuki, K.; Citterio, D., Inkjet printing: an integrated and green chemical approach to microfluidic paper-based analytical devices. *Rsc Adv* **2013**, *3* (24), 9258-9263.
47. Yamada, K.; Henares, T. G.; Suzuki, K.; Citterio, D., Paper-Based Inkjet-Printed Microfluidic Analytical Devices. *Angewandte Chemie International Edition* **2015**, *54* (18), 5294-5310.
48. Fenton, E. M.; Mascarenas, M. R.; Lopez, G. P.; Sibbett, S. S., Multiplex lateral-flow test strips fabricated by two-dimensional shaping. *ACS Appl Mater Interfaces* **2009**, *1* (1), 124-9.
49. Fu, E.; Lutz, B.; Kauffman, P.; Yager, P., Controlled reagent transport in disposable 2D paper networks. *Lab on a Chip* **2010**, *10* (7), 918-920.
50. Carrilho, E.; Martinez, A. W.; Whitesides, G. M., Understanding wax printing: a simple micropatterning process for paper-based microfluidics. *Anal Chem* **2009**, *81* (16), 7091-5.
51. Wang, J.; Monton, M. R. N.; Zhang, X.; Filipe, C. D.; Pelton, R.; Brennan, J. D., Hydrophobic sol-gel channel patterning strategies for paper-based microfluidics. *Lab on a Chip* **2014**, *14* (4), 691-695.
52. Koivunen, R.; Jutila, E.; Bollström, R.; Gane, P., Hydrophobic patterning of functional porous pigment coatings by inkjet printing. *Microfluidics and Nanofluidics* **2016**, *20* (6), 1-21.
53. Dressaire, E.; Sauret, A., Clogging of microfluidic systems. *Soft Matter* **2017**, *13* (1), 37-48.
54. Sauret, A.; Barney, E. C.; Perro, A.; Villermaux, E.; Stone, H. A.; Dressaire, E., Clogging by sieving in microchannels: Application to the detection of contaminants in colloidal suspensions. *Applied Physics Letters* **2014**, *105* (7).
55. Zuriguel, I., Invited review: Clogging of granular materials in bottlenecks. *Papers in physics* **2014**, *6* (2), 0-0.
56. Wyss, H. M.; Blair, D. L.; Morris, J. F.; Stone, H. A.; Weitz, D. A., Mechanism for clogging of microchannels. *Phys Rev E* **2006**, *74* (6).
57. Schoenitz, M.; Grundemann, L.; Augustin, W.; Scholl, S., Fouling in microstructured devices: a review. *Chemical Communications* **2015**, *51* (39), 8213-8228.
58. Bos, J. A., *Air entrapment and drop formation in piezo inkjet printing*. University of Twente: 2011.

59. Kim, J.; Erath, J.; Rodriguez, A.; Yang, C., A high-efficiency microfluidic device for size-selective trapping and sorting. *Lab on a Chip* **2014**, *14* (14), 2480-2490.
60. Berthet, H.; Fermigier, M.; Lindner, A., Single fiber transport in a confined channel: Microfluidic experiments and numerical study. *Phys Fluids* **2013**, *25* (10), 103601.
61. Kwon, K. D.; Vadhillo-Rodriguez, V.; Logan, B. E.; Kubicki, J. D., Interactions of biopolymers with silica surfaces: Force measurements and electronic structure calculation studies. *Geochimica Et Cosmochimica Acta* **2006**, *70* (15), 3803-3819.
62. Campbell, A. I.; Haw, M. D., Jamming and unjamming of concentrated colloidal dispersions in channel flows. *Soft Matter* **2010**, *6* (19), 4688-4693.
63. Whitesides, G. M.; Grzybowski, B., Self-assembly at all scales. *Science* **2002**, *295* (5564), 2418-2421.
64. Israelachvili, J. N., *Intermolecular and surface forces*. Academic press: 2011.
65. Kim, B.-H.; Kim, T.-G.; Lee, T.-K.; Kim, S.; Shin, S.-J.; Kim, S.-J.; Lee, S.-J., Effects of trapped air bubbles on frequency responses of the piezo-driven inkjet printheads and visualization of the bubbles using synchrotron X-ray. *Sensors and Actuators A: Physical* **2009**, *154* (1), 132-139.
66. de Jong, J.; de Bruin, G.; Reinten, H.; van den Berg, M.; Wijshoff, H.; Versluis, M.; Lohse, D., Air entrapment in piezo-driven inkjet printheads. *The Journal of the Acoustical Society of America* **2006**, *120* (3), 1257-1265.
67. Beulen, B.; Jong, J. d.; Reinten, H.; Berg, M. v. d.; Wijshoff, H.; van Dongen, R., Flows on the nozzle plate of an inkjet printhead. *Experiments in Fluids* **2006**, *42* (2), 217-224.
68. de Jong, J.; Jeurissen, R.; Borel, H.; Berg, M. v. d.; Wijshoff, H.; Reinten, H.; Versluis, M.; Prosperetti, A.; Lohse, D., Entrapped air bubbles in piezo-driven inkjet printing: Their effect on the droplet velocity. *Physics of Fluids* **2006**, *18* (12), 121511.
69. Meidani, A. R. N.; Hasan, M., Mathematical and physical modelling of bubble growth due to ultrasound. *Appl Math Model* **2004**, *28* (4), 333-351.
70. Jeurissen, R. J. M., *Bubbles in inkjet printheads: analytical and numerical models*. University of Twente: 2009.
71. Mak, W. C.; Beni, V.; Turner, A. P. F., Lateral-flow technology: From visual to instrumental. *Trac-Trend Anal Chem* **2016**, *79*, 297-305.
72. Müller, R. H.; Clegg, D. L., Automatic Paper Chromatography. *Analytical Chemistry* **1949**, *21* (9), 1123-1125.
73. Tonkinson, J. L.; Stillman, B. A., Nitrocellulose: A tried and true polymer finds utility as a post-genomic substrate. *Front Biosci* **2002**, *7*, C1-C12.
74. GE Fridley, C. H., SB Oza, P Yager, The evolution of nitrocellulose as a material for bioassays. *MRS bulletin* **2013**, *38* (4), 326-330.
75. Baker, R. W., *Membrane technology and applications*. . John Wiley & Sons.: John Wiley & Sons., 2012.
76. Sartorius Stedim Biotech UniSart® Nitrocellulose Membranes The Substrate of Choice for Protein Assays. <https://www.sartorius.com/resource/blob/37488/189418707763112e1360bdde5c88cb9c/b-roch-unisart-nitro-sl-1536-e-data.pdf>.
77. Tejado, A.; van de Ven, T. G., Why does paper get stronger as it dries? *Materials today* **2010**, *13* (9), 42-49.
78. Yang, D.; Zhong, L.-X.; Yuan, T.-Q.; Peng, X.-W.; Sun, R.-C., Studies on the structural characterization of lignin, hemicelluloses and cellulose fractionated by ionic liquid followed by alkaline extraction from bamboo. *Ind Crop Prod* **2013**, *43*, 141-149.

79. Wen, W.; Yan, X.; Zhu, C.; Du, D.; Lin, Y., Recent Advances on Electrochemical Immunosensors. *Analytical Chemistry* **2016**.
80. Liu, Z.; He, X.; Han, J.; Zhang, X.; Li, F.; Li, A.; Qu, Z.; Xu, F., Liquid wicking behavior in paper-like materials: mathematical models and their emerging biomedical applications. *Microfluidics and Nanofluidics* **2018**, *22* (11), 132.
81. Bird, R. B.; Stewart, W. E.; Lightfoot, E. N., *Transport phenomena*. John Wiley & Sons: 2007.
82. Rowlinson, J. S., and Benjamin Widom., *Molecular theory of capillarity*. Oxford University Press: 1982.
83. Young, T., III. An essay on the cohesion of fluids. *Philosophical transactions of the royal society of London* **1805**, (95), 65-87.
84. Athy, L. F., Density, porosity, and compaction of sedimentary rocks. *AAPG Bulletin* **1930**, *14* (1), 1-24.
85. Rouquerol, J.; Avnir, D.; Fairbridge, C.; Everett, D.; Haynes, J.; Pernicone, N.; Ramsay, J.; Sing, K.; Unger, K., Recommendations for the characterization of porous solids (Technical Report). *Pure and Applied Chemistry* **1994**, *66* (8), 1739-1758.
86. Mikhail, R. S.; Brunauer, S.; Bodor, E., Investigations of a complete pore structure analysis: I. Analysis of micropores. *J Colloid Interf Sci* **1968**, *26* (1), 45-53.
87. Giesche, H., Mercury porosimetry: a general (practical) overview. *Particle & particle systems characterization* **2006**, *23* (1), 9-19.
88. Washburn, E. W., The dynamics of capillary flow. *Physical review* **1921**, *17* (3), 273.
89. Couper, J. R., W. Roy Penney, and James R. Fair., *Chemical Process Equipment-Selection and Design (Revised 2nd Edition)*. Gulf Professional Publishing: 2009.
90. Whitaker, S., Flow in porous media I: A theoretical derivation of Darcy's law. *Transport Porous Med* **1986**, *1* (1), 3-25.
91. Liu, Z.; He, X. C.; Han, J. X.; Zhang, X. H.; Li, F.; Li, A.; Qu, Z. G.; Xu, F., Liquid wicking behavior in paper-like materials: mathematical models and their emerging biomedical applications. *Microfluidics and Nanofluidics* **2018**, *22* (11).
92. Liu, Z.; Hu, J.; Zhao, Y. M.; Qu, Z. G.; Xu, F., Experimental and numerical studies on liquid wicking into filter papers for paper-based diagnostics. *Appl Therm Eng* **2015**, *88*, 280-287.
93. Jahanshahi-Anbuhi, S.; Chavan, P.; Sicard, C.; Leung, V.; Hossain, S. Z.; Pelton, R.; Brennan, J. D.; Filipe, C. D., Creating fast flow channels in paper fluidic devices to control timing of sequential reactions. *Lab on a Chip* **2012**, *12* (23), 5079-5085.
94. Parolo, C.; Medina-Sánchez, M.; de la Escosura-Muñiz, A.; Merkoçi, A., Simple paper architecture modifications lead to enhanced sensitivity in nanoparticle based lateral flow immunoassays. *Lab on a Chip* **2013**, *13* (3), 386-390.
95. Rivas, L.; Medina-Sánchez, M.; de la Escosura-Muñiz, A.; Merkoçi, A., Improving sensitivity of gold nanoparticle-based lateral flow assays by using wax-printed pillars as delay barriers of microfluidics. *Lab on a Chip* **2014**, *14* (22), 4406-4414.
96. Choi, J. R.; Liu, Z.; Hu, J.; Tang, R.; Gong, Y.; Feng, S.; Ren, H.; Wen, T.; Yang, H.; Qu, Z.; Pingguan-Murphy, B.; Xu, F., Polydimethylsiloxane-Paper Hybrid Lateral Flow Assay for Highly Sensitive Point-of-Care Nucleic Acid Testing. *Analytical Chemistry* **2016**, *88* (12), 6254-6264.
97. Wang, J.; Bowie, D.; Zhang, X.; Filipe, C.; Pelton, R.; Brennan, J. D., Morphology and entrapped enzyme performance in inkjet-printed sol-gel coatings on paper. *Chemistry of Materials* **2014**, *26* (5), 1941-1947.

98. Jahanshahi-Anbuhi, S.; Kannan, B.; Pennings, K.; Ali, M. M.; Leung, V.; Giang, K.; Wang, T.; White, D.; Li, Y.; Pelton, R. H.; Brennan, J. D.; Filipe, C. D. M., Automating Multi-Step Paper-Based Assays Using Integrated Layering of Reagents. *Lab on a Chip* **2017**.
99. Fu, E.; Downs, C., Progress in the development and integration of fluid flow control tools in paper microfluidics. *Lab on a Chip* **2017**.
100. Sato, K.; Oaki, Y.; Takahashi, D.; Toshima, K.; Imai, H., Hierarchical CaCO<sub>3</sub> Chromatography: A Stationary Phase Based on Biominerals. *Chemistry – A European Journal* **2015**, *21* (13), 5034-5040.
101. Bauer, C. D.; Marks, R. M.; Bernardoni, E. A., Calcium enriched milk. Google Patents: 1959.
102. Kaji, N.; Mizusawa, S.; Sahashi, M.; Tsuchida, T., Calcium-enriched drink and method for producing the same. Google Patents: 1997.
103. Gane, P. A.; Kettle, J. P.; Matthews, G. P.; Ridgway, C. J., Void space structure of compressible polymer spheres and consolidated calcium carbonate paper-coating formulations. *Ind Eng Chem Res* **1996**, *35* (5), 1753-1764.
104. Schoelkopf, J.; Ridgway, C. J.; Gane, P. A. C.; Matthews, G. P.; Spielmann, D. C., Measurement and network modeling of liquid permeation into compacted mineral blocks. *J Colloid Interf Sci* **2000**, *227* (1), 119-131.
105. Gane, P. A. C., Absorption properties of coatings: A selected overview of absorption criteria derived from recent pore network modelling. *J Disper Sci Technol* **2004**, *25* (4), 389-408.
106. Ridgway, C. J.; Gane, P. A. C.; Schoelkopf, J., Modified calcium carbonate coatings with rapid absorption and extensive liquid uptake capacity. *Colloid Surface A* **2004**, *236* (1-3), 91-102.
107. Kettle, J.; Lamminmaki, T.; Gane, P., A review of modified surfaces for high speed inkjet coating. *Surf Coat Tech* **2010**, *204* (12-13), 2103-2109.
108. Lamminmaki, T. The comparative dynamics of bulk liquid flow and interpolymer diffusion during inkjet ink imbibition in porous coating structures. 2012.
109. Jutila, E.; Koivunen, R.; Kiiski, I.; Bollstrom, R.; Sikanen, T.; Gane, P., Microfluidic Lateral Flow Cytochrome P450 Assay on a Novel Printed Functionalized Calcium Carbonate-Based Platform for Rapid Screening of Human Xenobiotic Metabolism. *Adv Funct Mater* **2018**, *28* (31).
110. Jutila, E.; Koivunen, R.; Bollstrom, R.; Gane, P., Wicking and chromatographic properties of highly porous functionalised calcium carbonate coatings custom-designed for microfluidic devices. *Journal of Micromechanics and Microengineering* **2019**, *29* (5).
111. Lamminmaki, T. T.; Kettle, J. P.; Puukko, P. J. T.; Gane, P. A. C., Absorption Capability and Inkjet Ink Colorant Penetration into Binders Commonly Used in Pigmented Paper Coatings. *Ind Eng Chem Res* **2011**, *50* (6), 3287-3294.
112. Li, Y.; Dahhan, O.; Filipe, C. D. M.; Brennan, J. D.; Pelton, R. H., Optimizing piezoelectric inkjet printing of silica sols for biosensor production. *J Sol-Gel Sci Technol* **2018**, *87* (3), 657-664.
113. Li, Y.; Dahhan, O.; Filipe, C. D. M.; Brennan, J. D.; Pelton, R. H., DEPOSITED NANOPARTICLES CAN PROMOTE AIR CLOGGING OF PIEZOELECTRIC INKJET PRINTHEAD NOZZLES. *Langmuir* **2019**.

## *Chapter 2*

### **Silica Sol-Gel Inkjet Printing**

---

In this chapter, the clogging mechanisms of inkjet printing silica sols for biosensors were investigated. The clogging results were compared under normal flow and oscillating flow. The optimal printing behavior was obtained after adjusting the pH values of silica sols, which relate to the polymerization of silica sols to gels.

The experiment design, data analysis, and draft were conducted by me. My summer student Omar Dahhan helped me on data collection. Dr. Robert Pelton and Dr. Carlos Filipe contributed with vital discussion advice in the whole project. Dr. Robert Pelton and Dr. John Brennan re-wrote parts of the draft as necessary.

This chapter and the supporting information are allowed to reprint in *Journal of Sol-Gel Science and Technology* provided by Springer Nature and Copyright Clearance Center.

### **Optimizing Piezoelectric Inkjet Printing of Silica Sols for Biosensor Production**

Yuanhua Li, Omar Dahhan, Carlos D. M. Filipe, John D. Brennan, Robert H. Pelton  
*Journal of Sol-Gel Science and Technology*, (2018) 87: 657

<https://doi.org/10.1007/s10971-018-4762-3>



# Optimizing piezoelectric inkjet printing of silica sols for biosensor production

Yuanhua Li<sup>1</sup> · Omar Dahhan<sup>1</sup> · Carlos D. M. Filipe<sup>1</sup> · John D. Brennan<sup>1</sup>  · Robert H. Pelton<sup>1</sup>

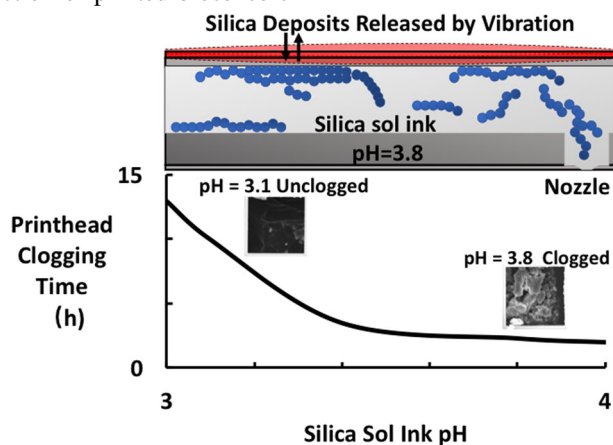
Received: 20 June 2018 / Accepted: 23 July 2018 / Published online: 6 August 2018  
© Springer Science+Business Media, LLC, part of Springer Nature 2018

## Abstract

The inkjet printing of biocompatible silica sols has gained popularity, both for biosensor production and development of holographic devices. However, there still remain significant issues related to premature clogging of inkjet printheads when printing aqueous silica sols. To better understand the causes of clogging of piezoelectric inkjet nozzles, printing studies were coupled with studies of colloidal stability along with silica deposition on surfaces, both under normal flow and piezoelectrically driven oscillating flow through an inkjet cartridge. Our studies show that clogging most likely results from deposition of silica colloids onto the internal surfaces of the printhead, followed by displacement of micron-sized pieces of the deposited material upon piezoelectric deformation of the printhead surface, which then block the nozzles of the printhead. Based on this result, we formulated a low-pH sol derived from sodium silicate and evaluated its colloidal stability, binding to silica surfaces and resistance to clogging of inkjet nozzles under normal and voltage-driven oscillating flow. We show that silica sols with a pH of 3.1 provide optimal printing behavior while allowing reproducible printing of spatially controlled silica patterns on paper to produce enzyme-based biosensing devices.

## Graphical Abstract

Use of low-pH-biocompatible silica sols allows long-term piezoelectric inkjet printing of silica inks without clogging, allowing high-throughput production of printed biosensors



**Electronic supplementary material** The online version of this article (<https://doi.org/10.1007/s10971-018-4762-3>) contains supplementary material, which is available to authorized users.

✉ John D. Brennan  
brennanj@mcmaster.ca  
✉ Robert H. Pelton  
peltonrh@mcmaster.ca

<sup>1</sup> Department of Chemical Engineering, McMaster University, Hamilton, ON L8S 4L7, Canada

<sup>2</sup> Biointerfaces Institute, McMaster University, Hamilton, ON L8S 4L7, Canada

## Highlights

- Oscillations during jetting can cause printhead clogging when inkjet printing silica sols.
- Use of low-pH sols (pH 3.1) allows printing with minimal clogging of nozzles.
- Low-pH silica sols can be printed reproducibly to create enzyme-based paper sensor strips.

**Keywords** Silica · Inkjet printing · Clogging · Enzyme entrapment · Biosensor

## 1 Introduction

Since 2007, there has been an explosion of publications describing paper-based biosensors [1–4]. In many cases, these devices are fabricated by inkjet printing of bioactive inks onto filter or chromatography paper or nitrocellulose membranes. Inkjet printing is an ideal method for dispensing expensive and sensitive reagents onto paper surfaces. In our laboratory, and many others, the DMP-2800 (Fujifilm Dimatix Inc., USA) piezoelectric printer has been favored because (1) it is a piezo printer (i.e., no heating); (2) most printing parameters are under user control; and (3) it is scalable to commercial production lines [5].

A significant amount of work from our groups has focused on printing of silica sols to create paper sensors that contained fragile enzymes trapped between layers of inkjet-printed silica [6, 7]. The structures were prepared by sequentially printing three layers. The first and third layers were silica sols at pH ~4 and the second (middle layer) was an enzyme solution in Tris buffer (100 mM, pH 7.8). Before drying, the silica layers intermixed with the buffered middle layer, increasing the pH and promoting gelation. The resulting dried sensor consisted of a 35-nm-thick porous silica coating on the filter paper fiber surfaces, which was able to retain protein activity over many months [8].

Although this biosensor format is a very promising technology, a significant issue with scalable production of such sensors is printhead failure due to clogging of nozzles when printing the top and bottom silica sol ink layers. The silica sol inks typically contain 82 wt% water, which is essential for maintaining protein activity, but leads to an unstable sol composition that seriously affects printing reliability. While it is possible to overcome the clogging of inkjet nozzles by using sols with very high alcohol content and limited or no water [9], or by printing alternative sols, such as those formed from titania [10], such compositions can denature the fragile enzymes used in our biosensors. Herein, we describe our efforts to elucidate the factors that lead to clogging of inkjet nozzles when printing aqueous silica sol inks and describe an optimized sol composition that allows printing of aqueous silica-based inks for extended durations.

## 2 Experimental section

### 2.1 Materials

Sodium silicate solution SS338-1 ( $\text{SiO}_2\text{:Na}_2\text{O}$  mole ratio ~3:2, ~60 wt% water) was obtained from Fisher Scientific. Dowex 50WX8-100 cationic exchange resin, anhydrous glycerol, Triton X-100, acetylcholinesterase from *Electrophorus electricus* (AChE, type VI-S), poly-L-arginine hydrochloride (>70 kDa), 5,5'-dithiobis(2-nitrobenzoic acid) (DTNB), and acetylthiocholine iodide (ATCh) were purchased from Sigma-Aldrich. Whatman #1 paper and 0.45- $\mu\text{m}$  syringe filters were purchased from VWR. All solutions were prepared using distilled deionized water (Milli-Q Synthesis A10 water purification system).

### 2.2 Preparation of silica sol ink

Sodium silicate sols were prepared by mixing 2.6 g of the sodium silicate solution (pH ~13) and 10 mL of water, followed by the addition of 5.5 g of Dowex cation exchange resin, which had previously been soaked in 0.1 M HCl for 1 h and then washed three times with water to charge the resin. The sol was stirred with the Dowex resin for ~30 s to replace  $\text{Na}^+$  with  $\text{H}^+$  and bring the final sol pH below 4 and the silica content to 6.2%. An aliquot of 0.1 M HCl was added to bring the final sol pH to values of 3.1, 3.4, or 3.8. Silica inks were prepared by mixing the sol with glycerol and Triton X-100 to obtain final concentrations of 30% v/v glycerol and 0.1 wt% Triton X-100. The dispersion was vacuum-filtered through Whatman No. 1 filter paper in a Büchner funnel and then passed through a 0.45- $\mu\text{m}$  membrane syringe filter to produce the final silica sol ink with a silica content of ~4.0 wt%, assuming no loss of silica during the filtration steps. The final ink had a viscosity of  $10.0 \pm 0.2$  mPa s, a surface tension of  $32.0 \pm 0.5$  mN/m, and a reciprocal Ohnesorge number of  $1/\text{Oh} = 33$ . The contact angle of a sessile drop of silica sol ink on a clean glass side was  $16 \pm 0.3^\circ$ .

### 2.3 Inkjet printing

All inkjet-printing experiments were performed with a Fujifilm Dimatix DMP-2800 fitted with a DMC-11610

printhead. The firing frequency was set to 5 kHz, and the single-nozzle voltage was adjusted to 40 V. The built-in Drop Watcher™ imaging system was used to capture images of the droplets ejected from each nozzle at 25 frames per second with printing continuing until significant printhead clogging was observed either by imaging the nozzles during printing, or by measuring the quantity of ink transferred when printing a pattern for a fixed time. For transfer measurements, the mass of the inkjet printer cartridge and the cleaning pad was determined before and after printing 80 copies of 1 cm<sup>2</sup> squares over 30 min.

## 2.4 Pumping ink through the printhead

Experiments were conducted in which clogging was measured when ink was pumped through the printhead in near-steady-state flow rather than by voltage-driven oscillatory jetting. The experimental configuration is shown in Figure S1. Tubing was connected to a DMC-11610 printhead and the printhead nozzles were imaged with a macroscope (Wild M420, Wild Heerbrugg, magnification at 1.25 × 20) fitted with a Pixelink PL-E535CU 5 megapixel color camera that recorded images at 7 fps. The silica sol ink was forced through the printhead with either a peristaltic pump (Masterflex®) at a flow rate of 2.4 mL/min or with a syringe pump (NE-1600, New Era Pump System, Inc.) fitted with a 60-mL syringe delivering 1.8 mL/min over a period of up to 180 min, with syringe changes as needed.

## 2.5 Surface tension, viscosity, and particle size

A Krüss Drop Shape Analysis System DSA 10 running DSA software (version 1.80.0.2) was used to measure the silica sol surface tension in pendant drop mode with a No.18 needle (diameter 1.2 mm). Measurements were recorded after 2 min of drop aging time. The silica sol ink viscosity was measured with a Vibro Viscometer (SV-10, A&D Company). The sample size was 10 mL and the frequency was 30 Hz. Dynamic light scattering (DLS, Model BI-APD, Brookhaven Instruments Corporation) was used to determine the hydrodynamic diameters of particles of aqueous silica with a detector angle of 90°. The duration of each measurement was 3 min and the results were analyzed by BIC dynamic light scattering software (Windows 9KDLWS version 3.34) using the EXSAMP model.

## 2.6 SEM imaging

Printheads were used to print silica sols of varying pH for specific periods of time. Following printing, the printhead was flushed with 30% v/v glycerol and 0.1 wt% Triton X-100 solution for 5 min and then dried at room temperature overnight and coated with 5 nm of platinum before being

imaged. The deposition of silica on the printhead surface and the print channel cross-section morphology were examined using a scanning electron microscope (JEOL 7000F) in the secondary electron image mode with a voltage of 10 kV and a magnification of ×2500.

## 2.7 Silica sol ink deposition on silica QCM-D sensors

Quartz crystal microbalance measurements (QCM-D, Q-Sense E4, Gothenburg, Sweden) were used to measure silica particle deposition on silica QCM chips. The silica sensor surface was first equilibrated by flowing an aqueous solution of glycerol (30% v/v) and Triton X-100 (0.1 wt%) for 30 min at a flow rate of 0.1 mL/min, followed by the flow of the aqueous silicate sol ink with pH values of 3.1, 3.4, or 3.8 over a period of 50 min, and then addition of the original aqueous glycerol and Triton X-100 solution without silica particles for a further 30 min. The experiment was repeated three times. The absorbed mass ( $\Delta m$ ) was estimated by the Sauerbrey equation using the frequency difference between the initial and final equilibration steps [11].

## 2.8 Enzyme-based pesticide sensors printed with silica sols

The AChE biosensor was prepared, as described elsewhere [7] by sequential printing of four ink layers, comprised of a bottom layer of 2 wt% poly-L-lysine, a lower layer of pH 3.1 silica ink, a layer of AChE (500 U/mL in 100 mM Tris buffer, pH 7.8 with 30% v/v glycerol and 0.1% Triton X-100), and a top layer of pH 3.1 silica ink. The wet density of each layer was 25 mL/m<sup>2</sup> using a 20- $\mu$ m drop-to-drop spacing, a nozzle voltage of 40 V, and a firing frequency of 5 kHz at room temperature and humidity. To evaluate both the effects of printing time after ink formulation, a pattern containing a 13 × 13 rectangular grid of AChE sensors (sensor size of 5 × 2 mm, with a 2-mm gap) was printed, with the bottom silica layer of silica sol ink printed column by column with a 30-min interval ranging from 0 to 6 h (denoted as  $t_B$ ) after formulation, followed by printing of the enzyme layer, drying for 30 min, and then printing of a top layer of silica sol row by row with a 30-min interval ranging from 0 to 6 h after formulation (denoted as  $t_T$ ). The final pattern of the grid showing the specific ink-printing times is provided in Figure S2. Control sensors were also printed using an AChE layer without the underlying cationic layer and without the top or bottom silica sol layers to evaluate the role of each layer, and also by printing sensors without AChE to obtain background values for color changes from the sensors.

To evaluate the sensor responses, an aqueous mixture of ATCh (2 mM) and DTNB (1 mM) at pH 7.0 was printed onto each of the sensor elements using the Dimatix printer

with the same settings as described above for sensor fabrication. A total of 250 nL of the mixture was printed onto each element, and the total printing time was 5 min for the 169 sensor elements. After 1 h, an image was taken with an iPhone 8 camera with the flash turned off, and the color intensity was determined using ImageJ software, as described elsewhere [8]. In brief, the image was converted to an 8-bit format, inverted into gray scale, and then the difference of color intensity ( $\Delta CI$ ) was measured between the sensor element and a background obtained for samples containing no enzyme [8].

### 3 Results and discussion

#### 3.1 Overview of inkjet clogging

Before outlining the results obtained from printing of silica sols, it is useful to understand the basic features of the Dimatix printhead and the general mechanisms that induce clogging. The DMC-11610 printhead for the DMP-2800 printer has 16 printing nozzles. Figure S3 shows a cross-sectional diagram of one channel and nozzle including the relevant dimensions, while Figure S4 shows a photograph of a printhead and a nozzle. Ink flows by gravity from a small (1.5 mL) cartridge into the printhead, and is then driven through an ink channel ( $100 \times 100 \mu\text{m}^2$ ) by the oscillations of the piezoelectric layer and ultimately is ejected at a truncated pyramidal orifice (i.e., a right frustum) with a 20- $\mu\text{m}$  wide opening, producing 10-pL drops with a spherical diameter of  $\sim 27 \mu\text{m}$ . The ink-contacting surfaces are silica formed by the oxidation of the silicon printhead.

Clogging of such microfluidic orifices by colloidal inks has been well studied, and a recent review by Dressaire and Sauret gives an excellent summary of microfluidic clogging research [12]. They propose three clogging mechanisms: (1) filtration (sieving), where particles larger than the channels are trapped, partially or completely blocking flow; (2) deposition (aggregation), where colloidal particles form aggregates in the liquid phase and spontaneously deposit onto channel surfaces, decreasing orifice diameters; and (3) jamming (bridging), where a cluster of particles in a constriction become mechanically trapped, blocking flow. In addition, it has been reported that inhalation of small air bubbles into the printhead can occur during printing, which has the potential to block flow [13–16]. Hence, the dispersed particle size in inks should be much smaller than the size of restrictions in the ink path; the ink colloids should be colloiddally stable and resistant to deposition on printhead surfaces; the volume fraction of dispersed solids should be far below the jamming limit; and ink layers should not be allowed to build up on the nozzle plate. To avoid clogging, most inkjet printers, including the Dimatix printer,

incorporate a cleaning operation involving a purge process to remove trapped air; a spit process where droplets are jetted at high voltage; and a blot process, where excess fluid on the nozzle plate is adsorbed onto a cleaning pad. Typical cleaning frequencies can range from 30 s to 15 min; however, unstable inks can require very frequent nozzle cleaning, which is incompatible with scalable manufacturing.

#### 3.2 Colloidal stability of silica sol inks

Prior to printing experiments, the pH and colloidal stability of the silica sols were investigated. Interestingly, each ink showed a slow change toward basic pH as the aging of the ink continued. For example, the ink with an initial pH of 3.1 slowly increased to 3.4 over 24 h, while the pH 3.4 ink increased to pH 3.7 after 10 h and the pH 3.8 ink increased to pH 4.1 in 5 h. Such shifts were not observed in ink samples that contained glycerol and Triton X-100 without silica present, and thus must be related to the silica chemistry. Under acidic pH conditions, a key reaction is that of silica condensation:  $\text{SiO}^- + \text{SiOH} \rightarrow \text{Si-O-Si} + \text{OH}^-$ , which produces  $\text{OH}^-$ , a stronger base than  $\text{Si-O}^-$ , and thus would cause small shifts to more basic pH over time. At more basic pH values, the rate of condensation would be expected to be higher, and thus the pH shift should be more rapid, as observed. Hence, the inks are not expected to be indefinitely stable, which is consistent with our observations that the inks will become viscous and eventually gel over a few days.

The proposed condensation reaction should also lead to slow growth of silica colloids with time. Figure 1 shows the average silica particle diameter obtained from dynamic light scattering (DLS) measurements as a function of aging time for each initial pH value tested. Initially, the particles were

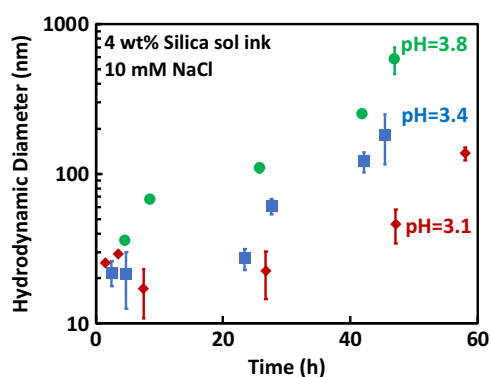


**Fig. 1** Average sol particle diameters, measured by dynamic light scattering, as a function of time for silica inks at pH 3.1, 3.4, and 3.8. Inks were stored at RT ( $\sim 23^\circ\text{C}$ ) between DLS experiments. Each point is obtained using a fresh sample from the same ink solution. The error bar is the standard deviation obtained from measurements of three different solutions. (●) pH = 3.8; (■) pH = 3.4; (◆) pH = 3.1. These symbols are used for all the remaining figures

very small (ca. 25-nm diameter) and weakly scattering at all pH values. However, at longer aging times, all of the inks showed an increase in particle diameter, which was much more pronounced at higher initial pH values. Based on the DLS results, the pH 3.1 ink remained stable (defined as less than a twofold change in particle diameter) for close to 50 h, while the pH 3.4 ink remained relatively stable for 30 h, and the pH 3.8 ink colloids grew relatively quickly and began to aggregate in less than 10 h. At longer times (ca. 50 h), both the pH 3.4 and pH 3.8 inks showed substantial aggregation, as evidenced by the particle size data, consistent with significant silica condensation. These results suggest that the fresh silica ink should not cause clogging problems at any pH below 3.8, but lower pH inks should remain stable for much longer times, and lead to decreased nozzle clogging.

### 3.3 Clogging of nozzles with silica inks

Figure 2 shows the number of clogged nozzles from printing silica ink as a function of the printing time and ink pH. The cleaning cycle time was deliberately set to the longest interval of 15 min to assess the most challenging conditions that could be used during printing. Experiments using a much shorter cleaning cycle generally led to fewer clogged nozzles for each of the inks tested (Fig. S5), however, this leads to an unreasonably long printing time as each cleaning cycle requires 3 min, and also causes substantial loss of ink. As shown in Fig. 2, the number of clogged nozzles, as determined with the camera built into the printer, increased with printing time regardless of the pH of the silica ink (see Fig. 3 for images of unclogged and clogged nozzles). However, it is noteworthy that even with a 15-min cleaning cycle, the pH 3.1 ink varies randomly between 2 and 5 clogged nozzles and does not lead to increased clogging with time, while both the pH 3.4 and 3.8 inks lead to increased numbers of clogged nozzles with time, and

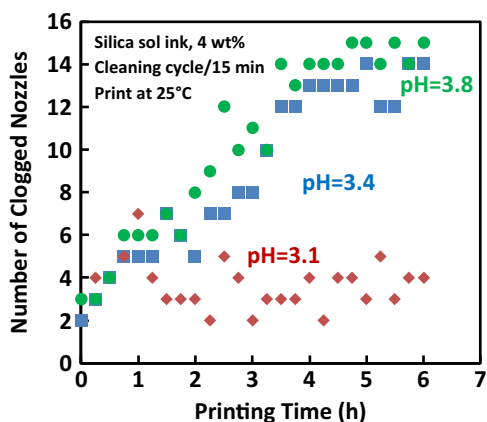


**Fig. 2** The influence of printing time and ink pH on clogging of inkjet nozzles

ultimately to clogging between 12 and 14 of the 16 nozzles (75+%) after 3.5 h of printing.

As shown in Fig. 3, the clogging occurs owing to the formation of spanning clusters of silica colloids, which are composed of aggregates of roughly 1–2  $\mu\text{m}$  in diameter along with larger rectangular “sheet-like” structures of 2–5  $\mu\text{m}$  in length with flat surfaces (see outlined area of one sheet-like structure). The images were obtained after 3.5 h of printing for a pH 3.1 (left) and pH 3.8 (right) sol, and clearly show substantially more silica deposited in the nozzle at pH 3.8 relative to pH 3.1. Given that the DLS data indicate that the average particle size is only 50 nm or less at this time, it is likely that an additional effect is in play during piezoelectrically driven printing that allows formation of larger aggregates and sheet-like structures, and ultimately reduces the time needed to clog the nozzles of the printhead.

### 3.4 Consistency of printing over time

Our key focus was on evaluating the printer performance as a function of time for each of the silica inks at the three initial pH values. Printer performance was evaluated by measuring the density of wet ink printed in a fixed pattern over time. As shown in Fig. 4, the ink at pH 3.1 can be printed consistently for at least 6 h, by which time the ink in the cartridge would be fully expended if continuous printing was done. At pH 3.4, printing performance begins to decline after 3.5 h, while at pH 3.8, the performance drops dramatically after 2.5 h. This observation is consistent with the nozzle-clogging data provided above and suggests that the printing performance begins to decline when roughly half of the nozzles are clogged. However, the decline in printing performance also occurs much more quickly than would be expected based on the DLS results, and well before there are noticeable changes in the colloid diameter, as measured by DLS. The data suggest that clogging is not strictly dependent on colloidal stability, as measured by DLS, but also depends on the propensity of silica particles to deposit onto the surfaces of the printhead, which is discussed in more detail below.

### 3.5 Pumping of inks through the printhead

To assess the effects of the piezoelectric oscillations on nozzle clogging, we compared printhead clogging based on piezoelectric printing (Fig. 2) to the case where ink was forced through the printhead with a pump. In the latter case, we employed a peristaltic pump to facilitate long experimental times. The results (Figure S6) show that over 6 h, no nozzles were plugged by pumping regardless of the ink pH. Based on these results, it appears that there is a process unique to piezoelectric printing that induces substantial clogging of the

**Fig. 3** SEM images for printing silica sols showing an unclogged and a clogged nozzle

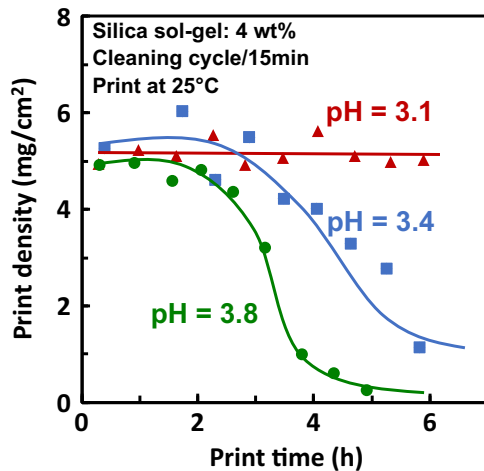
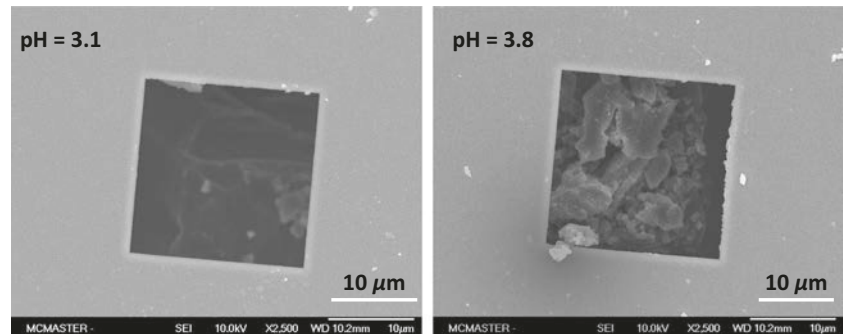


**Fig. 4** The influence of silica sol pH on the printing performance measured as the wet density of ink printed in 30-min intervals. Clogged nozzles lower the print density

printheads, and which can be tuned to some degree by careful selection of pH.

### 3.6 Evaluation of silica deposition on surfaces under flow

Given the data above, it was clear that deposition of silica onto printhead surfaces likely played a role in nozzle clogging. To further evaluate the potential mechanism of silica deposition, we examined the deposition of silica inks with varying pH onto the silica surface of a quartz crystal microbalance (QCM-D). As shown in Fig. 5, each of the inks results in a significant increase in Sauerbrey mass, which is consistent with deposition of silica from the ink solution onto the silica surface of the QCM crystal. To better evaluate the role of silica deposition alone, the control solution (30% v/v glycerol and 0.1 wt% Triton X-100) was reintroduced. It is clear that none of the sensors return to their initial values, showing that silica deposits at all pH values. The corresponding dissipation curve is shown in Figure S7. The ratio of frequency change to dissipation was approximately constant and less than 1/10th of the frequency change; therefore, we can calculate the deposition of silica

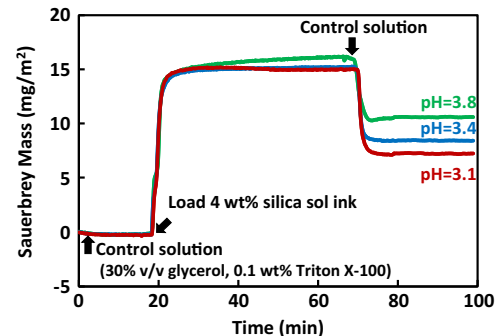


**Fig. 5** The deposition of silica sol ink on a silica QCM-D sensor surface as a function of time. The changes in Sauerbrey mass upon introduction of silica sol inks of varying pH followed by flushing of the QCM crystal with a glycerol/Triton X-100 solution

sol ink on silica sensor using the Sauerbrey equation. The Sauerbrey values of 10, 8.5, and 7 mg/m<sup>2</sup> were obtained for silica inks at pH 3.8, 3.4, and 3.1, respectively. If we assume that the silica is present as 25-nm-diameter spheres (based on DLS results), then we can calculate that 43%, 36%, and 30% of the sensor surface is covered with adsorbed silica at pH 3.8, 3.4, and 3.1 (see ESI for calculation of surface coverage). These results are consistent with the expected increase in condensation rate at higher pH values.

An important observation is the continuous deposition of the pH 3.8 ink over time, which suggests that inks at this pH continuously deposit onto the QCM surface, and thus may lead to substantial deposits after several hours. Hence, deposition of silica onto the silica surfaces of the printhead is highly likely and most likely increases as the pH of the silica ink increases.

### 3.7 Model for clogging of silica-based inks

Based on the data above, a model for clogging of nozzles when printing silica-based inks can be proposed, and an optimal printing process can be suggested. It is clear that silica sols become more basic, and thus less stable, with time. When subjected to flow without an oscillating electric field, these inks can be driven through the printhead for many hours, but eventually will still clog, likely due to initial deposition on the nozzle surface (as suggested by

QCM-D studies) coupled with longer-term destabilization of the colloidal sol over many hours. When using piezoelectrically driven printing, the clogging is significantly accelerated. Based on our data, it appears that the clogging is caused by the presence of large “sheet-like” structures several microns across, which are sufficiently large to jam the printhead. Once present, smaller colloids can deposit onto and around these sheets, until the nozzle is filled with silica species and can no longer jet the silica ink. Hence, the clogging appears to be a combination of the three main processes outlined in section 3.1, where large sheets initially jam the orifice, followed by deposition of colloidal particles onto the sheets and filtration of particles, which completely blocks the channel.

Given that large silica sheets are not present in the nozzle when pumping ink through the printhead, the origin of the large silica sheets must be related to the piezoelectric printing. Based on the QCM-D data, it is clear that the deposition of silica colloids onto surfaces increases as the pH of the silica ink increases. Hence, the surfaces of the printhead are slowly coated with a layer of silica as printing continues. As shown in Figure S3, the piezoelectric surface of the Dimatix printhead is along the channel that is at a right angle to the nozzle. This channel has a large surface onto which silica can deposit, and hence a thin sheet of silica will deposit along the length of the channel. Under piezoelectrically driven printing, the surface of the channel will be oscillating at high frequency (unlike during pumping) and hence it is likely that after a significant amount of silica deposits, the mechanical flexing of the channel surface will cause pieces of the deposited silica to detach and produce the “sheet-like” structures observed by SEM. Once formed, these structures are sufficiently large to jam the nozzle orifice, followed by further deposition of silica onto the nozzle, and then finally obstruction. At lower pH values, the degree of deposition and the overall rate of silica condensation are decreased, and hence it is possible to print for much longer periods of time before clogging becomes an issue.

### 3.8 Enzyme-based pesticide sensors printed with silica sols

Given the ultimate desire to use printed silica inks for fabrication of biosensors, we evaluated the performance and reproducibility of previously reported enzyme-based pesticide sensors printed on filter paper [6]. The sensor consists of four sequentially printed layers: L1 poly-L-arginine to promote silica adhesion to cellulose; L2 silica sol-gel; L3 the enzyme acetylcholinesterase AChE, which is deactivated by exposure to pesticide; and L4 the silica sol-gel top layer. The nanoscale structure and composition of the resulting sensor have been described in detail [8]. An array of sensors were printed using the pH 3.1 ink, wherein the silica sol ink aging time before printing the L2 and L4

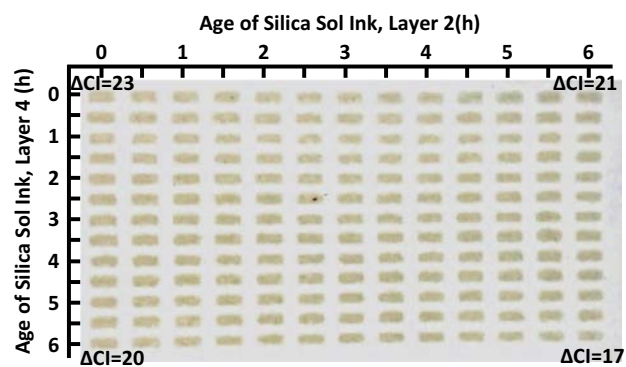


**Fig. 6** AChE (500 U/mL, Tris buffer, 100 mM, pH 7.8) catalyzed color formation as a function of the age of silica sol ink (pH 3.1) used to print silica sol-gel layers 2 and 4 in the fabrication of pesticide biosensors. The color was generated upon exposure to an aqueous mixture of ATCh (2 mM) and DTNB (1 mM) at pH 7. Printed sensors not containing AChE were used to obtain background signals, which were subtracted from each sensor signal (see Figure S8). Visual inspection and color intensity ( $\Delta CI$ ) values showed no indication of ink age influencing sensor performance over 6 h

layers was independently varied between 0 and 6 h in 30-min increments. Inks at pH 3.4 and 3.8 were not evaluated as these had already proven to have irreproducible deposition of silica on paper surfaces (see Fig. 4).

As shown in Fig. 6, the size and shape of the rectangular sensors appeared to be independent of ink aging time of 6 h, suggesting no extreme clogging of nozzles. Analysis of the color intensities showed a slight decrease with ink aging time. In the extreme, 6-h aging of ink for both the L2 and L4 layers before printing, the sensor gave a color intensity of  $\Delta CI = 17$  which was only 25% less than the intensity of sensors prepared with fresh silica sol ink (see Fig. 6). The data clearly show that functional sensors can be printed over a relatively long period of time when using the low-pH ink, demonstrating that inkjet printing can potentially be used for scalable manufacturing of sol-gel-based sensors on paper.

## 4 Significant findings

The fabrication of paper-based biosensors using the inkjet printing of aqueous silica-based inks was reported almost 10 years ago [6], but our ability to scale up the process to allow reproducible printing of a large numbers of tests has been curtailed by issues related to clogging of inkjet printheads by the silica sol, which led to an inability to print sensors over even a 1-h period [8]. In this work, we undertook a study of how the initial pH of the silica-based ink affects this clogging phenomenon, including how pH affects the stability of silica sols (via DLS), the ability of silica to deposit on silica surfaces using QCM-D, and the effect of voltage-driven oscillatory flow (piezoelectric printing vs. pumping) on clogging. Our data indicate that

silica inks deposit onto silica surfaces, such as those of the printhead, and that the amount of deposition increases at higher pH. When present in a channel that is undergoing piezoelectrically driven mechanical deformation, the silica deposits can detach as “sheet-like” structures that jam the nozzles of the printhead, leading to clogging. Our data show that adjusting the pH of the silica ink to a value of 3.1 (or likely lower) can sufficiently reduce the rate of deposition so as to allow reproducible inkjet printing over at least 6 h (sufficient to expend all ink in the cartridge) while still being compatible with the fabrication of printed enzyme-based sensors. This finding has significant impact on the viability of silica inks for scalable manufacturing of sensors that incorporate sol–gel-derived layers and should help move this field forward.

## 5 Conclusions

In an effort to understand the origin of printing challenges with aqueous silica sol inks, we coupled printing studies with experiments in which ink was pumped through the printhead in steady flow and compared the colloidal stability and degree of deposition of silica inks of varying pH onto surfaces. Our results demonstrated that a key factor affecting the ability to print silica sols was the deposition of silica onto printhead surfaces, which increased with ink pH and ultimately clogged the printhead. The use of silica inks at pH 3.1 reduced the rate of silica deposition and condensation (relative to higher pH values) and allowed printing of silica inks over at least 6 h. Importantly, even when using inks at pH 3.1, it was possible to print enzyme-based sensors with good enzyme activity and high reproducibility between sensors printed at early and late times. Overall, the study demonstrates that tuning the pH of the silica sol can minimize the clogging of piezoelectric nozzles and thus allow this method to be utilized for scalable manufacturing of printed paper-based biosensors.

**Acknowledgements** The authors thank Chris Butcher (Canadian Center for Electron Microscopy, McMaster University) and Marcia Reid (McMaster Health Sciences) for sample preparation and training. The authors also thank the Natural Sciences and Engineering Research Council of Canada for funding through the *SENTINEL* Bioactive Paper Network. We also thank the Canadian Foundation for Innovation and the Ontario Ministry of Research and Innovation for Infrastructure funding to the Biointerfaces Institute. YL acknowledges funding from the China Scholarship Council (CSC). JDB holds the Canada Research Chair in Bioanalytical Chemistry and Biointerfaces. RP holds the Canada Research Chair in Interfacial Technologies.

## Compliance with ethical standards

**Conflict of interest** The authors declare that they have no conflict of interest.

## References

- Pelton R (2009) Bioactive paper - a low cost platform for diagnostics. *Trends Anal Chem* 28(8):925–942. <https://doi.org/10.1016/j.trac.2009.05.005>
- Yamada K, Henares TG, Suzuki K, Citterio D (2015) Paper-based inkjet-printed microfluidic analytical devices. *Angew Chem Int Ed* 54(18):5294–5310. <https://doi.org/10.1002/anie.201411508>
- Maejima K, Tomikawa S, Suzuki K, Citterio D (2013) Inkjet printing: An integrated and green chemical approach to microfluidic paper-based analytical devices. *Rsc Adv* 3(24):9258–9263
- Martinez AW, Phillips ST, Whitesides GM, Carrilho E (2010) Diagnostics for the developing world: Microfluidic paper-based analytical devices. *Anal Chem* 82(1):3–10. <https://doi.org/10.1021/ac9013989>
- Li J, Rossignol F, Macdonald J (2015) Inkjet printing for bio-sensor fabrication: Combining chemistry and technology for advanced manufacturing. *Lab Chip* 15(12):2538–2558
- Hossain SMZ, Luckham RE, McFadden MJ, Brennan JD (2009) Reagentless bidirectional lateral flow bioactive paper sensors for detection of pesticides in beverage and food samples. *Anal Chem* 81(21):9055–9064. <https://doi.org/10.1021/ac901714h>
- Hossain SMZ, Luckham RE, Smith AM, Lebert JM, Davies LM, Pelton R, Filipe CDM, Brennan JD (2009) Development of a bioactive paper sensor for detection of neurotoxins using piezoelectric inkjet printing of sol-gel derived bioinks. *Anal Chem* 81:5474–5483. <https://doi.org/10.1021/a900660p>
- Wang J, Bowie D, Zhang X, Filipe C, Pelton R, Brennan JD (2014) Morphology and entrapped enzyme performance in inkjet-printed sol–gel coatings on paper. *Chem Mater* 26(5):1941–1947. <https://doi.org/10.1021/cm500206s>
- Chouiki M, Schoeftner R (2011) Inkjet printing of inorganic sol–gel ink and control of the geometrical characteristics. *J Sol-Gel Sci Technol* 58(1):91–95. <https://doi.org/10.1007/s10971-010-2360-0>
- Safaryan SM, Yakovlev AV, Vinogradov AV, Vinogradov VV (2017) Inkjet printing of the chromogen free oxidase based optical biosensors. *Sens Actuatur B-Chem* 251:746–752. <https://doi.org/10.1016/j.snb.2017.05.112>
- Rodahl M, Kasemo B (1996) On the measurement of thin liquid overlayers with the quartz-crystal microbalance. *Sens Actuatur A: Phys* 54(1–3):448–456. [https://doi.org/10.1016/S0924-4247\(97\)80002-7](https://doi.org/10.1016/S0924-4247(97)80002-7)
- Dressaire E, Sauret A (2017) Clogging of microfluidic systems. *Soft Matter* 13(1):37–48. <https://doi.org/10.1039/C6SM01879C>
- Kim B-H, Kim T-G, Lee T-K, Kim S, Shin S-J, Kim S-J, Lee S-J (2009) Effects of trapped air bubbles on frequency responses of the piezo-driven inkjet printheads and visualization of the bubbles using synchrotron x-ray. *Sens Actuatur A: Phys* 154(1):132–139. <https://doi.org/10.1016/j.sna.2009.05.021>
- de Jong J, de Bruin G, Reinten H, van den Berg M, Wijshoff H, Versluis M, Lohse D (2006) Air entrapment in piezo-driven inkjet printheads. *J Acoust Soc Am* 120(3):1257–1265. <https://doi.org/10.1121/1.2216560>
- Beulen B, Jong Jd, Reinten H, Berg Mvd, Wijshoff H, van Dongen R (2006) Flows on the nozzle plate of an inkjet printhead. *Exp Fluids* 42(2):217–224. <https://doi.org/10.1007/s00348-006-0232-8>
- de Jong J, Jeurissen R, Borel H, Berg Mvd, Wijshoff H, Reinten H, Versluis M, Prosperetti A, Lohse D (2006) Entrapped air bubbles in piezo-driven inkjet printing: Their effect on the droplet velocity. *Phys Fluids* 18(12):121511. <https://doi.org/10.1063/1.2397015>

## Electronic Supporting Information

### Optimizing Piezoelectric Ink-Jet Printing of Silica Sols for Biosensor Production

Yuanhua Li,<sup>a</sup> Omar Dahhan,<sup>a</sup> Carlos D.M. Filipe,<sup>a</sup> John D. Brennan,<sup>b\*</sup> and Robert H. Pelton<sup>a\*</sup>

<sup>a</sup>Department of Chemical Engineering, <sup>b</sup>Biointerfaces Institute, McMaster University, Hamilton, Ontario, L8S 4L7, Canada

[\\*brennanj@mcmaster.ca](mailto:brennanj@mcmaster.ca); [peltonrh@mcmaster.ca](mailto:peltonrh@mcmaster.ca)

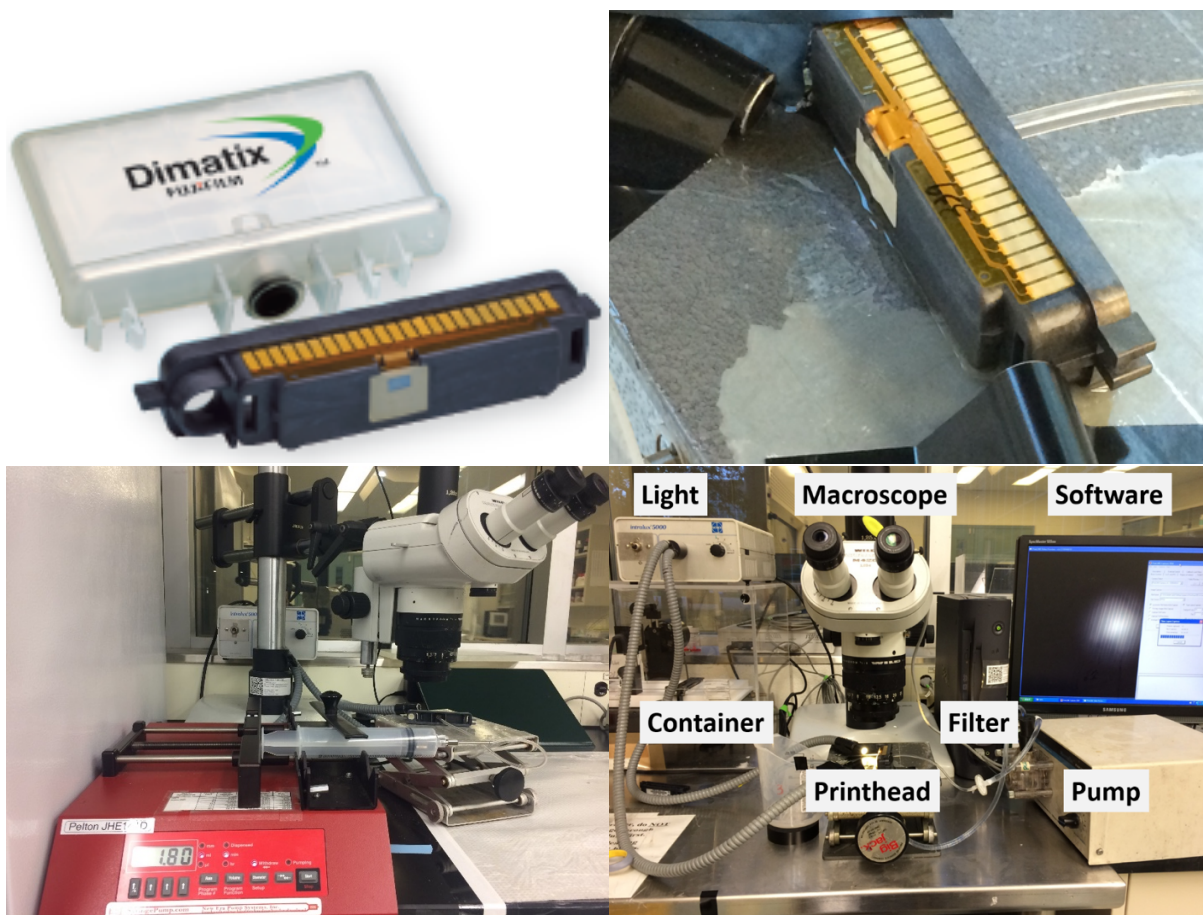


**Figure S1.** Photographs the Dimatix cartridge and printhead, and the experimental setup for pumping ink through a printhead. A peristaltic pump was used for long experiments whereas a syringe pump was used for shorter experiments.

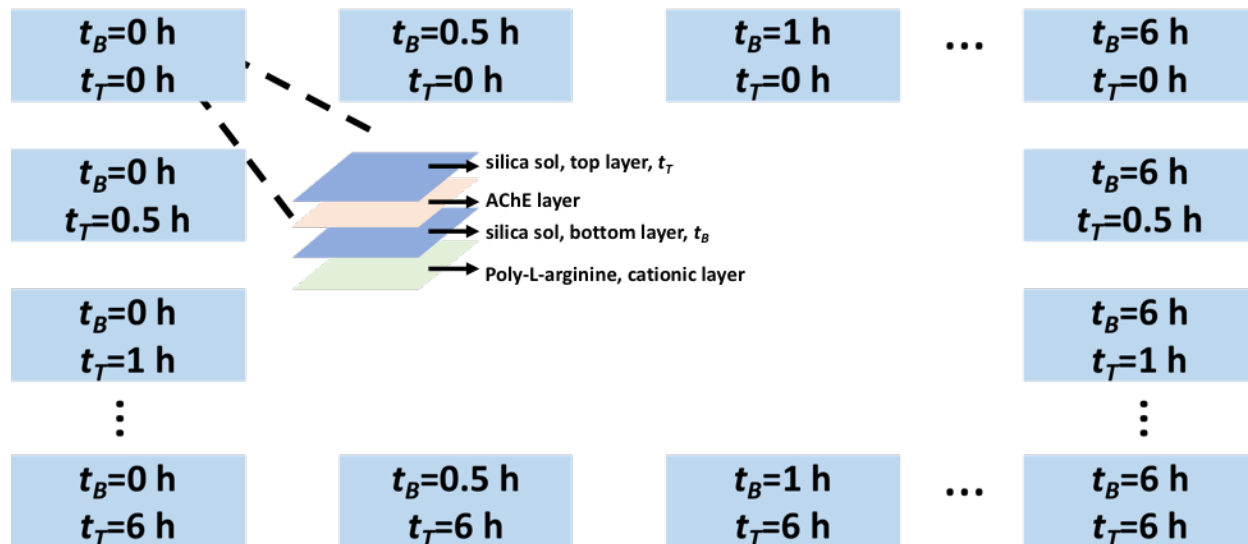


**Figure S2.** The printing pattern for AChE sensor with specific silica printing time interval. The sub figure is a four-layer structure with a poly-L-arginine layer as a cationic layer, a bottom layer( $t_B$ ) with silica sol, an AChE layer, and a top layer ( $t_T$ ) with silica sol. The bottom silica layer and the top silica layer are printing with a 30 min interval presenting a 13\*13 grid pattern.

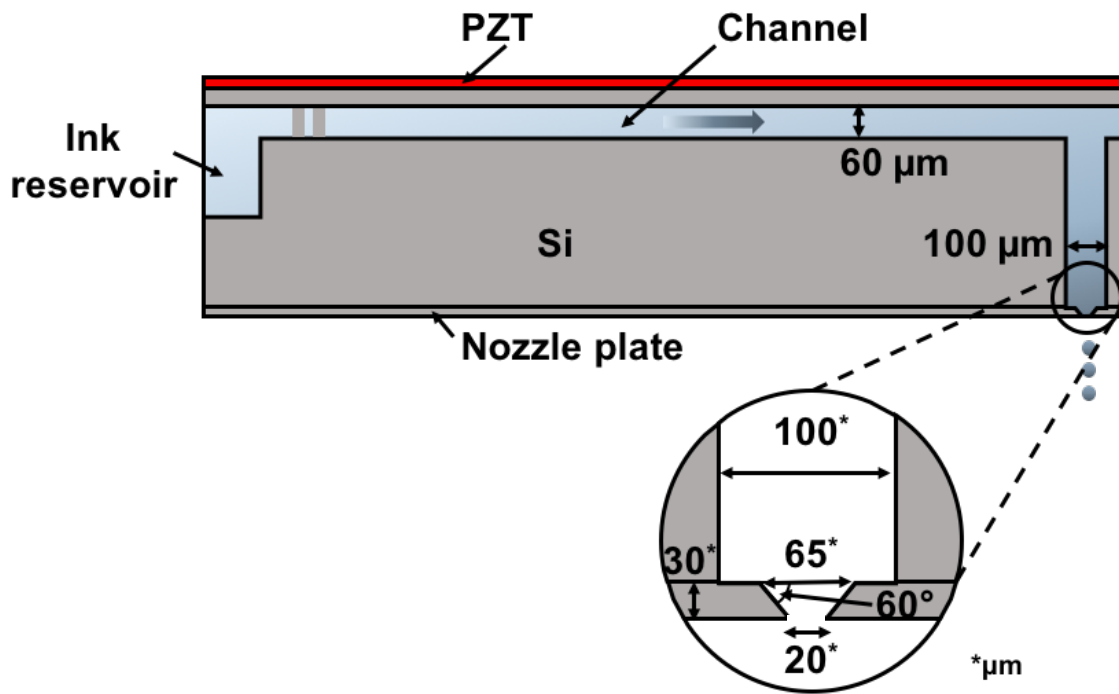


**Figure S3.** Top: Schematic diagram of the Diamatix printhead. Bottom: SEM images of printhead cross section (left) and a close up of the nozzle (right), with relevant dimensions noted.

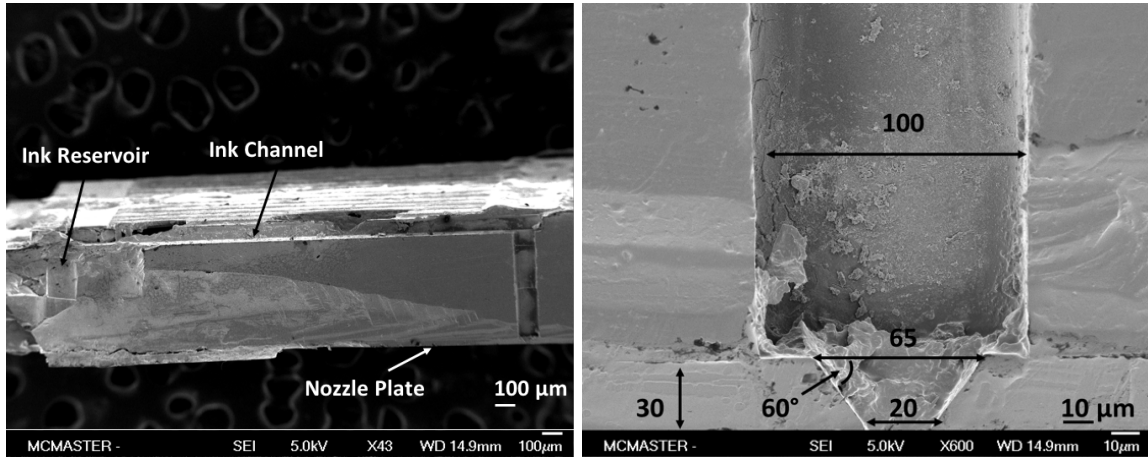


**Figure S4.** SEM Images of a Dimatix printhead and nozzle.

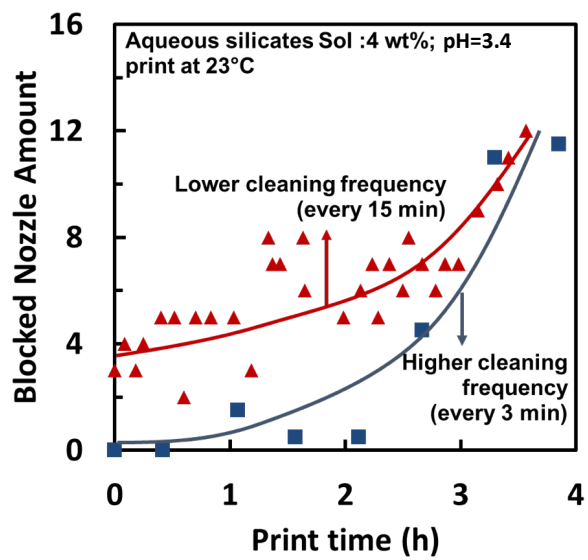


**Figure S5.** A comparison of the clogged nozzle amount for two different cleaning cycle frequencies using the pH 3.4 silica ink.

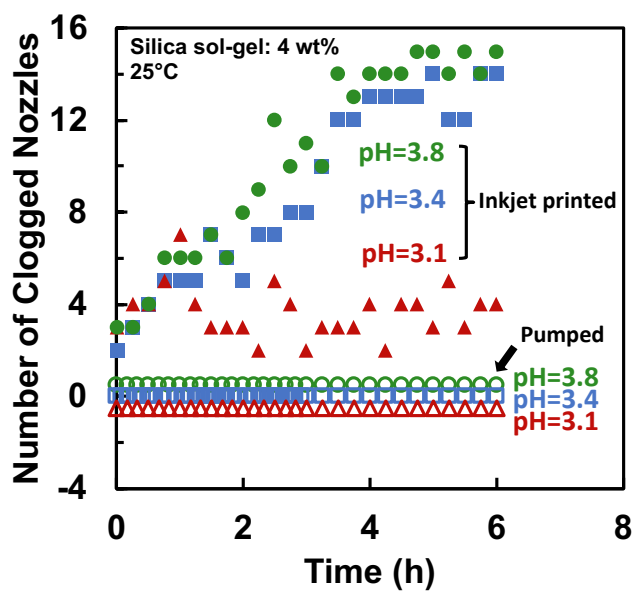


**Figure S6.** A comparison of printhead clogging by silica sol using jetting versus pumping the ink through a passive printhead. Flow rate with pumping was 2.4 mL/min corresponding to a Reynolds number of 4.3 in each nozzle opening. The “pH = 3.4” and “pH = 3.1” pumping results were shifted down from zero for clarity.

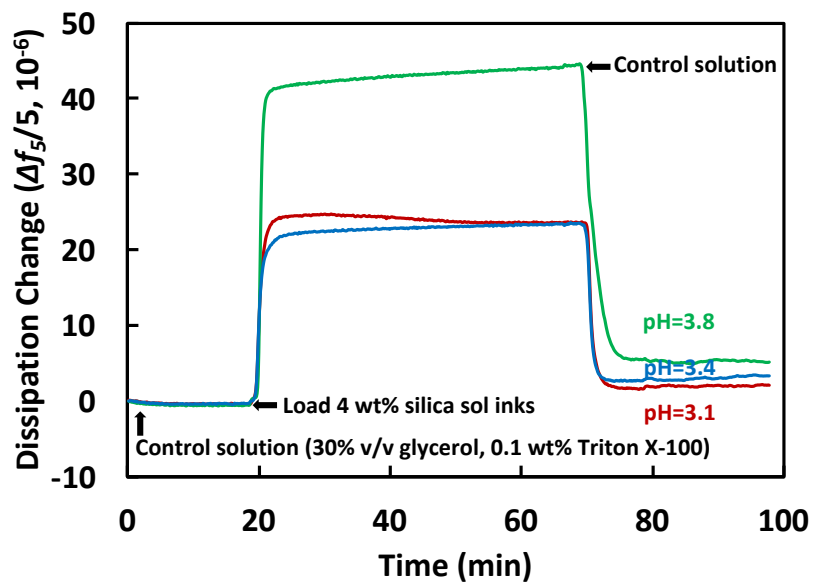


**Figure S7.** The dissipation change of three silica sol inks on a silica QCM-D sensor surface as a function of time.

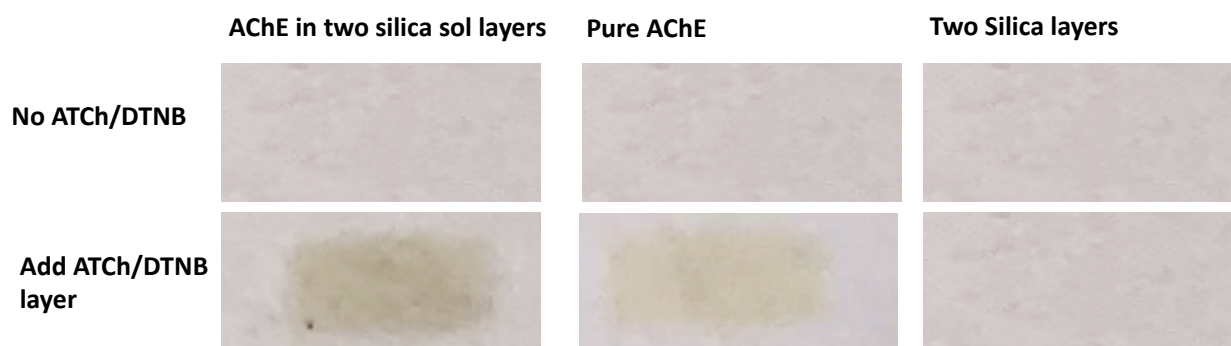


**Figure S8.** Comparison of printing different materials on Whatman #1 filter paper after applying ATCh/DTNB mixture.

The Sauerbrey mass of different pH value

$$S := \begin{bmatrix} 10 \\ 8.5 \\ 7 \end{bmatrix} \frac{mg}{m \cdot m} \quad \begin{array}{l} \text{pH}=3.8 \\ \text{pH}=3.4 \\ \text{pH}=3.1 \end{array}$$

$$D_{silica\_sensor} := 14 \text{ mm}$$

$$Area_{sensor} := \pi \cdot \left( \frac{D_{silica\_sensor}}{2} \right)^2 = (1.539 \cdot 10^{-4}) \text{ m}^2$$

$$m := S \cdot Area_{sensor} = \begin{bmatrix} 1.539 \cdot 10^{-6} \\ 1.308 \cdot 10^{-6} \\ 1.078 \cdot 10^{-6} \end{bmatrix} \text{ gm}$$

silica sol properties:

$$D_{silica} := 25 \text{ nm}$$

$$\rho_{silica\_sol} := 1.4 \frac{gm}{mL} \quad \text{Ref, Wang, J., et al. (2014). Chemistry of materials 26(5): 1941-1947.}$$

$$M_{silica\_sol} := \frac{4}{3} \cdot \pi \cdot \left( \frac{D_{silica}}{2} \right)^3 \cdot \rho_{silica\_sol} = (1.145 \cdot 10^{-17}) \text{ gm}$$

$$Area_{silica\_sol} := \pi \cdot \left( \frac{D_{silica}}{2} \right)^2 = (4.909 \cdot 10^{-16}) \text{ m}^2$$

Coverage

$$C := \frac{m}{M_{silica\_sol}} \cdot \frac{Area_{silica\_sol}}{Area_{sensor}} = \begin{bmatrix} 0.429 \\ 0.364 \\ 0.3 \end{bmatrix}$$

## *Chapter 3*

### **Model Nanoparticle Inks Inkjet Printing**

---

In this chapter, the clogging mechanisms of different nanoparticle-based inks during the inkjet printing process were investigated. These nanoparticles vary with particle sizes, surface properties, and softness. The depositing submonolayer by hydrophobic nanoparticles on printhead surface cause clogging problems by inducing the air bubbles during inkjet printing. This chapter is to show various printing results with different nanoparticle inks for later printing expensive bioagents.

The experiment designs and data collection were conducted by me with the assistance with my summer student Omar Dahhan. I analyzed the data and wrote the draft. Dr. Robert Pelton, Dr. Carlos Filipe and Dr. John Brennan contributed with vital discussion. Dr. Robert Pelton also helped me re-write parts of the draft as necessary.

This chapter and the supporting information are allowed to reprint with permission from *Langmuir* provided by American Chemical Society.

#### **Deposited Nanoparticles Can Promote Air Clogging of Piezoelectric Inkjet Printhead Nozzles**

Yuanhua Li, Omar Dahhan, Carlos D. M. Filipe, John D. Brennan, Robert H. Pelton

*Langmuir*, 2019, 35 (16), 5517-5524

**DOI:** 10.1021/acs.langmuir.8b04335

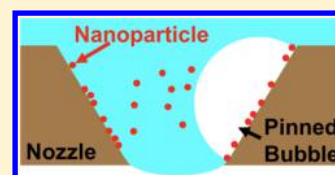
# Deposited Nanoparticles Can Promote Air Clogging of Piezoelectric Inkjet Printhead Nozzles

Yuanhua Li,<sup>†</sup> Omar Dahhan,<sup>†</sup> Carlos D. M. Filipe,<sup>†</sup> John D. Brennan,<sup>‡</sup> and Robert H. Pelton<sup>\*,†</sup><sup>†</sup>Department of Chemical Engineering and <sup>‡</sup>Department of Chemistry & Chemical Biology, McMaster University, Hamilton, Ontario L8S 4L7, Canada

## Supporting Information

**ABSTRACT:** Piezoelectric inkjet printing is susceptible to printhead clogging when printing with inks that contain dispersed particles. This paper investigates the mechanisms by which 28–530 nm nanoparticle dispersions induce printhead clogging without forming large aggregates or thick deposited layers on printhead surfaces. Printing experiments were combined with nanoparticle deposition studies and with experiments where inks were pumped through printheads at a constant flow rate with a syringe pump. Submonolayer coverages of hydrophobic cationic polystyrene nanoparticles adhering to printhead surfaces

promote rapid clogging by trapped air that enters from the nozzle opening. We propose that the deposited particles distort the shape of the ink/air meniscus, possibly causing air entrainment, and promote air bubble adhesion to the interior printhead surfaces. The printer's purge-blot cleaning procedure removes air clogs, but the clogs quickly reform when printing is resumed because the adsorbed nanoparticles are not removed by the cleaning procedure. Nondepositing anionic hydrophobic nanoparticles cause much less clogging, possibly because of filtration of trace large aggregates. Colloidal stability is a necessary but not sufficient criterion for ink dispersions; the ink particles must not adsorb onto the printhead surfaces. Thus, alternate surface chemistries for the printhead and ink particle surfaces may be required to print hydrophobic ink materials.



## INTRODUCTION

Piezoelectric inkjet printing is an ideal method for dispensing expensive and sensitive reagents during the fabrication of biosensors.<sup>1,2</sup> Inks that are homogenous solutions generally display trouble-free printing behaviors, provided that the surface tension and viscosity are within the limits prescribed by the manufacturer. In contrast, inks containing dispersed particles can induce significant printhead clogging. We recently reported results of a detailed investigation of the mechanism by which the silica sol inks induced clogging.<sup>3</sup> If the pH of the silica sol was greater than 3.1, silica nanoparticles formed multilayer deposits on the inside surfaces of the printhead. With time, large sheets of silica deposits were released and clogged the printhead nozzles. Furthermore, evidence suggested that deposits were released from the vibrating transducer surface during printing. Herein, we expand our investigation of clogging mechanisms to include model inks that are dilute, colloidally stable nanoparticle dispersions.

Dressaire and Sauret gave an excellent summary of microfluidic clogging research.<sup>4</sup> They proposed three clogging mechanisms: (1) filtration (sieving), where particles larger than the channels are trapped, partially or completely blocking the flow;<sup>5</sup> (2) thick deposition (aggregation), where colloidal particles form aggregates in the liquid phase and spontaneously deposit onto channel surfaces, decreasing orifice diameters,<sup>6,7</sup> and, (3) jamming (bridging) where a cluster of particles in a constriction become mechanically trapped, blocking flow. Jamming, in contrast to deposition, is a printhead failure mechanism, where the particle/particle and particle/wall interactions are repulsive. The requirement for jamming is the

presence of multiple particles near a constriction.<sup>8</sup> Note, the terms in brackets are Dressaire's nomenclature. In addition to these three mechanisms, we add (4) air inhalation, where air bubbles enter the printhead via the printhead nozzle. Ideally, air bubbles that enter the nozzle during the inhalation step are immediately exhaled when flow is reversed. If the air bubbles are retained in the printhead, they can grow and block flow.<sup>9–13</sup>

In summary, the clogging literature teaches that the dispersed particle size in inks should be much smaller than the size of restrictions in the ink path; the ink colloids should be colloidally stable and resistant to deposition on printhead surfaces; the volume fraction of dispersed solids should be far below the jamming limit; and ink layers should not be allowed to buildup on the nozzle plate.

This paper probes the mechanism by which small colloidally stable ink particles can clog large printhead nozzles. We show that sparse layers of deposited nanoparticles near the nozzle openings can induce catastrophic clogging. All evidence suggests that the deposited nanoparticles trap air bubbles entering from the nozzle, and that trapped air is a clogging agent. This is a generic phenomenon which could be operative on any microfluidic device ejecting droplets in air with oscillating pressure-driven flow.

Received: December 31, 2018

Revised: March 28, 2019

Published: March 29, 2019

## EXPERIMENTAL SECTION

**Materials.** Four polystyrene latexes were purchased from Thermo-Fisher Scientific: two were cationic polystyrene amidine latexes, CPS-90 (Cat. # A37313) and CPS-510 (Cat. # A37317) and two were anionic polystyrene latexes, APS-530 (Cat. #S37494) with surface sulfate groups and APS-28 (Cat # C37261) with surface carboxyl groups. AMG-120 is an anionic microgel based upon poly(*N*-isopropylacrylamide), and CMG-450 is a cationic microgel prepared by adsorbing a polyamide epichlorohydrin polymer onto an anionic supporting microgel. Details of the microgels preparation and characterization have been published; AMG-120 has the designation A2 in ref 14 and CMG-450 was designated P69-A12 in ref 15.

**Six Model Inks.** The inks were prepared by diluting a concentrated nanoparticle dispersion in an ink solution, giving a final nanoparticle concentration of 0.02 wt %. The ink solutions were 1 mM NaCl, 30 vol % glycerol, and 0.1 wt % Triton X-100. The pH of the cationic polystyrene latex (CPS) inks was 4.0, whereas the other inks were adjusted to neutral pH.

**Ink Characterization.** For surface tension, a Krüss Drop Shape Analysis System DSA 10 running DSA software (version 1.80.0.2) was used in the pendant drop mode with a no. 18 needle (diameter 1.21 mm). Measurements were recorded after 2 min of drop aging time. Ink viscosities were measured with a Vibro Viscometer (SV-10, A&D Company) with the temperature controlled at 28 °C. The sample size was 10 mL, and the frequency was 30 Hz.

Dynamic light scattering (Model BI-APD, Brookhaven Instruments Corporation) was used to determine the hydrodynamic diameters. The duration of each measurement was 3 min, and the results were analyzed by BIC dynamic light scattering software (Windows 9KDLWS version 3.34) using the EXSAMP model.

**Inkjet Printing.** All printing experiments were performed with a DMP-2800 (Fujifilm Dimatix, Inc.) fitted with a DMC-11610 printhead. Diagrams and photographs of the printhead are shown in Figures 1 and S1 of the Supporting Information. The waveform used to

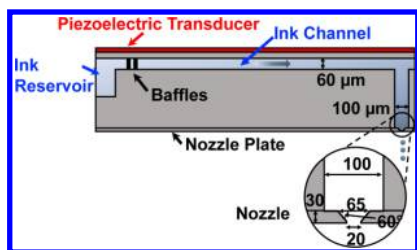


**Figure 1.** Schematic cross-section of the Dimatix printhead, showing the ink flow path to one of the 16 nozzles in the printhead. The piezoelectric transducer induces flow by bending into the ink channel. The backflow baffles are two parallel rows of square posts with <20 μm wide channels between the posts—see SEM image in Figure S4.

drive the printhead was the Dimatix Model Fluid 2—see Figure S2. The firing frequency was set to 5 kHz, and the single nozzle voltage was adjusted to maintain ink velocity between 7 and 10 m/s. Printing runs

were 20 min in duration, followed by a cleaning sequence of 0.5 s purge, followed by the blotting procedure. After the cleaning process, the printhead and its cartridge were stored in a resealable plastic bag at room temperature.

The printing performance was followed two ways: (1) the number of clogged nozzles was measured with the drop watcher system at 5 min intervals and (2) the mass of printed ink over 20 min was determined from the change in mass of the cartridge and the blotting pad.

**Pumping Ink Through Printheads.** The six model inks were pumped through a printhead, not installed in the printer. Steady-state flow was maintained with a syringe pump (NE-1600, New Era Pump System, Inc.) fitted with a 60 mL syringe delivering 1.8 mL/min. The corresponding average flow rate through 16 nozzles during printing was 1.7 mL/min, a value estimated as follows. The mass of particle-free ink was measured over an elapsed printing time of 5 min. The corresponding time when the ink was actually flowing out the nozzles was determined from waveform and piezo frequency. Full details of the calculations are given in the Supporting Information. Images of the ink streams leaving the printhead were captured with an iPhone camera—see Figure S3.

**Nanoparticle Deposition on QCM-D Silica Sensors.** Quartz crystal microbalance measurements (QCM-D, Q-Sense E4, Gothenburg, Sweden) were used to measure the deposition of nanoparticles on a silica sensor. The flow rate was 0.1 mL/min. Ink solution (i.e., ink without nanoparticles) was pumped through the silica sensor for at least 30 min before introducing the inks. The coverages (mass/area) of adsorbed nanoparticles were calculated with the Sauerbrey equation.

**Contact Angle—Polystyrene Films from Nanoparticles.** Polystyrene nanoparticle samples were dried and dissolved in tetrahydrofuran (THF) (0.65 wt %). The solutions were spin coated (SPIN 150 Wafer Spinner running rev: 3.25 software) on glass at 3000 rpm for 90 s, giving thick smooth films. The water contact angles were measured with a Krüss Drop Shape Analysis System DSA 10 (version 1.80.0.2). Each measurement was repeated three times. The water contact angles are a measure of the nanoparticle hydrophobicity insofar as the function group density on the thin films matches the surface chemistry of the parent nanoparticles.

**Contact Angle—Glass with Adsorbed Nanoparticles.** Glass coverslips (VWR, Borosilicate glass, 18 × 18 mm) were cleaned by 5 min exposure to UV/ozone (ProCleaner Bioforce Nanosciences, Inc.). The cleaned coverslips were immersed for 1 h in 10 mL of model inks in a 20 mL glass vial without mixing for 1 h at room temperature. Weakly bound nanoparticles were removed by soaking in 1 L of water in a beaker for 1 h. The coverslips were dried by holding over a flow of nitrogen gas. Sessile drops of ink solution were formed with a #26S stainless steel needle giving a typical volume of 2 μL. Two min after forming the sessile drops, contact angles were measured.

**Scanning Electron Microscopy Imaging.** Dry glass coverslips and QCM-D silica sensors with adsorbed nanoparticles were coated with a 5 nm platinum layer. These samples were examined using a scanning electron microscope (JEOL 7000F). The densities of adsorbed nanoparticles were estimated by ImageJ software (Version 1.51s).

**Optical Microscopy.** An Axioplan microscope (Carl Zeiss Microscopy, LLC) fitted with a 10x objective and a camera (Excelis

**Table 1. The Properties of Six Model Inks<sup>a</sup>**

name	description	diam., PDI (nm)	E.M. ( $10^{-8}$ m <sup>2</sup> /V s)	surface tension (mN/m)	viscosity (mPa·s)	water contact angle (deg)
AMG-120	anionic microgel	120, 0.08	$-0.6 \pm 0.05$	$28 \pm 0.4$	$4.7 \pm 0.06$	
CMG-450	cationic microgel	450, 0.13	$+1.1 \pm 0.07$	$30 \pm 0.5$	$5.2 \pm 0.07$	
APS-530	anionic polystyrene	485, 0.15	$-0.9 \pm 0.05$	$31 \pm 0.5$	$5.5 \pm 0.04$	$72 \pm 0.2$
APS-28	anionic polystyrene	28, 0.1	$-1.2 \pm 0.03$	$27 \pm 0.4$	$5.8 \pm 0.05$	$69 \pm 0.2$
CPS-90	cationic polystyrene	90, 0.04	$+0.8 \pm 0.03$	$32 \pm 0.6$	$5.4 \pm 0.03$	$70 \pm 0.5$
CPS-510	cationic polystyrene	448, 0.15	$+0.5 \pm 0.02$	$30 \pm 0.7$	$5.7 \pm 0.05$	$73 \pm 0.3$

<sup>a</sup>E.M. is the electrophoretic mobility. The names of polystyrene particles include the average diameters given by the supplier. The nanoparticles were dispersed in 1 mM NaCl, 30 vol % glycerol, 0.1 wt % Triton X-100. All inks were adjusted to pH 7 except for CPS inks, which were at pH 4. Water contact angle measurements were performed on smooth polystyrene films.

HD, AU-300-HD) was used to examine the nozzles. After printing with model inks, the printhead was flushed with the background solution and dried in an ambient environment. Optical micrographs were taken with bright field illumination with polarization in a reflective mode.

## RESULTS AND DISCUSSION

**Model Inks.** Six model inks were prepared as 0.02 wt % nanoparticles dispersions in ink solutions (1 mM NaCl, 30 vol % glycerol, and 0.1 wt % Triton X-100). The pH of the CPS inks was 4, whereas the other inks were adjusted to neutral pH. Some ink properties are summarized in Table 1. The microgels are hydrophilic,<sup>16</sup> deformable particles that are colloidally stabilized by both electrostatic and steric mechanisms. In contrast, the polystyrene particles are hydrophobic and are electrostatically stabilized. The average diameters listed in Table 1 were measured by DLS. The names of polystyrene latexes include the diameter given by the suppliers. For APS-530 and CPS-510, the DLS averages were less than the suppliers values and the PDIs were high, possibly indicating some aggregation. The average particle diameters did not change significantly with storage time.

The water contact angle measurements in Table 1 were performed on smooth polymer films formed by dissolving the polystyrene nanoparticles in THF and spin coating the polymer solution. The values range from 69 to 73, indicating significant hydrophobicity as expected for polystyrene. To the extent that the surface functional groups on films represent the surface chemistries of the nanoparticles, these contact angles are a measure of nanoparticle hydrophobicity. The microgels are hydrophilic, and contact angles are not a good indicator of the surface energy of these gels.<sup>16</sup>

**Inkjet Printing Model Inks.** All printing experiments were performed with a DMP-2800 piezoelectric inkjet printer (Fujifilm Dimatix, Inc.) fitted with a DMC-11610 printhead. Figure 1 shows a schematic diagram of the printhead, and photographs of the printhead are shown in Figure S1 of the Supporting Information. Each printhead has a row of 16 nozzles each with  $20 \times 20 \mu\text{m}^2$  nozzle openings. A camera on the printer facilitated real-time monitoring of the number of clogged nozzles.

Figure 1 includes a drawing showing the nozzle geometry which has the shape of a hollow square frustum. The flow versus time behavior through a nozzle is complex, and is determined partly by the printing frequency (5 kHz) and the time-dependent piezoelectric actuation signals (see Figure S2 for an image of the waveform setup screen on the Dimatix). On the basis of the setup parameters, we estimated that the average volumetric flow rate through the 16 nozzles during the short drop ejection time was 1.7 mL/min, which corresponds to a Reynolds number of 10 (for details see the Supporting Information). The nozzle opening was a  $20 \mu\text{m}$  square, and for the ink, CPS-510, containing the largest particles, the ratio of the particle diameter to nozzle width was about 0.026.

Figure 2 compares the printing performance of CPS-90, the most clogging ink, with APS-28, which is the least troublesome. The y-axis shows the number of unblocked nozzles up to a maximum of 16. The x-axis labels correspond to six consecutive printing runs performed with the same printhead. The first three print runs were performed on day 1. After each printing, the printhead was given a purge-blot cleaning cycle and the printhead was stored in a sealed plastic bag for 3 h before the next printing run. After three printings, the printhead, containing ink, was stored for 5 days before the final set of

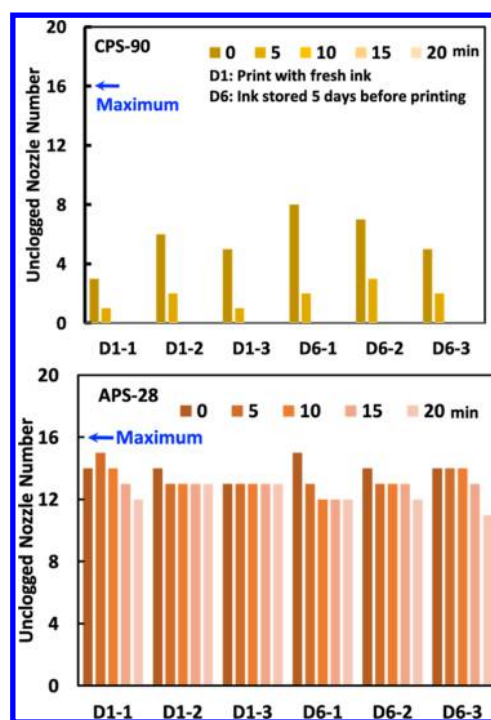


**Figure 2.** Nozzle clogging by CPS-90, an ink with CPS, and APS-28, an ink with anionic polystyrene latex. Each ink/printhead combination underwent six print runs, the first three printing runs were made on day 1 and the last three on day 6. The “0” time reading was made about 20 s after initiating jetting. The printheads were cleaned with purge-blot cycle after every 20 min print run. The anionic ink gave much less clogging than the cationic ink.

three printing runs, which were a test of the ink colloidal stability. Note the “0” time measurements were made approximately 20 s after starting jetting.

Printing performance was poor with the cationic CPS-90 ink. For every 20 min print run, all of the nozzles were completely clogged between 5 and 10 min. However, in every case the purge-blot cleaning procedure cleared the clogs, as evidenced by the restoration of the “0” time result. Because cleaning was effective, the six repeated print runs gave similar results.

The anionic APS-28 gave much better performance. However, in every case, at least 1 nozzle was clogged. Like the cationic ink, the purge-blot cleaning rejuvenated the printhead, giving six similar printing runs. In view of the stochastic nature of the clogging, the experiments were exceptionally reproducible.

The clogging performance of the six model inks are compared in Figure 3 where for each ink, the three printing run results for day 1 were averaged. None of the model inks was perfect. In every case, at least one nozzle was clogged. The two CPSs and the cationic microgel showed the greatest clogging. By contrast, the small anionic APS-28 was the best performing, with the anionic microgel second best. The large anionic APS-530 ink performed better than the cationic nanoparticle inks but far worse than the other anionic nanoparticle inks. Similar results were recorded for the day 6 measurement—see Figure S5. The error bars in Figure 3 denote the standard deviation of three consecutive measurements with the same printhead.

We also measured the mass of ink printed in 20 min, and the results for the six inks are compared in Figure 4. The theoretical maximum printed mass was estimated to be about 1 g based on  $10 \text{ pL drop volume} \times 16 \text{ nozzles} \times 5000 \text{ Hz} \times 20 \text{ min}$ . None of the inks gave the theoretical printed mass, which is consistent

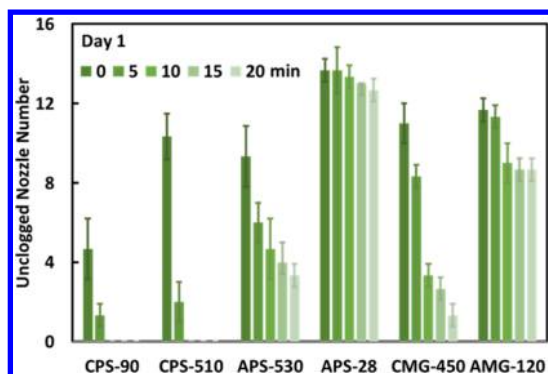


**Figure 3.** Comparison of the printing performance of the six model inks. Each bar shows the average and standard deviation of three consecutive day 1 printing runs, each separated by a purge-blot cleaning cycle. The “0” time reading was made about 20 s after initiating jetting.

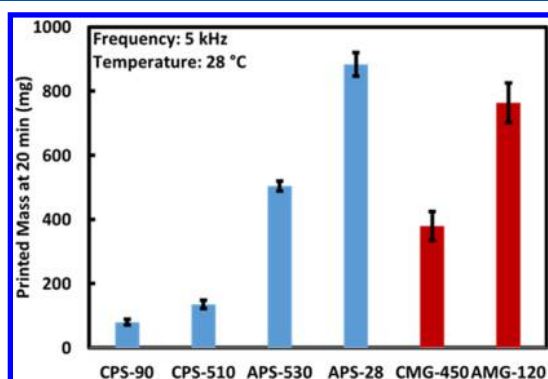
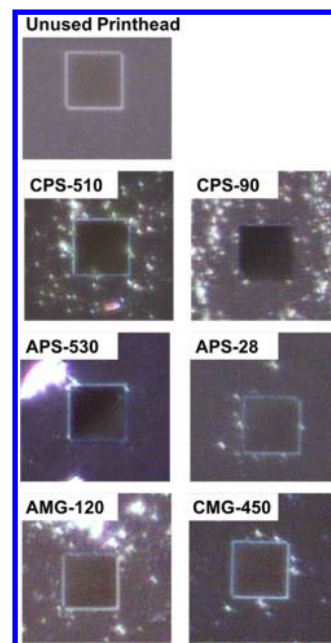


**Figure 4.** The average total mass of printed ink over 20 min for the three printing runs with six inks in day 1. The blue bars denote polystyrene latex inks, whereas the red bars are the microgel inks. The error bars portray the standard deviations of triplicate measurements.

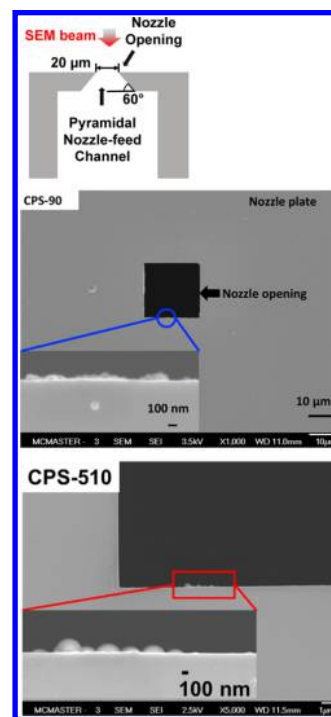
with observation that at least one nozzle was blocked in every experiment (see Figure 3).

Figure 5 shows optical images of the six nozzles from six printheads after the sixth printing run on day 6. Before imaging, the printhead underwent a purge-blot cleaning, a rinse with particle-free printing solution, followed by a pure water rinse. Whereas all of the nozzles showed nanoparticle deposits on the nozzle plate surrounding the nozzles, there was no evidence of large aggregates blocking the nozzle.

According to the Dimatix printer manual, the purge process removes air trapped in the printhead. Does the purge cleaning cycle also remove adsorbed nanoparticles? Scanning electron microscopy (SEM) was used to determine if any CPS-90 or CPS-510 particles remained on the inside surfaces leading to the nozzle opening after cleaning. The drawing in Figure 6 shows a cross-sectional diagram of the pyramidal nozzle-feed channel leading to the nozzle opening. Because of the slope of the nozzle-feed channel, SEM can only “see” adsorbed nanoparticles near the nozzle opening. Figure 6 shows SEM images of the nozzle openings after printing with the two cationic polystyrene inks, CPS-510 and CPS-90. In both cases, sub-monolayer deposits of polystyrene particles are present on the nozzle-feed channel near the nozzle opening. In summary, the clogging results suggest that purge-blot washing removes trapped air, but the SEM images show that purging does not remove all of the adsorbed cationic particles.



**Figure 5.** Optical micrographs of nozzles after 20 min printing after cleaning. The white spots are clumps of nanoparticles. The square nozzle openings are 20  $\mu\text{m}$  square.



**Figure 6.** SEM images showing CPS-510 and CPS-90 nanoparticles adsorbed inside the printhead near the nozzle opening. Because of the angle of the pyramidal nozzle-feed channel, only the nanoparticles deposited near the nozzle opening were visible to the SEM beam. The higher magnification inserts show images of adsorbed nanoparticles just below the nozzle opening. These images showed that purge-blot cleaning did not removal all, or possibly any, of the deposited nanoparticles.

Inspired by the literature, we hypothesized that small air bubbles were inhaled during the oscillatory flow during printing and adsorbed on the nanoparticle-coated printhead surfaces.<sup>9–12</sup> To test this hypothesis, APS-28, CPS-510, and CPS-

90 inks were pumped through the printheads at a constant rate with a syringe pump—see a photograph of the apparatus in Figure S3. With steady flow pumping, air inhalation from the nozzle opening is impossible. The pumping rate was set to give the volumetric flow rate of 1.8 mL/min in the pumping experiments in an attempt to match the average flow rates during jetted drop ejection. Therefore, hydrodynamic forces on deposited particles in the jetting and pumping should be similar.

The results of the pumping experiments are shown as photographs in Figure 7. After 20 min pumping, CPS-510 gave

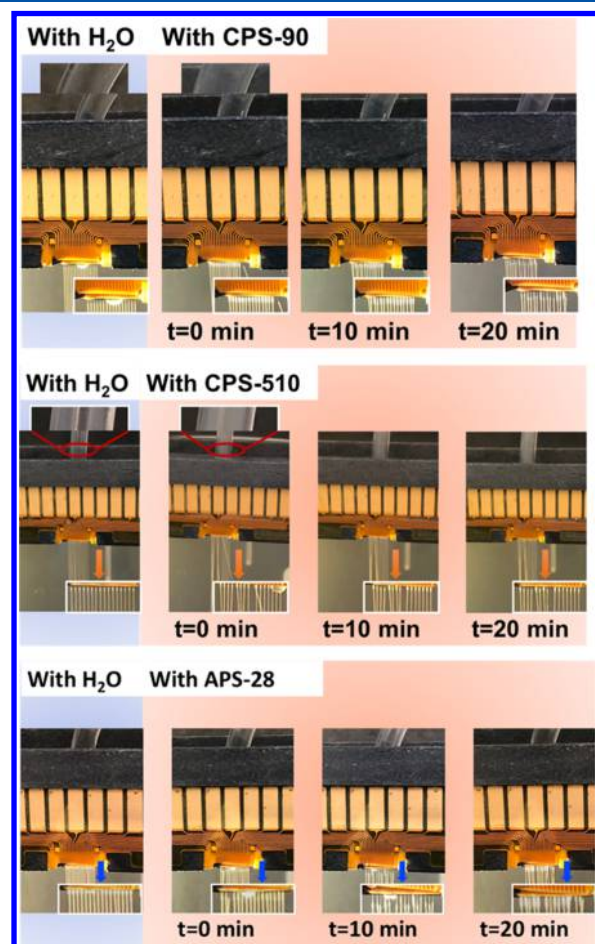


**Figure 7.** Images of CPS-90, CPS-510, and APS-28 inks being pumped (1.8 mL/min) through the Dimatix printhead. With pumping, most of the nozzles were functioning after 20 min.

one blocked nozzle and one nozzle with a deflected stream. This result is in marked contrast to the printing results (Figure 3), where all nozzles were blocked before 10 min printing. With the small cationic CPS-90, the comparison was more dramatic. With pumping, there was some stream deflection, however, none of the nozzles was blocked, whereas with printing, all nozzles were blocked by 10 min. Finally, in pumping experiments, the APS-28, the best printing ink, gave some distorted streams and blocked nozzles—it was no better than CPS-90, the worst printing ink. To summarize, the pumping experiments gave much better performance compared to normal jetting, suggesting that some of the clogging is associated with the oscillatory flow during printing.

**Ink Deposition on Silica.** The results in Figure 6 suggest that clogging may be related to nanoparticle adsorption on the

interior printhead surfaces. However, nanoparticle deposition on printheads is difficult to measure quantitatively, thus, we employed surrogate surfaces for adsorption studies. Dimatix printheads are fabricated from silicon, and the exposed surfaces will be oxidized to silica. Quartz crystal microbalance measurements were used to measure the deposition of ink nanoparticles onto silica QCM-D sensor surfaces. Figure 8 summarizes the

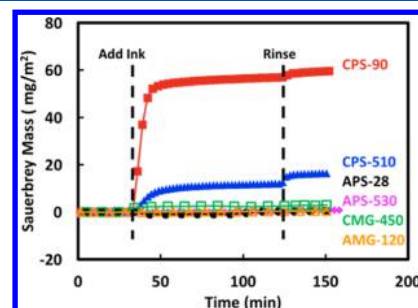


**Figure 8.** The deposition of ink nanoparticles onto QCM-D silica sensors. The inks were added without dilution. Ink solutions (i.e., inks with no nanoparticles) were used for initial conditioning and for the rinsing step at the end. The Sauerbrey mass is based on the third overtone, and the corresponding dissipation curves are shown in Figure S6 and  $\Delta D/\Delta f$  ratios are shown in Table S1 in the Supporting Information.

QCM-D results. The Sauerbrey equation was used to convert frequency shifts to coverages of adsorbed nanoparticles. The corresponding dissipation results, in Figure S6 and Table S1, reveal that the Sauerbrey model is valid for the hard polystyrene particles, whereas application of Sauerbrey to the microgel results was marginal. The soft, water-swollen microgels displayed more viscous dissipation than did the hard polystyrene particles.

Each experiment started with 40 min of flowing ink solution (no dispersed particles), followed by the ink dispersion. After 125 min, the QCM-D sensor was rinsed with ink solution. Only the three cationic nanoparticles displayed significant adsorption onto silica. CPS-90 gave the highest coverage, with the much larger CPS-510 nearly 10 times less. Finally, the cationic microgel had a small adsorption tendency, whereas the anionic microgels and the polystyrene nanoparticles did not adsorb.

**Ink Deposition on Glass Coverslips.** In order to perform sessile drop contact angle measurements, we exposed cleaned glass coverslips to the inks to promote nanoparticle adsorption. Figure S7 compares SEM images of the QCM-D surface to the glass surface after saturation adsorption of CPS-90 CPS. The coverages, estimated by image analysis, were remarkably similar—30% for the silica sensor and 33% for the glass slide. These results are typical of the previously reported cationic latex deposition studies on glass.<sup>17</sup>

Figure 9 compares SEM images of glass coverslips after exposure to the six inks for sufficient time to give saturation coverage. The insets show images of ink solution sessile drops on coverslips. Paralleling the QCM-D experiments, CPS-90 gave the highest coverage. The larger cationic CPS-510 appeared clumped together. As the ink showed no signs of aggregation, we believe that latex adhesion to glass was insufficient to overcome capillary forces during drying, which drew particles together forming 2-D clumps on the glass. The cationic microgel CMG-450 also appeared to have a few very small aggregates; these were present in the parent microgel dispersion.<sup>15</sup>

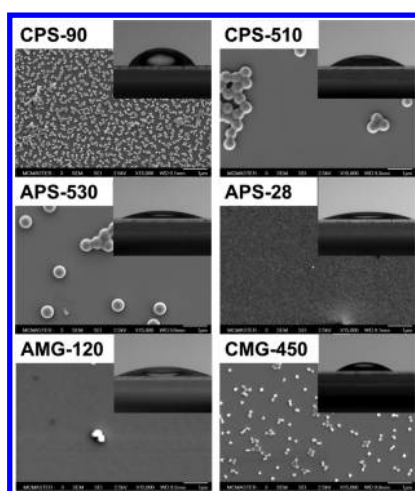


**Figure 9.** SEMs of glass surfaces after exposure to the six model inks. The inset shows images of sessile drops of ink solution on the dried nanoparticle-treated glass surfaces.

The anionic microgel AMG-120 and the smaller anionic polystyrene, APS-28 showed virtually no adsorption, agreeing with the QCM-D results (Figure 8). The anionic APS-510 did not deposit in the QCM-D experiments, however, there was some deposited particles on the glass coverslip including one aggregate.

The advancing contact angle of the ink solutions on dry, nanoparticle decorated coverslips were measured and are summarized in Table 2. Exposure of the glass coverslips to

**Table 2. The Contact Angle of Ink Solutions (i.e., Inks without Dispersed Nanoparticles) on Glass Coverslips with Adsorbed Nanoparticles<sup>a</sup>**

nanoparticle	contact angle (deg)	pinning
none	10 ± 1.0	no
CPS-90	40 ± 2	yes
CPS-510	28 ± 0.6	yes
CMG-450	25 ± 1	yes
APS-530	17 ± 0.2	yes
APS-28	14 ± 0.3	no
AMG-120	18 ± 0.4	no

<sup>a</sup>Pinning refers to sessile drops whose three-phase contact line does not smoothly contract when liquid is removed from the drop.

anionic nanoparticles gave very low coverages (Figure 9), therefore the contact angles of ink solutions were close to the value for clean coverslips not exposed to nanoparticles. CPS-90 gave the highest angle, reflecting the high (33%) coverage and the hydrophobic character of polystyrene. Previously, we have shown that hydrophilic glass surfaces decorated with polystyrene nanoparticles do not display reversible wetting behaviors.<sup>17</sup> When water is removed with a needle from a sessile water drop to give a receding contact angle, the water drop does not contract. Instead, the drop footprint is fixed and the receding contact angle decreases as water is removed. This behavior is called “pinning”.<sup>17,18</sup> In the current work, coverslips treated with the three cationic inks or with APS-530 gave pinned ink solution sessile drops. Pinning corresponded to the most troublesome inks.

Finally, the contact angle results (Table 2), nanoparticle adsorption results (Figure 8), and printing performance results

(Figure 4) are compared in Figure 10. Each vertical pair of points corresponds to a specific ink. The three independent types of

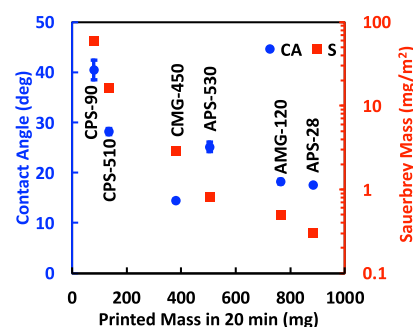


**Figure 10.** Relating the contact angle of the printing solution (no nanoparticles) on dry coverslips previously exposed to inks and the mass coverage of adsorbed nanoparticles on QCM-D silica sensors to the printing performance measured by mass transferred in 20 min. (●) contact angle; (□) Sauerbrey mass.

measurements are correlated. The best inks have the lowest tendency to deposit, giving the lowest contact angles.

**Clogging Mechanisms.** The Dimatix 2800 is an excellent printer, which we have used for years with great results. However, printhead clogging can occur. The inks in this study were chosen to be problematic with a view to understanding clogging mechanisms. Any proposed clogging mechanism must explain the main observations that include the following: all six inks showed some level of clogging; neither SEM nor optical microscopy showed any examples of thick layers of adsorbed particles or large aggregates trapped in a nozzle opening, blocking flow; the cationic nanoparticles that spontaneously adsorbed on silica were the most potent cloggers; the cationic polystyrene nanoparticles gave much less clogging when pumped; purge-blot cleaning removed clogs but did not dislodge adsorbed nanoparticles; and, the poorest printing inks also displayed pinning during attempts to measure receding contact angles.

Of the four clogging mechanisms described in the introduction (filtration, thick deposit formation, jamming, and air inhalation), we can immediately reject thick deposit formation because no thick deposits were observed. Jamming also seems unlikely as the particle volume fractions were low,  $\sim 0.0002$  for the polystyrene inks. The ratio of particle diameter to orifice diameter is an important parameter for jamming.<sup>4,5,8,19,20</sup> APS-530 was the largest nanoparticle and the corresponding ratio is  $0.530/20 = 0.027$ . However, the literature suggests that the ratio should be 0.3–0.4,<sup>20</sup> an order of magnitude larger than our inks. In summary, jamming and thick deposit formation seem unlikely, leaving filtration and air inhalation. We now link the key findings to the possible clogging mechanisms.

Figure 2 shows that the small anionic polystyrene latex ink gave some clogging. Although aggregates were not visible and dynamic light scattering did not indicate aggregation, it is possible that a low concentration of large aggregates was present in the ink and was trapped by filtration in the baffles (no large aggregates were observed in the nozzles). Sauret et al. recently promoted microfluidic clogging as a tool to analyze the concentration of large aggregates that are difficult to measure by other techniques.<sup>5</sup> Therefore, we propose that filtration of low concentrations of large particles was responsible for the few clogged nozzles with the anionic inks.

The most potent clogging inks were the cationic polystyrene particles that formed sub-monolayer deposits on silica and glass. In another work related to mineral flotation, we have shown that adsorbed polystyrene particles on glass surfaces display four dramatic effects:

1. Pinning of the three-phase contact line was observed when water was withdrawn from a sessile drop on glass with a sparse polystyrene nanoparticle coating.<sup>17</sup> Pinning was also observed with some of the nanoparticle inks listed in Table 2; the inks displaying pinning correspond to the poorest printing inks.
2. Adsorbed polystyrene particles promote the attachment of air bubbles to glass surfaces.<sup>21</sup> It is relatively difficult for an air bubble suspended in water to adhere to a smooth glass surface. In contrast, adsorbed nanoparticles are hydrophobic asperities on more hydrophilic glass surfaces, promoting the formation of glass/water/air three phase contact lines and, thus, bubble adhesion.
3. The force required to dislodge a 50  $\mu\text{m}$  glass bead from a large air bubble was increased by more than two orders of magnitude by adsorbing onto the glass surfaces a sub-monolayer coating of cationic polystyrene particles similar to the CPS-90 particles used herein.<sup>22</sup>
4. CPS particles strongly adhere to glass. Based on AFM-colloid probe measurements, the laminar flow shear rate required to dislodge a 317 nm CPS adsorbed on glass was estimated to be  $2.4 \times 10^6 \text{ s}^{-1}$ .<sup>23</sup> This is a substantial shear rate, which may not be present during jetting. For a given shear rate, the displacement forces on a deposited spherical particle in laminar flow increase with the square of particle radius, so the smallest particles are the least likely to be removed by hydrodynamic forces.<sup>24</sup>

The above three phenomena are most extreme when the polystyrene surfaces are not covered with surfactant or with many hydrophilic groups. The contact angle results for the particles in Tables 1 and 2 suggest that the surfaces of the polystyrene nanoparticles used herein were close to pristine polystyrene. Arguments are now presented to support the hypothesis that a sub-monolayer of adsorbed cationic polystyrene nanoparticles induces air clogging.

A series of papers from the Netherlands has reported detailed experimental and computation studies showing that the alternating directions of ink flow during normal inkjet printing can entrain air bubbles in the ink flowing back into the nozzle feed channel from the nozzle opening.<sup>9–12</sup> This air inhalation process was directly observed by de Jong et al. who used high speed photography and a transparent nozzle on a homemade printhead.<sup>13,25</sup>

The Dimatix printhead also produces oscillatory flow. With electrical stimulation, the piezoelectric element in the printhead bends down forcing the ink to move. The ink can flow in two directions: (1) back through the baffles toward the reservoir and, (2) out of the nozzle as a jetted ink drop (see Figure 1). The Dimatix generates drop volumes of about 10 pL; we do not know the corresponding flow volume through the baffles toward the reservoir. In the reverse cycle, the piezoelectric element retracts, causing ink to flow back into the ink channel from the same two directions—from the reservoir and from the nozzle. Therefore, at the nozzle opening, there is an alternating flow direction of ink through the nozzle at the printing frequency (5 kHz).

The Dutch group also showed that the presence of an ink film on the nozzle plate promotes retention of the entrained bubbles.

They also reported that dust particles adsorbed at the ink/air interface influence air entrainment. Specifically, they state, “It is therefore believed that these particles disturb the normal jetting process by creating an asymmetric meniscus, which then could lead to the entrapment of air.”<sup>10</sup>

Herein, we propose a related mechanism whereby cationic hydrophobic particles adsorb on the surface of the printhead feed channel, pinning and, thus, perturbing the moving meniscus, as well as facilitating the attachment of inhaled bubbles to the printhead wall. Trapped air bubbles were not directly observed because the Dimatix printhead is not transparent. On the other hand, we have much indirect evidence. First, the extreme clogging behaviors of the cationic polystyrene inks were not observed when the inks were pumped through the printhead in steady-state flow, a situation where air cannot not enter from the nozzle opening. Second, extreme clogging was only observed with adsorbing polystyrene nanoparticles. Third, the clogs were easily removed by the Dimatix purge procedure, suggesting that the clogs were air. However, the adsorbed polystyrene particles were not removed, and clogs quickly reformed when printing was resumed.

The role of nanoparticle surface hydrophobicity was not quantitatively evaluated in this work. The water swollen microgels surfaces are less hydrophobic than polystyrene,<sup>16</sup> and the printing results in Figures 3 and 4 show that the microgels were less potent cloggers than the polystyrene particles of similar size and charge.

The ink formulation lessons from this work include the following: ink colloidal stability is not enough for trouble free printing; dispersed particles in ink should have little tendency to deposit on silica surfaces; and because some ink deposition is inevitable, the dispersed ink particles and the printhead must have hydrophilic surfaces.

## CONCLUSIONS

The piezoelectric inkjet printing performances of colloiddally stable nanoparticle inks were systematically investigated in an effort to understand the origin of inkjet printhead clogging. Experiments with six model inks led to the following conclusions:

1. Sub-monolayer coverages of hydrophobic cationic nanoparticles adhering to printhead surfaces promote clogging with trapped air that enters the printhead from the nozzle opening. We propose that the deposited particles distort the shape of the ink/air meniscus, possibly causing air entrainment and promoting air bubble adhesion to the interior printhead surfaces.
2. Nondepositing anionic hydrophobic nanoparticles cause much less clogging, possibly due to filtration of trace large aggregates.
3. The printer's purge-blot cleaning procedure removes air clogs, but clogs quickly reform when printing is resumed because the adsorbed nanoparticles are not removed by the cleaning procedure.
4. A sub-monolayer coating of deposited nanoparticles will induce air bubble clogging if the nanoparticles are as hydrophobic as polystyrene.

## ■ ASSOCIATED CONTENT

### 📄 Supporting Information

The Supporting Information is available free of charge on the ACS Publications website at DOI: [10.1021/acs.langmuir.8b04335](https://doi.org/10.1021/acs.langmuir.8b04335).

Photographs of the Dimatix printhead and cartridge, the setup screen, photographs of experimental setup for pumping ink through the printhead, SEMs of the printhead baffles and nanoparticles deposited on glass, summary of day 6 nozzle printing results, dissipation results for nanoparticle deposition on QCM-D silica sensors, validity of the Sauerbray analysis, and calculation of average flow rate during drop ejection and estimate of the corresponding Reynolds number (PDF)

## ■ AUTHOR INFORMATION

### Corresponding Author

\*E-mail: [peltonrh@mcmaster.ca](mailto:peltonrh@mcmaster.ca).

### ORCID

Carlos D. M. Filipe: 0000-0002-7410-3323

John D. Brennan: 0000-0003-3461-9824

Robert H. Pelton: 0000-0002-8006-0745

### Notes

The authors declare no competing financial interest.

## ■ ACKNOWLEDGMENTS

The authors thank Chris Butcher (Canadian Center for Electron Microscopy, McMaster University) and Marcia Reid (McMaster Health Sciences) for sample preparation and training. Dr. Dong Yang is thanked for providing the microgel dispersions. The authors also thank the Natural Sciences and Engineering Research Council of Canada for funding through the SENTINEL Bioactive Paper Network. We also thank the Canadian Foundation for Innovation and the Ontario Ministry of Research and Innovation for Infrastructure funding to the Biointerfaces Institute. Y.L. acknowledges funding from the China Scholarship Council (CSC). J.D.B. holds the Canada Research Chair in Bioanalytical Chemistry and Biointerfaces. R.H.P. holds the Canada Research Chair in Interfacial Technologies.

## ■ REFERENCES

- (1) Pelton, R. Bioactive Paper - a Low Cost Platform for Diagnostics. *Trends Anal. Chem.* **2009**, *28*, 925–942.
- (2) Yamada, K.; Henares, T. G.; Suzuki, K.; Citterio, D. Paper-Based Inkjet-Printed Microfluidic Analytical Devices. *Angew. Chem., Int. Ed.* **2015**, *54*, S294–S310.
- (3) Li, Y.; Dahhan, O.; Filipe, C. D. M.; Brennan, J. D.; Pelton, R. H. Optimizing Piezoelectric Inkjet Printing of Silica Sols for Biosensor Production. *J. Sol-Gel Sci. Technol.* **2018**, *87*, 657–664.
- (4) Dressaire, E.; Sauret, A. Clogging of Microfluidic Systems. *Soft Matter* **2017**, *13*, 37–48.
- (5) Sauret, A.; Barney, E. C.; Perro, A.; Villermanx, E.; Stone, H. A.; Dressaire, E. Clogging by Sieving in Microchannels: Application to the Detection of Contaminants in Colloidal Suspensions. *Appl. Phys. Lett.* **2014**, *105*, 074101.
- (6) Mustin, B.; Stoeber, B. Deposition of Particles from Polydisperse Suspensions in Microfluidic Systems. *Microfluid. Nanofluid.* **2010**, *9*, 905–913.
- (7) Lee, A.; Sudau, K.; Ahn, K. H.; Lee, S. J.; Willenbacher, N. Optimization of Experimental Parameters to Suppress Nozzle Clogging in Inkjet Printing. *Ind. Eng. Chem. Res.* **2012**, *51*, 13195–13204.

(8) Wyss, H. M.; Blair, D. L.; Morris, J. F.; Stone, H. A.; Weitz, D. A. Mechanism for Clogging of Microchannels. *Phys. Rev. E: Stat., Nonlinear, Soft Matter Phys.* **2006**, *74*, 061402.

(9) Kim, B.-H.; Kim, T.-G.; Lee, T.-K.; Kim, S.; Shin, S.-J.; Kim, S.-J.; Lee, S.-J. Effects of Trapped Air Bubbles on Frequency Responses of the Piezo-Driven Inkjet Printheads and Visualization of the Bubbles Using Synchrotron X-Ray. *Sens. Actuators, A* **2009**, *154*, 132–139.

(10) De Jong, J.; De Bruin, G.; Reinten, H.; Van Den Berg, M.; Wijshoff, H.; Versluis, M.; Lohse, D. Air Entrapment in Piezo-Driven Inkjet Printheads. *J. Acoust. Soc. Am.* **2006**, *120*, 1257–1265.

(11) Beulen, B.; Jong, J. D.; Reinten, H.; Berg, M. V. D.; Wijshoff, H.; Van Dongen, R. Flows on the Nozzle Plate of an Inkjet Printhead. *Exp. Fluids* **2006**, *42*, 217–224.

(12) De Jong, J.; Jeurissen, R.; Borel, H.; van den Berg, M.; Wijshoff, H.; Reinten, H.; Versluis, M.; Prosperetti, A.; Lohse, D. Entrapped Air Bubbles in Piezo-Driven Inkjet Printing: Their Effect on the Droplet Velocity. *Phys. Fluids* **2006**, *18*, 121511.

(13) Wijshoff, H. The Dynamics of the Piezo Inkjet Printhead Operation. *Phys. Rep.* **2010**, *491*, 77–177.

(14) Yang, D.; Gustafsson, E.; Stimpson, T. C.; Esser, A.; Pelton, R. H. Hydrazide-Derivatized Microgels Bond to Wet, Oxidized Cellulose Giving Adhesion without Drying or Curing. *ACS Appl. Mater. Interfaces* **2017**, *9*, 21000–21009.

(15) Yang, D. *Adhesives with Controllable Degradability for Wet Cellulosic Materials* McMaster; Hamilton: Canada, 2018.

(16) Pelton, R. Poly(N-Isopropylacrylamide) (PNIPAM) Is Never Hydrophobic. *J. Colloid Interface Sci.* **2010**, *348*, 673–674.

(17) Yang, S.; Pelton, R. Nanoparticle Flotation Collectors II: The Role of Nanoparticle Hydrophobicity. *Langmuir* **2011**, *27*, 11409–11415.

(18) De Gennes, P. G.; Brochard-Wyart, F.; Quéré, D. *Capillarity and Wetting Phenomena: Drops, Bubbles, Pearls, Waves*; Springer Verlag: New York, 2004.

(19) Goldsztein, G. H.; Santamarina, J. C. Suspension Extraction through an Opening before Clogging. *Appl. Phys. Lett.* **2004**, *85*, 4535–4537.

(20) Sharp, K. V.; Adrian, R. J. On Flow-Blocking Particle Structures in Microtubes. *Microfluid. Nanofluid.* **2005**, *1*, 376–380.

(21) Dong, X.; Gustafsson, E.; Price, M.; Dai, Z.; Xu, M.; Pelton, R. Glass Bead-Bead Collisions Abrade Adsorbed Soft-Shell Polymeric Nanoparticles Leaving Footprints. *Colloids Surf., A* **2017**, *533*, 159–168.

(22) Yang, S.; Pelton, R.; Raegen, A.; Montgomery, M.; Dalnoki-Veress, K. Nanoparticle Flotation Collectors – Mechanisms Behind a New Technology. *Langmuir* **2011**, *27*, 10438–10446.

(23) Dong, X.; Marway, H. S.; Cranston, E. D.; Pelton, R. H. Relating Nanoparticle Shape and Adhesiveness to Performance as Flotation Collectors. *Ind. Eng. Chem. Res.* **2016**, *55*, 9633–9638.

(24) Goldman, A. J.; Cox, R. G.; Brenner, H. Slow Viscous Motion of a Sphere Parallel to a Plane Wall—II Couette Flow. *Chem. Eng. Sci.* **1967**, *22*, 653–660.

(25) De Jong, J.; Versluis, M.; De Bruin, G.; Lohse, D.; Reinten, H.; Van Den Berg, M.; Wijshoff, H.; De Jong, N. Acoustical and Optical Characterization of Air Entrapment in Piezo-Driven Inkjet Printheads. *IEEE Ultrasonics Symposium*, 2005; Vol. 2, p 1270.

## SUPPORTING INFORMATION

### DEPOSITED NANOPARTICLES CAN PROMOTE AIR CLOGGING OF PIEZOELECTRIC INKJET PRINTHEAD NOZZLES

Yuanhua Li, Carlos D.M. Filipe, John D. Brennan, and Robert H. Pelton \*

Department of Chemical Engineering, <sup>a</sup> Department of Chemistry, <sup>b</sup> McMaster University, Hamilton, Ontario, L8S 4L7, Canada

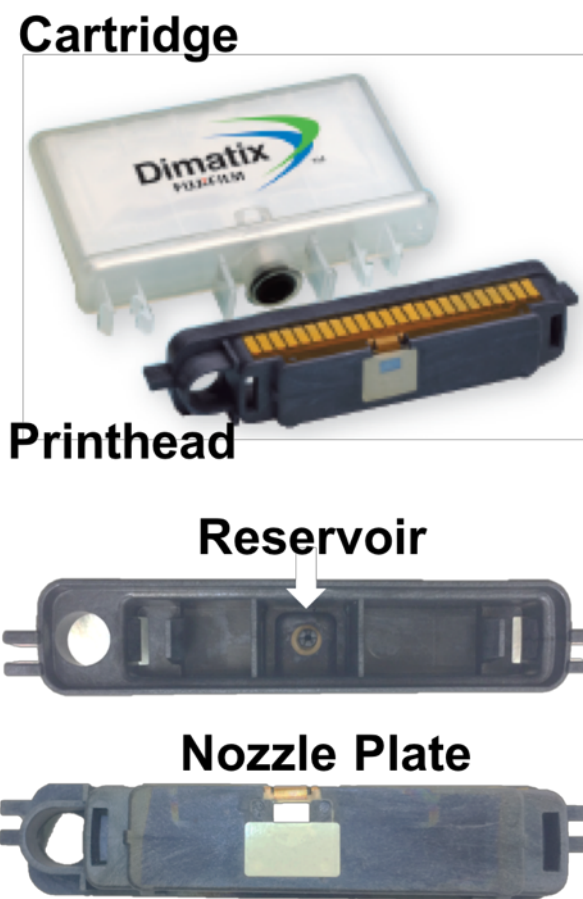
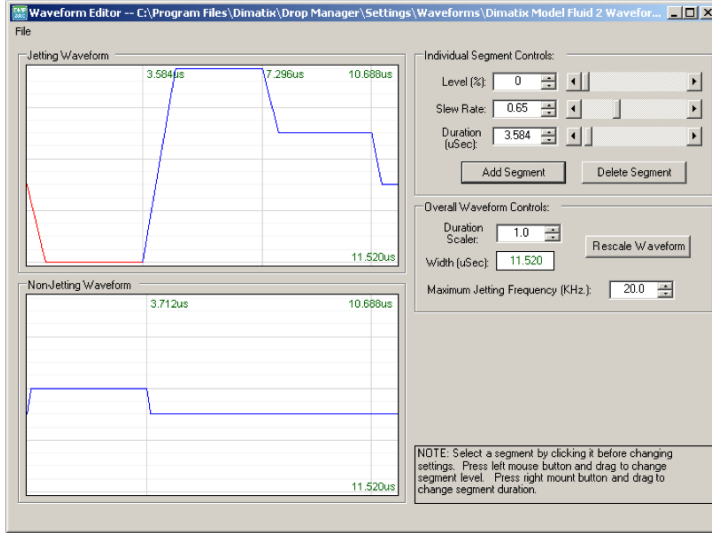


Figure S1 Photographs of a Dimatix printhead and cartridge.

# Waveform Setting



# Cleaning Process Setting

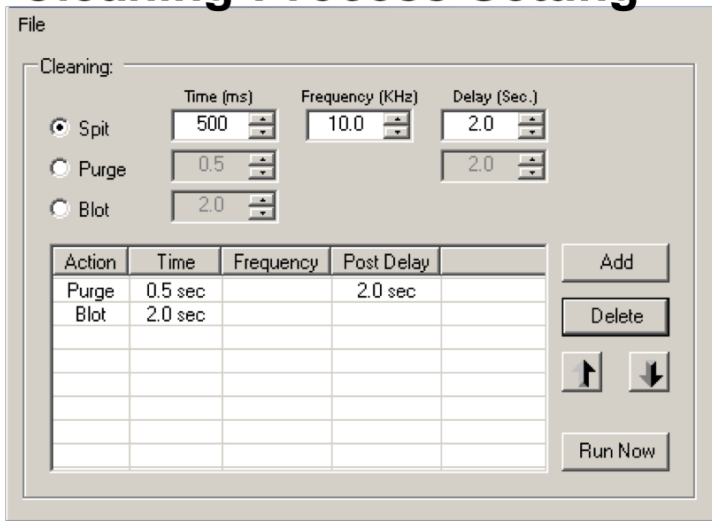


Figure S2 Printing wave form and the cleaning settings.

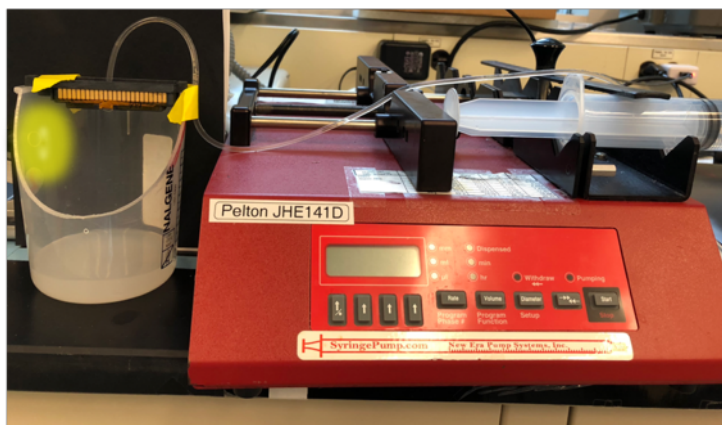


Figure S3 Photographs the experimental setup for pumping ink through a printhead. The syringe pump drove a steady flow of ink and images of the flow from the 16 nozzles were captured with an iPhone camera.

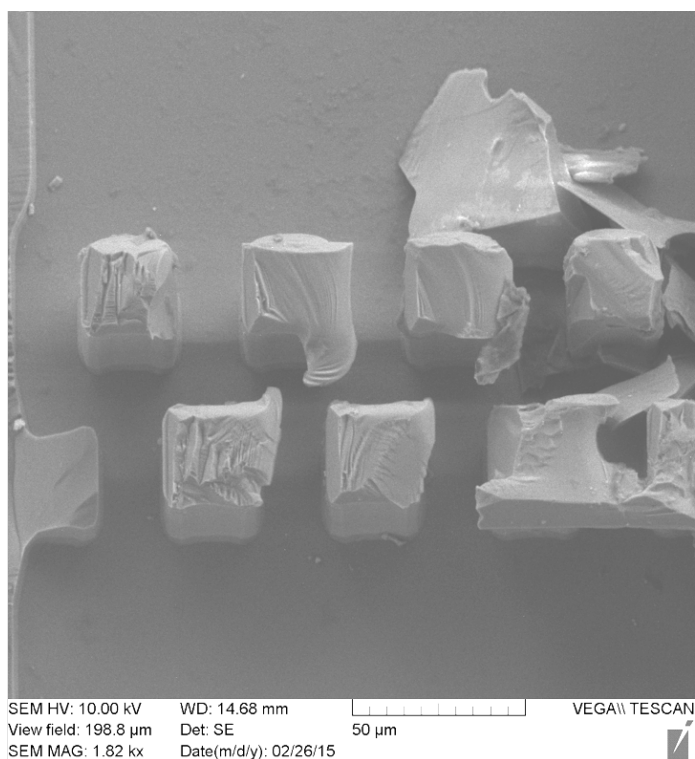


Figure S4 SEM of a broken printhead showing the baffle posts.

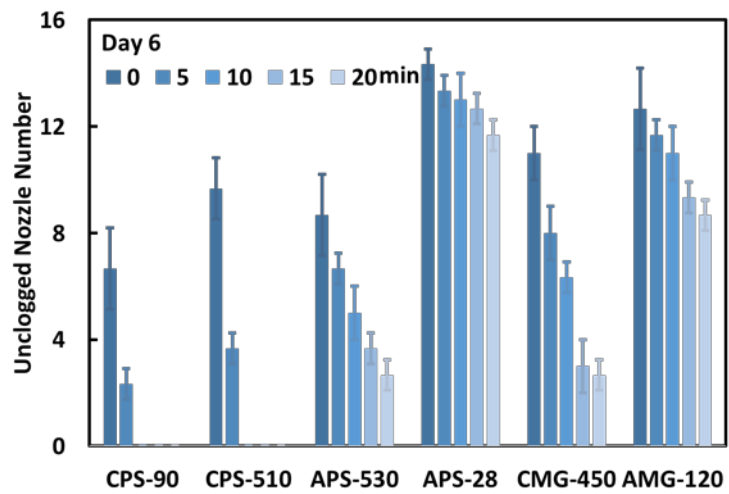


Figure S5 Summary of day 6 nozzle printing results.

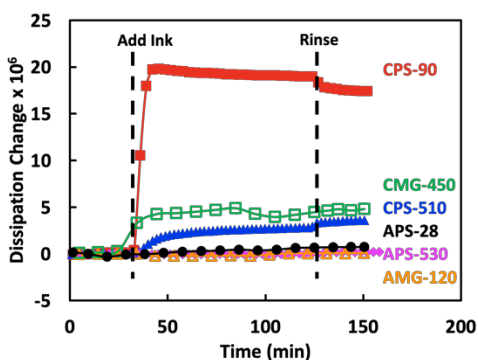
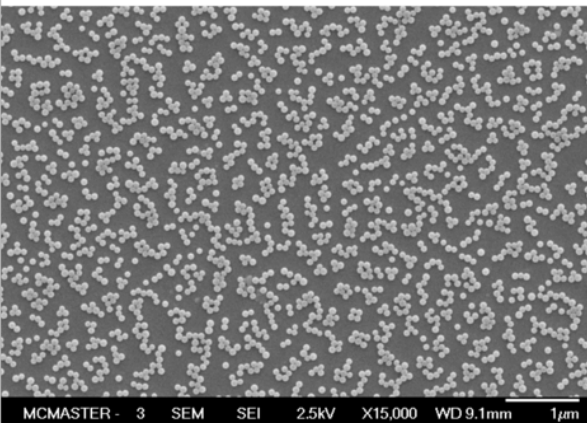


Figure S6 Dissipation results for nanoparticle deposition on QCM-D silica sensors. The dissipation curves were based on the third overtone

Table S1 Validity of the Sauerbrey analysis. The microgels barely obey Reviakine's criteria for the Sauerbrey model ( $(\Delta D / -\Delta f) \ll 4 \times 10^{-7} / \text{Hz}$ )<sup>1</sup> whereas the hard polystyrene particles formed Sauerbrey deposits. These data were based on the third overtone

Name	$\Delta f_3/3$ (Hz)	$\Delta D \times 10^6$	$(\Delta D / -\Delta f_3/3) \times 10^7$ Hz
AMG-120	-3.0	0.7	2.4
CMG-450	-16.7	4.8	2.9
APS-530	-4.5	0.2	0.4
APS-28	-1.9	0.1	0.4
CPS-90	-336.2	17.4	0.5
CPS-510	-93.1	3.6	0.4

**CPS-90 on silica QCM-D sensor**



**CPS-90 on glass slide**

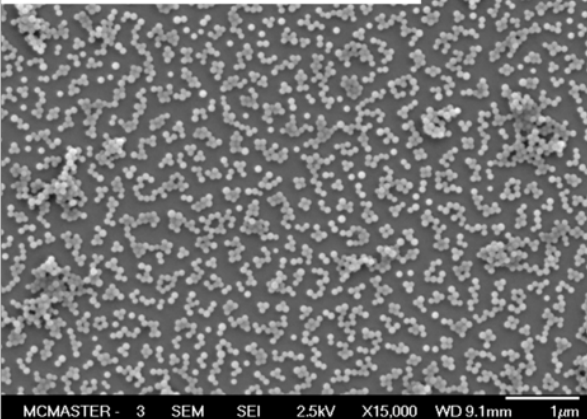


Figure S7 SEMs comparing the deposition of CPS-90 onto the QCM-D silica sensor with deposition on glass

## REFERENCES

- (1) Reviakine, I.; Johannsmann, D.; Richter, R. P. Hearing What You Cannot See and Visualizing What You Hear: Interpreting Quartz Crystal Microbalance Data from Solvated Interfaces. *Anal. Chem.* **2011**, *83*, 8838-8848. <https://doi.org/10.1021/ac201778h>

## Estimating flow rate and Re during Dimatix printing

Measuring mass of printed water+glycerol+surfactant

	Dish weight	Droplet volumn (mg)
	mg	mg
Dish net weight	2679.2	
1	3047.7	368.5
2	3038.8	359.6
3	3060.9	381.7
4	3031.4	352.2
average		365.5
Note	in 5 min, 16 nozzle, 5000x16*300=24000000 droplets	

$$N_d := 5000 \cdot 16 \cdot 300 = 2.4 \cdot 10^7 \quad \rho_{ink} := 1.07 \frac{gm}{mL} \quad pL := 10^{-12} \cdot L$$

$$V_d := 365.5 \frac{mg}{\rho_{ink} \cdot N_d} = 14.233 \text{ pL} \quad \text{Approximate verage drop volume - seems reasonable}$$

### Printing time:

The actual time is the time ejecting the droplet, not the entire process (aspiring and dispensing), so we need the waveform setting. For a segment control, the slew rate means the aspiring time, uptake the solution. So the ejection time for a droplet (or cycle) is

$$t_c := (11.520 - 3.584) \cdot 10^{-6} \text{ s} = (7.936 \cdot 10^{-6}) \text{ s}$$

The droplet ejection frequency

$$f := 5 \text{ kHz}$$

The total time over 5 min that fluid is exiting the nozzle

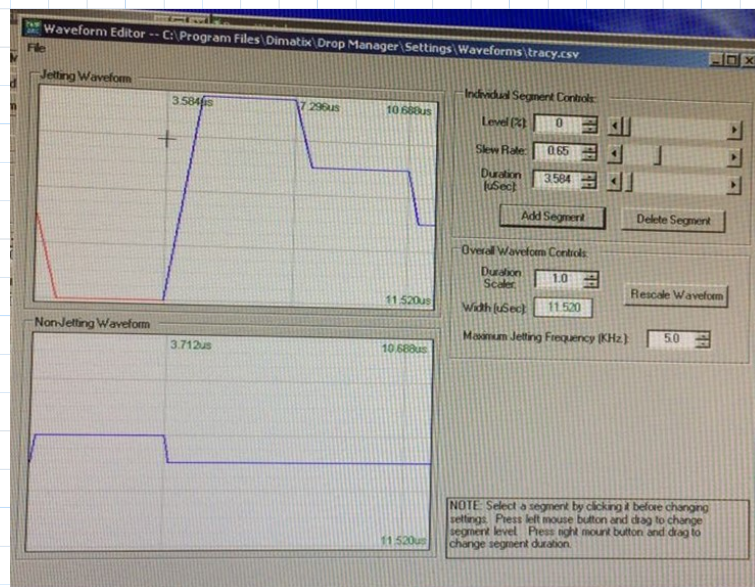
$$t_{total} := 5 \text{ min} \cdot f \cdot t_c = 11.904 \text{ s}$$

$$\frac{1}{f} = (2 \cdot 10^{-4}) \text{ s}$$

Therefore, the total **mass flow rate** for 16 nozzles is

$$Q_{m16} := \frac{365.5 \text{ mg}}{t_{total}} = 1.842 \frac{gm}{min}$$

$$Q_{v16} := \frac{Q_{m16}}{\rho_{ink}} = 1.722 \frac{mL}{min}$$



### Re estimation:

The fluid flow in diamatix printing is through a pyramidal shaped nozzle. This is a simplified estimate of a relevant Reynolds number

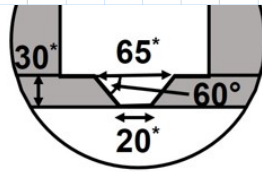
$$L := 20 \mu\text{m} \quad \text{Assumed characteristic linear dimension}$$

$$A_{a16} := 16 \cdot (20 \mu\text{m})^2 = (6.4 \cdot 10^{-5}) \text{ cm}^2 \quad \text{Area of 16 nozzle exits}$$

$$u_{average} := \frac{Q_{v16}}{A_{a16}} = 4.484 \frac{\text{m}}{\text{s}}$$

The dynamic viscosity of the fluid

$$\eta_{ink} := 10 \cdot 10^{-3} \text{ Pa} \cdot \text{s}$$



$$Re := \frac{\rho_{ink} \cdot u_{average} \cdot L}{\eta_{ink}} = 9.595$$

## *Chapter 4*

### **Rapid Screening of Pigments and Binders for Printable Lateral Flow Media**

---

In this chapter, a library of 900 different formulations that contain calcium carbonates or diatomaceous earth pigments with polymer binders was developed. By testing the wicking distance of liquid in these coating media, the calcium carbonate-based pigments with latex binders were concluded as promising printable formulations for their broader wicking distances range.

In Chapter 4, the experiment design, data collection and analysis were mainly conducted by me. Lisa Tran (my summer student) helped me on coating experiments and testing wicking distances. Dr. Robert Pelton and Dr. John Brennan contributed with vital discussion advice in the whole project. I wrote the draft and Dr. Carlos Filipe re-wrote parts of the draft as necessary.

This chapter is being prepared for future publication.

## **Introduction**

Many point-of-use diagnostic assays rely on capillary-driven flow in porous media to move fluid as part of the analyses process. One such example is the pregnancy test, a lateral-flow device where the porous media consists of a porous nitrocellulose membrane driving the wicking of the fluid along the device. For the last ~15 years, filter paper has been extensively used as a platform to create a variety of tests and assays that take advantage of the porous nature of paper to drive the movement of liquids.<sup>1-5</sup> The main advantages of paper are its low cost, availability, compatibility with many biologically-based reactions and the ability to directly print the reagents required to conduct the assays on the paper. There are also disadvantages associated with these two materials: a relatively large volume of liquid (sample and/or reagents) required to drive flow;<sup>6</sup> the variability in terms of performance for filter paper and nitrocellulose;<sup>7</sup> the complexity of design needed to create complex flow patterns,<sup>8-10</sup> which is not compatible to additive manufacturing and potential 3D printing of the entire device. A potential solution to these problems is through the creation of printable porous media that can be deposited as thin films on a variety of surfaces (plastic, glass, etc.) to create lateral flow devices.

The “ink” used to create the printable porous media consists of a pigment and a binder, such as polyvinyl alcohol (PVA) or latex binders. The pigments are micron-size colloidal particles, such as precipitated calcium carbonate (PCC),<sup>11</sup> which are traditionally used in paper coating. Recently, several reports<sup>12-14</sup> have appeared in the literature on the creation of pigment-based thin films using coating techniques in industrial-scale operations. In this paper, we report on a rapid screening method to identify the most promising pigment/binder combinations to generate printable porous media with the goal of ultimately replacing filter paper or nitrocellulose in lateral flow assays.

## **Experimental**

### **Materials**

Fifteen different pigments were tested in this study, consisting of 8 different calcium carbonate and 7 diatomaceous earth (DE). These pigments had a variety of shapes (rhombohedral, spherical, scalenohedral, prismatic and cubic. Figure S4 - 1 (in the supplementary information section) shows electron micrographs of several of the pigments used in this study.

Table 4 - 1.    CaCO<sub>3</sub> and diatomite pigment used in this study.

Pigment	Type	Supplied as:	Form
<b>CaCO<sub>3</sub> from Omya Canada Inc.</b>			
Covercarb 85	GCC <sup>a</sup> 0	Dispersion, 70.5 wt%	Rhombohedral
Hydrocarb 90	GCC1	Dispersion, 76 wt%	Rhombohedral
OmyaJet 5010	MCC <sup>b</sup>	Dispersion, 50 wt%	Spherical
Syncarb S160	PCC <sup>c</sup> 0	Dispersion, 22.5 wt%	Scalenohehdral
<b>CaCO<sub>3</sub> from Specialty Minerals Inc.</b>			
ViCALity Light	PCC1	Powder	Scalenohehdral
ViCALity ALBAFIL	PCC2	Powder	Prismatic
ViCALity Extra Light	PCC3	Powder	Scalenohehdral
ViCALity Heavy	PCC4	Powder	Cubic
<b>Diatomite from Imerys S.A. Inc.</b>			
Celite 221-M	Natural, DEN0	Powder	--
Celpure-C25	Natural, DEN1	Powder	--
ALMDE	Natural, DEN2	Powder	--
LOMDE	Natural, DEN3	Powder	--
Celpure-C100	Calcined <sup>d</sup> , DEC	Powder	--
ALMDE-AW	Acid washed <sup>e</sup> , DEAW0	Powder	--
LOMDE-AW	Acid washed, DEAW1	Powder	--

<sup>a</sup>GCC is ground calcium carbonate.

<sup>b</sup>PCC is precipitated calcium carbonate (PCC) and it is by reacting CO<sub>2</sub> with Ca(OH)<sub>2</sub> reaction.

<sup>c</sup>MCC is modified calcium carbonate consists of 70 % calcium minerals, 20 % calcium silicate, and 10 % amorphous silica.<sup>15</sup>

<sup>d</sup>Calcinated diatomaceous earth is the product of natural diatomaceous earth after a calcination treatment under 1000°C, which results in the melting individual diatomaceous earth into large particles.

<sup>e</sup>For acid washed DE, an acid wash step (sulfuric acid) is used to wash the natural DE before calcination.

Three different binders were tested as parts of the screening process : (1) Acronal S 728 (BASF Canada) is a styrene/n-butyl acrylate copolymer with an average diameter of 200 nm and a glass transition temperature (T<sub>g</sub>) of 23 °C with a solids content of 50 wt%; (2) Styronal BN 4606 X (BASF Canada) is a carboxylated styrene-butadiene copolymer, with an average diameter of 150 nm and a T<sub>g</sub>=6 °C with a solids content of 50 wt%; (3) polyvinyl alcohol (PVA) with a molecular weight of 205 kDa and a degree of hydrolysis 87.7 mol% was purchased from

Sigma (as Mowiol® 40-88). The porous media were deposited on polyester (PE) films (Mohawk Synthetic Premium Polyester film, No. 7 plastic, white, item No. 90-51134, 100 µm thickness) from Mohawk Fine Papers Inc. Both nitrocellulose membranes (Hi-Flow Plus HF075, MilliporeSigma) and Whatman #1 filter paper disks (18.5 cm diameter) were cut with a paper trimmer/cutter (Kutrimmer, Ideal, Germany) into 5 mm wide strips, with lengths of 8 cm.

### **Accelerated Screening Process**

*Ink Preparation.* In this study, a total of 900 different inks were evaluated, which account for all possible combinations of 15 possible pigments (Table 4 - 1) at five contents (3, 6, 9, 12, 15 wt%) with 3 binders at four different dosages (2.5, 5, 7, 10 pph - pph is defined as the mass of binder in the coating formulation divided by the total dry mass of pigment in the formulation). The porous pigments used in the ink formulations were prepared as slurries at 20 wt% in 1 mM NaHCO<sub>3</sub> and pH =8. The latex suspensions used in the ink formulations were prepared by diluting the 50 wt% initial latex suspensions to a final 5 wt% dispersion in 1 mM NaHCO<sub>3</sub> at pH =8. 5 wt% of PVA was prepared by adding solid PVA into 1mM NaHCO<sub>3</sub> solution under mixing and heating at 90° and heating was stopped after the solution was clear, followed by overnight mixing at room temperature. The pH of the final solution was adjusted to pH =8 using 10 mM HCl or NaOH. The ink library was created using a Tecan Freedom Evo 200 liquid handling automated system that dispensed each of the 900 possible formulations on a series of 96 deep well plates (BRADN® polypropylene with a 2.2 mL volume in each well). The total mass of ink in each well was ~1.0-1.5 g, depending on the formulations.

*Coating Porous Media as Parallel Channels.* The inks were coated onto plasma treated (using a Harrick PDC-001, for 45 s at a high RF power (30 W) with a partial air pressure of 700 mTorr) PE films, with a wax defined pattern. The wax pattern was printed with a Xero Phaser 6580 printer with a black wax ink - ColorQube 8570/8580 Black Solid Ink - in “high-quality printing” mode. Figure 4 - 1 shows the process to create the patterns in the PE films. The pattern consisted of eight parallel channels (5.5 cm height, 6 mm width), separated with a 2 mm wax barrier and this pattern was repeated four times in a single page (see Figure S4 - 2 in supplementary information for details, including information regarding the masks used to fabricate the patterned PE films).

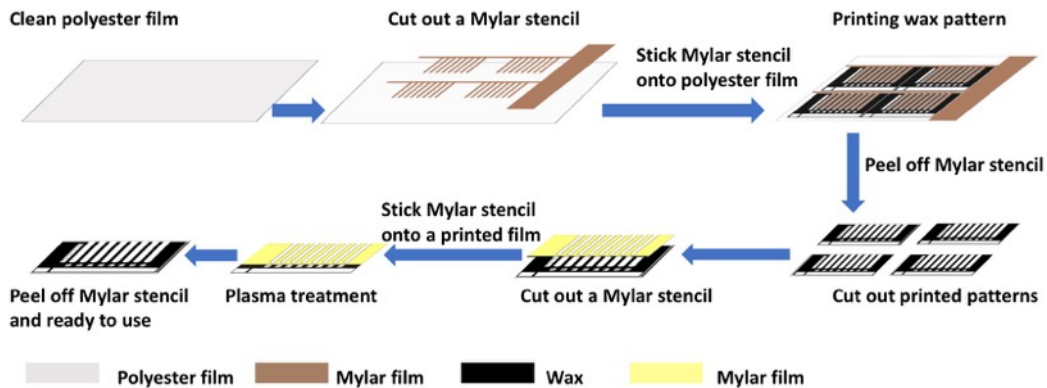


Figure 4 - 1. Sequence of steps to create patterned polyester films for coating the ink library.

A variable speed drawdown coater (EC-200, ChemInstruments Inc.) was used to coat library of inks onto the patterned PE films. Each channel received 50  $\mu\text{L}$  of ink, followed by drawdown with the coater set at the speed of 3.7 m/min (speed = 3) using a #40 size wire wound rod, generating films with 100  $\mu\text{m}$  wet thickness. The inks were allowed to dry overnight at room temperature and 45% RH to generate solid porous coated media.

Wicking Experiments. Vertical wicking measurements were used to characterize the printed porous media. To initiate wicking, the coated PE films supporting the coated porous media were lowered into 1 mM  $\text{NaHCO}_3$  buffer oriented so that the capillary flow was the same direction that the media was originally printed. The wicking was recorded with an iPhone and the wicking distance was extracted after 2 min of starting the wicking experiment.

Figure 4 - 2 provides a general overview of the complete accelerated screening process.

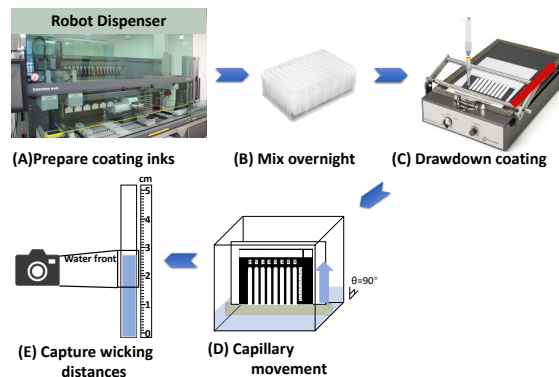


Figure 4 - 2. Overview of the accelerated screen process including the generation of the ink library, coating and assessment of wicking properties.

## Material Characterization

Particle Size Measurements. A Malvern Mastersizer 2000 (running software version V5.1) was used to measure the hydrodynamic diameter of pigments based on the Mie theory. The concentration of the sample was  $\sim 0.01$  wt% in 1 mM NaHCO<sub>3</sub> at pH = 8.0. Three indexes were used to characterize particle size and size distribution: D (0.1) 10% of all the particles in the sample have a diameter smaller than this value. D (0.5) 50% of the particles in the sample are smaller than this value. D (0.9) 90% of the particles in the sample are smaller than this value. These results are based on the volume fraction. Each measurement repeated three times.

Electrophoretic Mobility. The electrophoretic mobility of each pigment was measured using a ZetaPlus analyzer (Brookhaven Instrument Corp., US) using the phase analysis light scattering mode running ten cycles with ten scans for each cycle.

Specific surface area. The specific surface area for each pigment powder was measured through the BET-N<sub>2</sub> method (Autosorb iQ, Quantachrome Instrument, USA), and analyzed by ASiQwin (Version 5.2).

Contact Angle Measurements. Contact angles were measured with a Krüss Drop Shape Analysis System DSA 10 running DSA software (version 1.80.0.2). Sessile drops of 1 mM NaHCO<sub>3</sub> solution were formed with a #26S stainless steel needle, giving a typical volume of 2  $\mu$ L. Contact angles were recorded after 2 min of drop aging time -each experiment was repeated for three times.

SEM Imaging. A dry coated sample was placed on a 45° SEM pin stub a cross-section surface was cut using a razor blade (0.22 mm, VWR), followed by coating with a 5 nm gold layer. These samples were examined using a scanning electron microscope (JEOL 7000F) with a 2.5 keV or 5.0 keV in the secondary electron image. The thickness of the coated layer was measured by ImageJ software (Version 1.51s).

## Results and Discussion

### Characterizing Pigments and Binders

Table 4 - 2 summarizes key characteristics for the 15 pigments used in this study. The electrophoretic mobility of the pigments (dispersed in 1 mM NaHCO<sub>3</sub> and pH =8) shows that all of the DE pigments and most of the CaCO<sub>3</sub> pigments are anionic, except MCC and PCC0 - the only two cationic pigments in this study. The average mass median diameter (D (0.5)) for the DE pigments were in the  $\sim 5$ -35  $\mu$ m range, whereas the CaCO<sub>3</sub> pigments were in the 0.5-10  $\mu$ m range. The DE pigments had substantially

broader particle distributions when compared to CaCO<sub>3</sub> pigments, which can be an issue when attempting to create very uniform porous media. The specific surface area (SSA) of the CaCO<sub>3</sub> pigments were mainly in the 3 to 13m<sup>2</sup>/g range (with MCC being an exception), while the DE pigments had substantially larger SSA, in the 10 to 44 m<sup>2</sup>/g range.

Table 4 - 2. Properties of porous pigments dispersed in 1 mM NaHCO<sub>3</sub> at pH = 8.0 solution. The standard derivations reported are for three repeated measurements. The results of particle size were based on the volume concentration.

<b>Pigment</b>	<b>Electrophoretic Mobility (10<sup>-8</sup> m<sup>2</sup>/ (V·s))</b>	<b>Specific Surface Area (m<sup>2</sup>/g)</b>	<b>D (0.1) (µm)</b>	<b>D (0.5) (µm)</b>	<b>D (0.9) (µm)</b>
<b>Calcium Carbonate-based</b>					
GCC0	-3.5±0.04	12.5 <sup>a</sup>	0.2	0.7	1.5
GCC1	-2.5±0.1	12.5 <sup>a</sup>	0.7	1.3	2.3
MCC	1.1±0.1	30.0 <sup>a</sup>	1.0	2.0	6.7
PCC0	0.3±0.05	9.0 <sup>a</sup>	1.8	4.5	9.8
PCC1	-3.0±0.3	7.8 <sup>a</sup>	2.4	5.2	9.9
PCC2	-1.8±0.4	7.0 <sup>a</sup>	2.2	4.9	9.6
PCC3	-1.7±0.2	8.5 <sup>a</sup>	2.1	4.5	8.4
PCC4	-3.9±0.2	3.3 <sup>a</sup>	1.8	5.7	12.4
<b>Diatomaceous Earth-based</b>					
DEN0	-3.2±0.04	44.2	5.8	16.6	44.3
DEN1	-4.4±0.06	11.7	3.2	13.3	42.1
DEN2	-3.2±0.1	25.4	1.7	10.1	20.3
DEN3	-4.4±0.08	24.5	1.0	4.9	17.4
DEC	-3.9±0.05	14.4	4.0	13.6	45.9
DEAW0	-2.1±0.07	35.6	10.0	35.5	79.0
DEAW1	-3.5±0.11	36.3	1.5	8.1	32.8

<sup>a</sup> Values reported by supplier.

The main properties for the two latex binders (dispersed in 1 mM NaHCO<sub>3</sub> and pH =8) used in this study are shown in Table 4 - 3. The particle diameter for both binders is about ten times smaller than the size of the pigments listed in Table 4 - 2. PVA is a non-ionic water-soluble polymer, hence particle diameters are not applicable for this binder.

Table 4 - 3. Properties for the two latex binders used in this study. Samples were dispersed in a 1 mM NaHCO<sub>3</sub> solution at pH =8. The standard derivation was calculated from three repeated measurements.

Binder	Electrophoretic Mobility ( $10^{-8} \text{ m}^2/(\text{V}\cdot\text{s})$ )	Diameter (nm)	Tg (°C)
Acronal S 728 (Latex1)	-3.6±0.12	200	23 <sup>a</sup>
Styronal BN 4606 X (Latex2)	-3.3±0.08	150	6 <sup>a</sup>

<sup>a</sup> Values reported by supplier.

When a pigment is combined with a binder, the particle size and the distribution associated with the mixture changed to varying degrees, compared to the size and distribution associated with pigment and binder on their own. Table 4 - 4 shows this using the pigment PCC1 as an example. The addition of PVA or Latex1 (10 pph) resulted in no difference on the particle size and distribution of the pigment on its own, indicating that pigment aggregation did not occur. On the other hand, the addition of 10 pph Latex2 resulted in a substantial increase in particle size and a broadening of the size distribution for the mixture, indicating aggregation of the pigments. The library of 900 inks generated in this study will contain formulations where pigment aggregation occurs upon mixing the pigment with the binder and before coating takes place.

Table 4 - 4. The particle size and size distribution associated with PCC1 (15 wt%) in the absence or in the presence of 10 pph binder (PVA, Latex1, or Latex2). All final mixtures were in 1 mM NaHCO<sub>3</sub> and pH = 8.0.

Pigment	Binder	Binder Dosage (pph)	D (0.1) ( $\mu\text{m}$ )	D (0.5) ( $\mu\text{m}$ )	D (0.9) ( $\mu\text{m}$ )
PCC1			2.4	5.3	9.9
PCC1	PVA	10	2.3	5.4	11.0
PCC1	Latex1	10	2.3	5.0	9.5
PCC1	Latex2	10	7.0	24.8	55.2

### Coating and the Importance of Plasma Treatment

The ink library was deposited on plasma treated PE films with wax barriers defining the region onto each ink was placed, followed by spreading using a drawdown coater with a wire-wound rod (see schematic shown in Figure S4 - 3). Each region (exposed PE film surrounded by wax barriers) received 50  $\mu\text{L}$  of ink. Plasma treatment of the PE film was needed to ensure good wettability and spreading of the inks. Figure 4 - 3 shows the PE surface after coating with an ink containing 12 wt% of PCC0 and 10 pph of Latex2 in 1 mM NaHCO<sub>3</sub>. Prior to plasma treatment, the water contact angle of the PE film was  $\sim 54^\circ$  resulting in poor wettability and non-uniform coating. After a 45 s plasma treatment, the water contact angle decreased to  $\sim 25^\circ$  and a uniform coating could be obtained. It is important to note that the wax barriers needed to be masked during the plasma treatment step to

preserve the ability of the barrier to contain the ink during the coating process (Figure S4 - 4 in supplementary information).

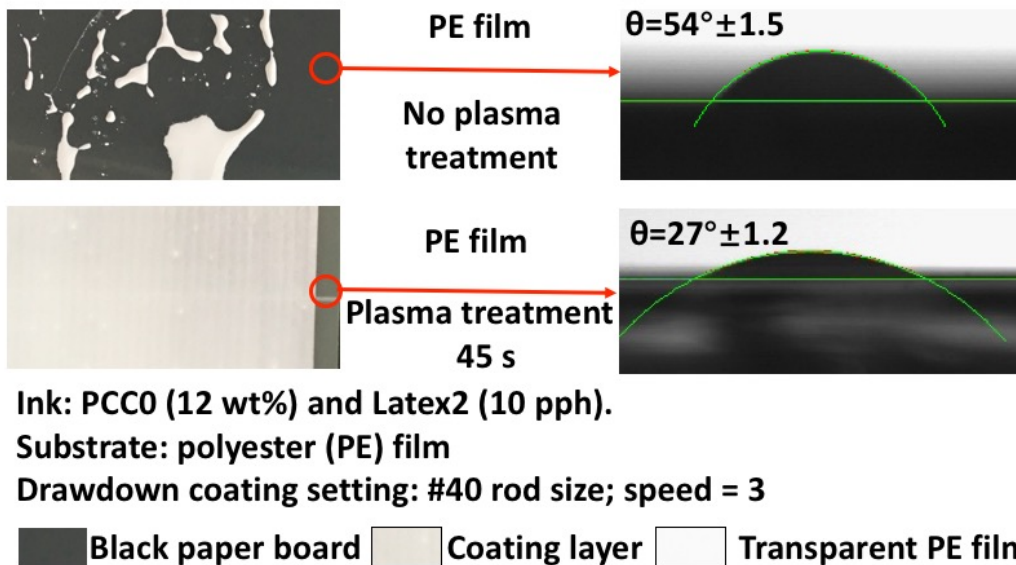
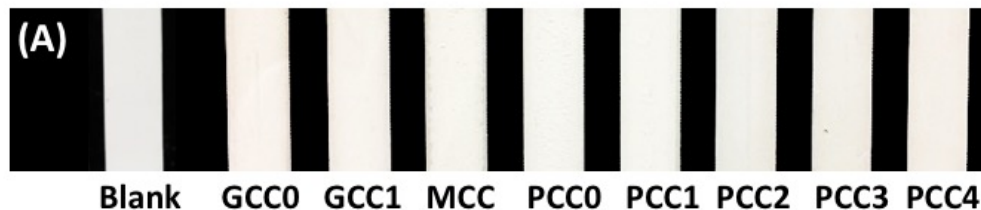
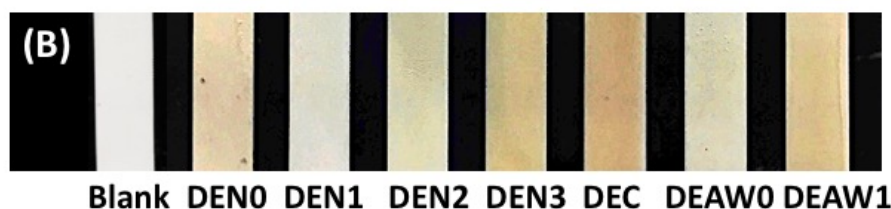


Figure 4 - 3. Images obtained after drawdown coating of an ink containing PCC0 as the pigment and Latex2 as the binder on a PE film with or without plasma surface treatment.

Figure 4 - 4 shows images of the porous media (dried ink) for the two types of pigments used in this study ( $\text{CaCO}_3$  and diatomite-based). The coating layers were highly uniform and perfectly contained within the wax barriers. Due to larger particle size and broader size distribution, DE coatings were coarser than the  $\text{CaCO}_3$  based coatings.  $\text{CaCO}_3$  is white while the diatomite-based pigments have different colors, depending on its components of silica, ferric oxide, and alumina. The natural color of DE pigments might be a source of interference when performing colorimetric assays on the media.

**CaCO<sub>3</sub> coatings****Diatomite coatings**

Ink: 15 wt% of pigment and 5 pph of Latex2 in 1 mM NaHCO<sub>3</sub>, pH =8.0.

Drawdown coating parameters: #40 rod size, speed = 3.

Figure 4 - 4. Images of porous media (dried coating layers) on plasma treated PE films (black regions are wax). Panel (A) is for CaCO<sub>3</sub> based coatings. Panel (B) is for DE-based coatings.

**Wicking Kinetics for the Coated Ink Library**

We evaluated a total of 900 different inks, which account for all possible combinations of 15 possible pigments (Table 4 - 1) at five different contents (3, 6, 9, 12, 15 wt%), with 3 binders at four different dosages (2.5, 5, 7, 10 pph). Wicking experiments were performed to characterize the various porous media in the library. These experiments were done by partially immersing the PE films, each containing 8 channels coated with 8 different ink formulations and measuring the wicking distance of 1 mM NaHCO<sub>3</sub> solution after two minutes have passed. Since we did not observe any differences when either inks of 3%, 6% and 9% pigment contents were used (Figure S4 - 5 for CaCO<sub>3</sub> and Figure S4 - 6 for diatomite -based pigments. Reason is explained later in this paper), we only compared the results among formulations of 3%, 12% and 15% of pigment. The results obtained from the library are presented as supplementary information that Figure S4 - 7 and Figure S4 - 8 contain the results for 360 different formulations. Figure 4 - 5 shows the results for the wicking distance (at 2 minutes) for formulations obtained using two pigments PCC1 and DEN1. We selected these two pigments to be included in Figure 4 - 5 since they exhibited a wide range of wicking speed as a function of formulation and because the wicking speeds were amongst the highest obtained in the library.

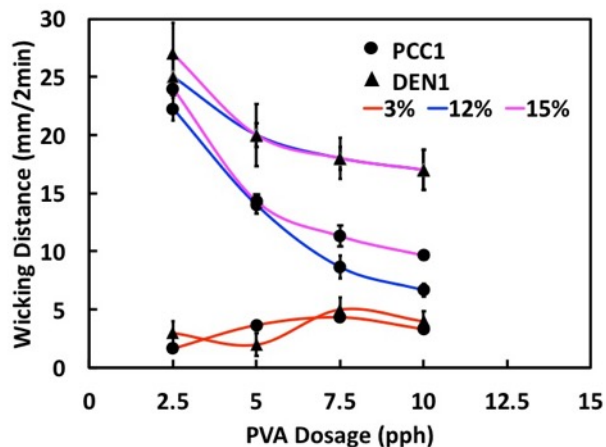


Figure 4 - 5. The wicking distances of 1 mM  $\text{NaHCO}_3$  solution in 2 min within PCC1 and DEN1 based coatings, addition of PVA binder.

When pigment content was low (3 wt%), the wicking distance was very short for these two pigments and that distance did not depend on the dosage of binder used. The reason for this is that the amount of pigment was so small that the coverage of the PE film was essentially in the form a discontinuous monolayer as shown in the SEM pictures in Figure 4 - 6 (Latex2 was the binder used to generate those films). Higher pigment contents resulted in a substantial increase in the wicking speed and Figure 4 - 6 shows that the porous media formed consisted of uniform and continuous 10-15  $\mu\text{m}$  thick films. Figure 4 - 5 also shows that as the binder dosage increases, the wicking distance decreases, potentially due to PVA swelling in solution and blocking pores.<sup>16</sup> A similar decrease in the wicking distance with increasing of the PVA dosage was observed for all pigments when present in contents equal to or great than 12% (see Figure S4 - 7 and Figure S4 - 8).

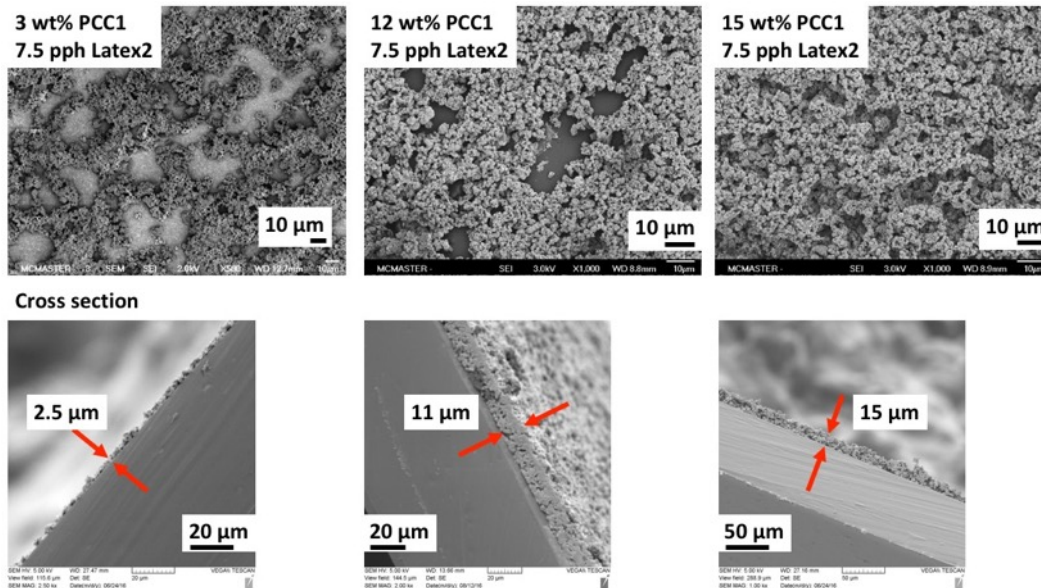


Figure 4 - 6. SEM images of the surface and cross sections for media coated with inks of PCC1 at 3 wt%, 12 wt% and 15 wt% with 7.5 Latex2 as the binder.

For the latex binders used in this study (Latex 1 and Latex2), the effect of dosage on the wicking distance was not as large as was the case with PVA. Figure 4 - 7 shows that increasing the dosage of the latex binders does result in a decrease of the wicking distance, but that decrease is substantially smaller than that observed for PVA, suggesting a lower extent of pore blocking for the latex binders. Above 5 pph dosage of latex binders, the wicking distance is essentially independent of the dosage for the binder. This is a very useful feature when there is the need to produce porous media with very high levels of reproducibility and uniformity (i.e. small deviations in applied dosage will result in little or no difference in performance).

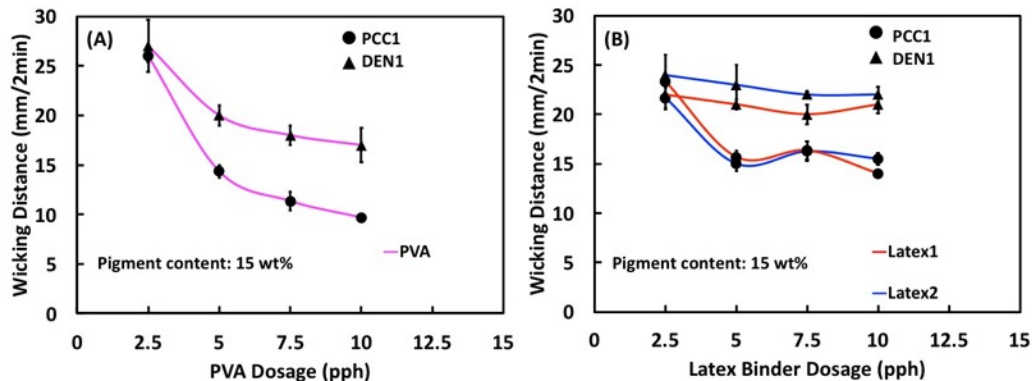


Figure 4 - 7. Comparing the effect of the binder dosage on the wicking distance (after 2 minutes) for PVA (A) and two latex binders (B) when using two different pigments – PCC1 and DEN1.

The properties of the pigment particles dominate the wicking behaviors. Table 4 - 5 classified pigments into four groups. The detailed wicking characteristic also depend upon the binder type and pigments solids contents. Based on these results, we choose four pigments (PCC1, PCC2, PCC3, and PCC4) for detailed assessment as pigments for printable porous media – see Chapter 5.

Table 4 - 5.    A summary of the wicking distances in 1 mM NaHCO<sub>3</sub>.

<b>Description</b>	<b>Porous pigment</b>	<b>Form</b>	<b>Wicking distance of buffer in 2 min(mm)</b>
Slow	GCC0	Rhombohedral	0-10
	GCC1	Rhombohedral	
	MCC	Spherical	
Medium	PCC2	Prismatic	10-20
	PCC4	Cubic	
	DEN3	--	
	DEAW1	--	
	DEN0	--	
	DEAW0	--	
Fast	PCC0	Scaleno-hedral	20-35
	PCC1	Scaleno-hedral	
	PCC3	Scaleno-hedral	
	DEC		
	DEN1		
	DEN2		
	Whatman #1 filter paper		
Ultrafast	Nitrocellulose membrane		>35

## **Conclusion**

We developed a simple and effective method to generate and test a library of 900 different formulations to create printable porous media. The focus is on the future use as printable porous media to support lateral flow assays, substituting filter paper and nitrocellulose. The library consisted of combinations of 15 different pigments and 3 different binders at various concentrations and it was created using an

automated liquid handler. The formulations were coated as a series of 8 parallel channels on PE films and parallel wicking experiments were conducted to rapidly identify formulation that resulted in low, medium and high wicking rates. It was found that the pigment content needs to be equal or greater than 12 wt% to generate a continuous uniform coating and produce reasonable wicking rates. Scalenohedral precipitated CaCO<sub>3</sub> pigments were superior to ground calcium carbonates and DE pigments as they led to larger wicking distances, with the ability to tune the wicking distance through changes in formulation. Latex binders are preferred to generate printable media as compared to PVA, since the wicking distance is highly sensitive to the dosage of PVA, whereas that dependence is much lower for latex binders. This means that latex binders will result in more repeatable and uniform printable porous media product.

## Supporting Information

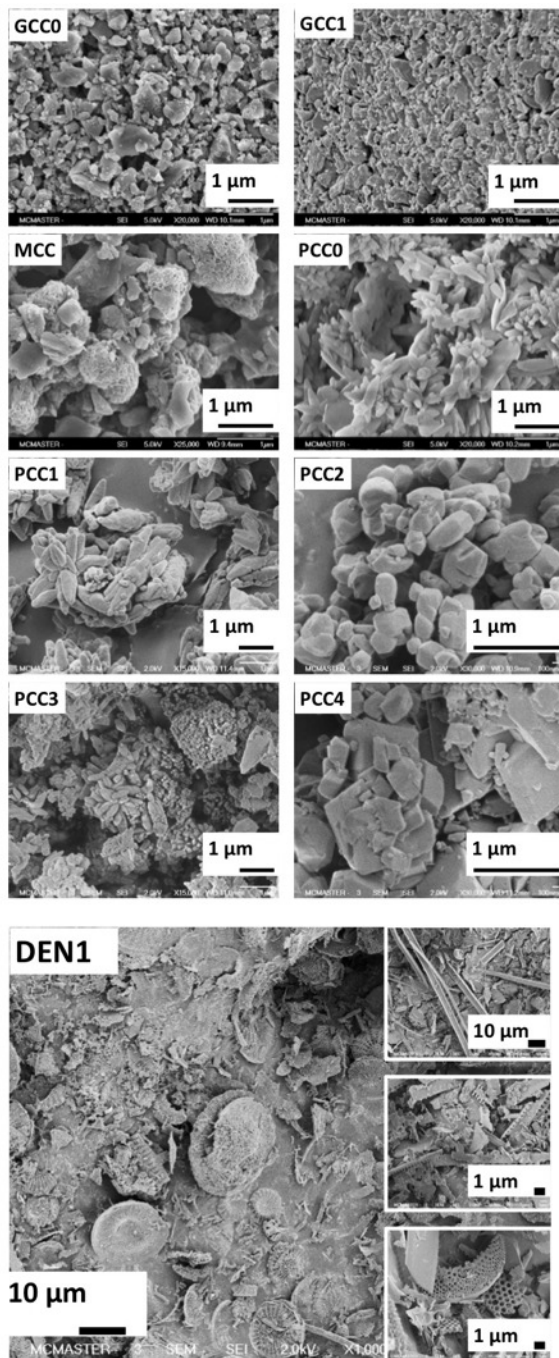


Figure S4 - 1. SEM images for the eight CaCO<sub>3</sub> pigments used in this study and DEN1 as an example of DE pigments. Only one DE pigment is shown because all seven had similar structures.

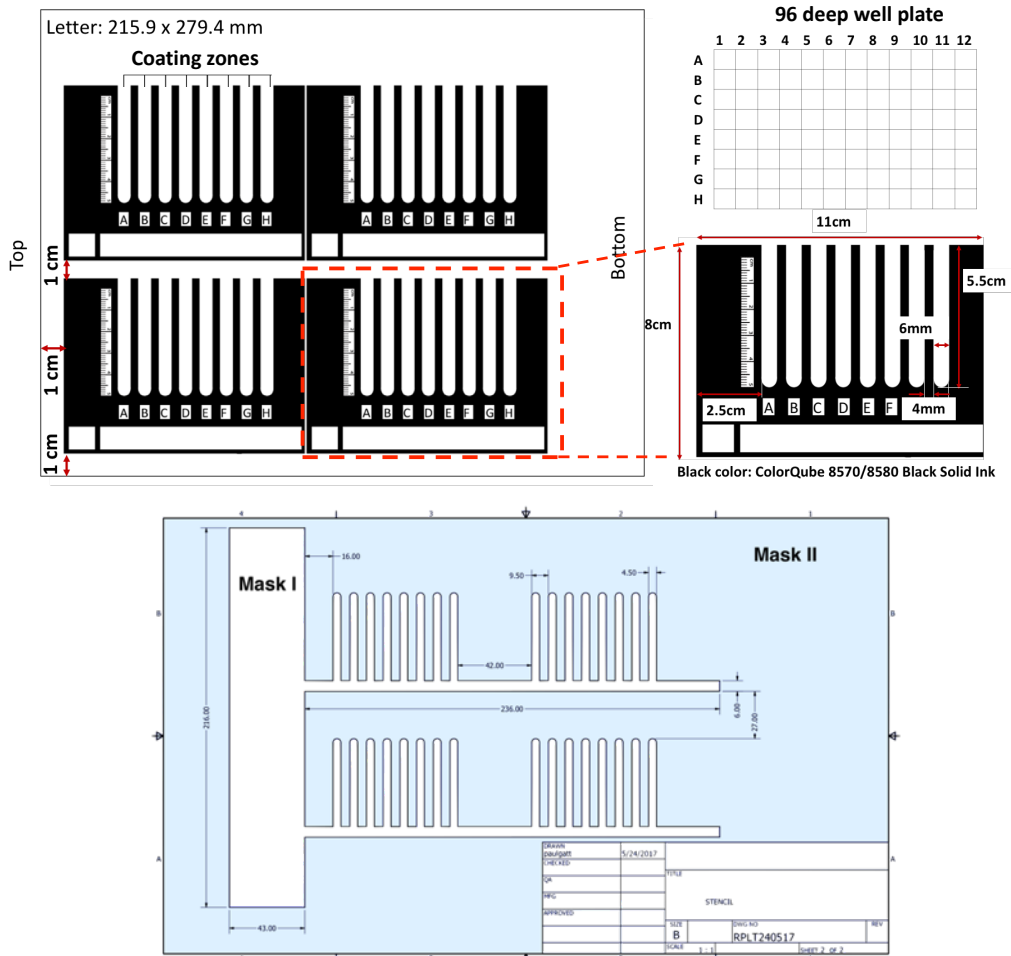


Figure S4 - 2. The design of parallel coating channels, and masks I, II.

**Masks design:** The masks were made from Mylar film (polyethylene terephthalate, transparent, 50  $\mu\text{m}$  thickness, Tekra, USA), they were designed using AutoCAD (2018) and cut by a laser cutter (Speedy 300, Trotec Laser, Canada). To avoid the presence containments on non-printed zones during the wax printing process, a Mylar film mask (Mask I) was attached onto the polyester film using a double-sided tape. After the wax printing step, Mask I was removed. A patterned PE film was cut into four repeating patterns using a paper trimmer (Kutrimmer, Ideal, Germany). Mask II covered the wax printed areas, leaving the parallel coating channels on the PE film, exposed to receive plasma treatment (PDC-001, Harrick, Ithaca, NY) for 45 s at high RF power (30 W) with a partial air pressure of 700 mTorr).

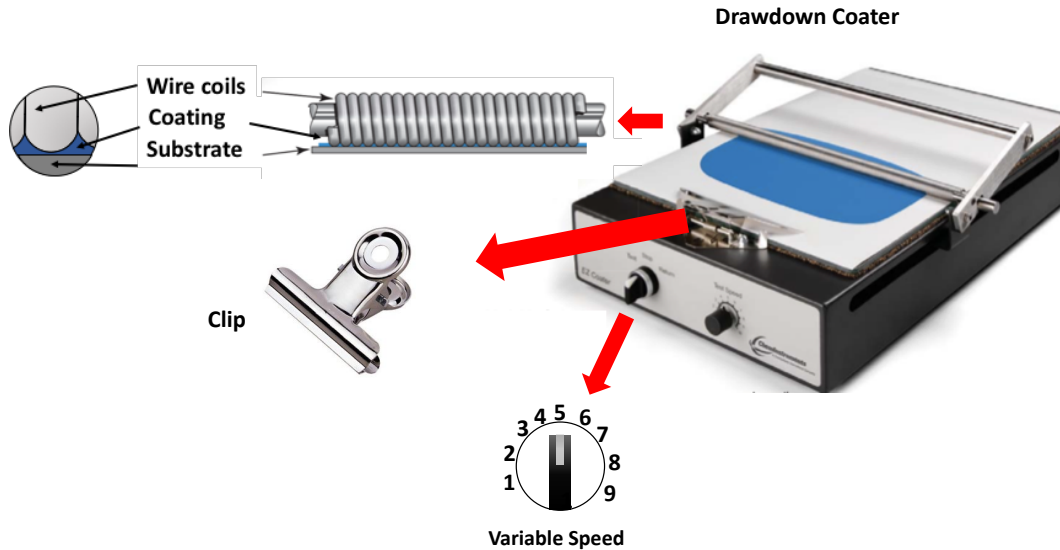


Figure S4 - 3. The diagram for a variable speed drawdown coater. This figure is modified of the images of the EC-200, ChemInstruments Inc.

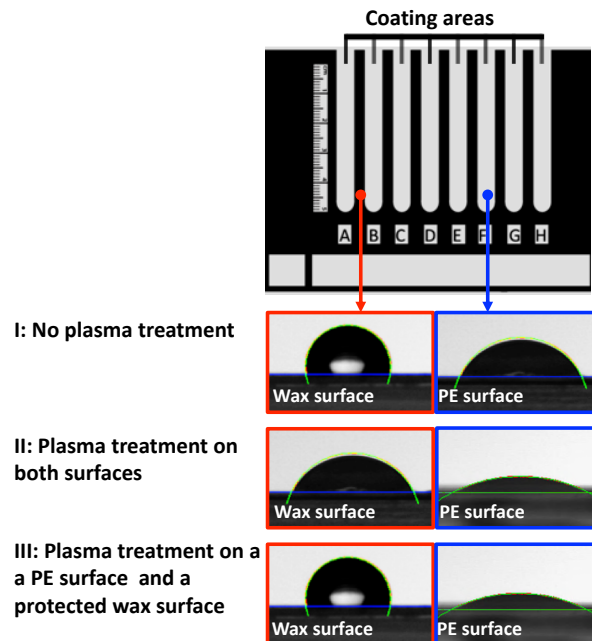


Figure S4 - 4. Water contact angle of a wax delineated channel in a PE film for three different surface treatment: (I) Wax printed channel and PE original surface before plasma treatment; (II) The same as in (I) but after exposing both the wax and PE surface to plasma treatment; (III) The same as in II but using a Mylar mask to cover the wax patterns before exposing the film to plasma treatment, thereby protecting and maintaining the integrity of the wax barrier .

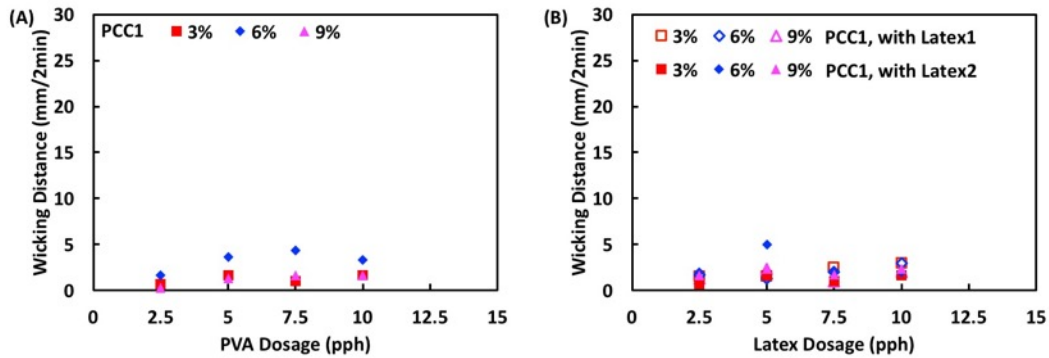


Figure S4 - 5. Wicking distances of 1 mM NaHCO<sub>3</sub> solution within 2 min in PCC1 based coating media. (A) Inks: 3, 6, 9 wt% of PCC1 with 2.5, 5, 7.5 and 10 pph of PVA binders. (B) Inks: 3, 6, 9 wt% of PCC1 with 2.5, 5, 7.5 and 10 pph of latex binders.

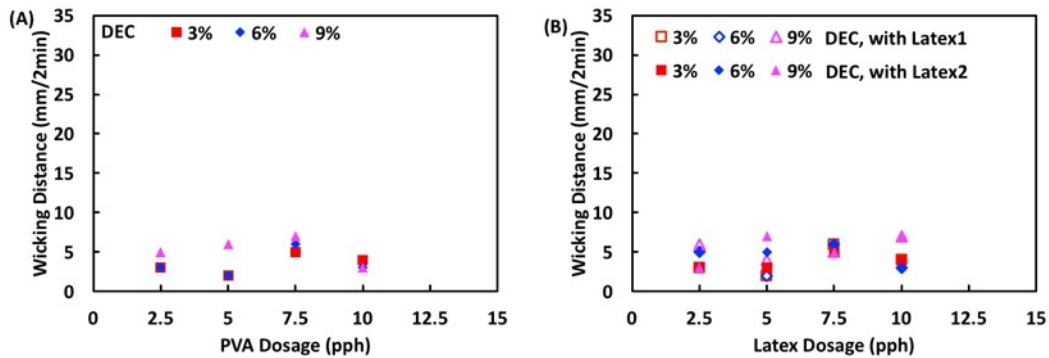


Figure S4 - 6. Wicking distances of 1 mM NaHCO<sub>3</sub> solution within 2 min in DEC based coating media. (A) Inks: 3, 6, 9 wt% of DEC with 2.5, 5, 7.5 and 10 pph of PVA binders. (B) Inks: 3, 6, 9 wt% of DEC with 2.5, 5, 7.5 and 10 pph of latex binders.

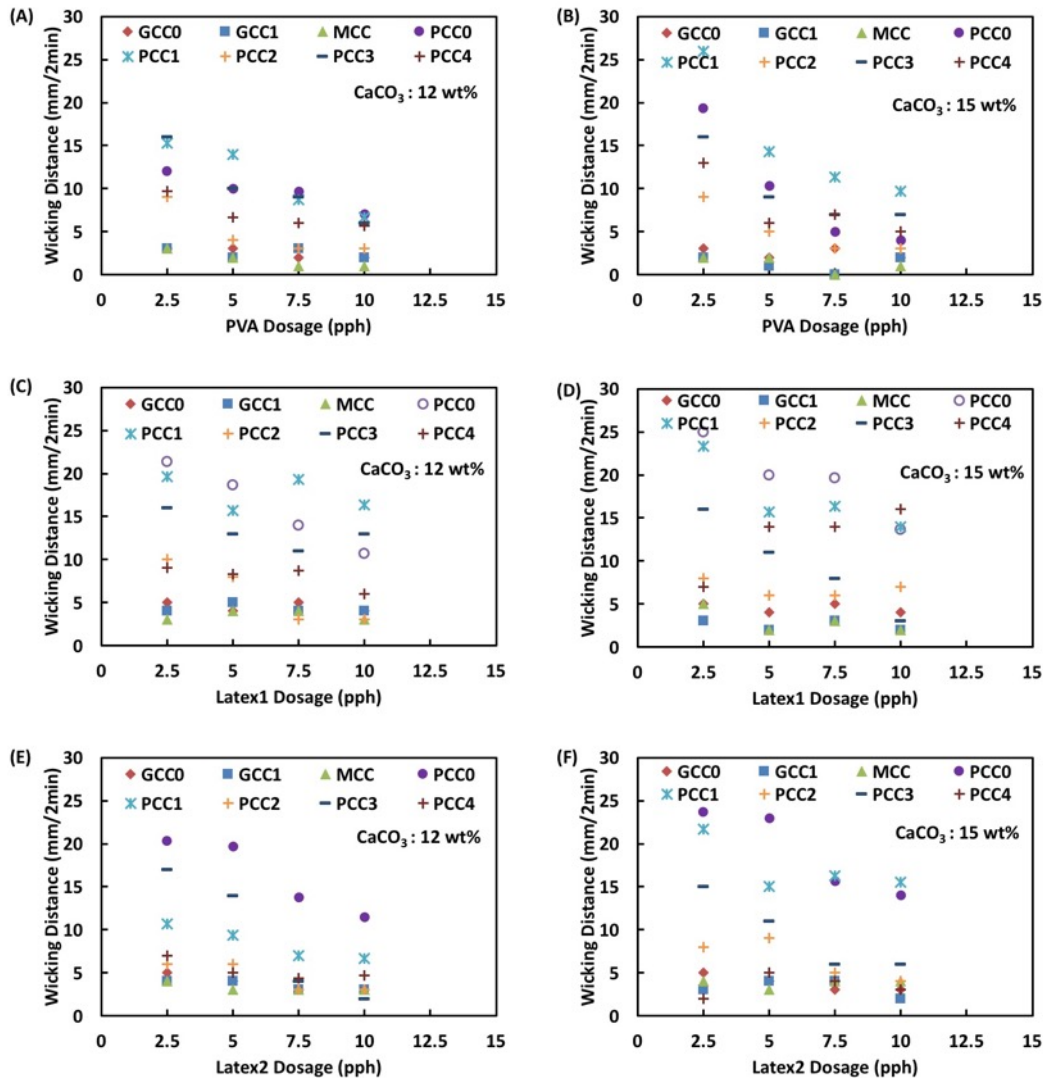


Figure S4 - 7. Wicking distances of 1 mM NaHCO<sub>3</sub> solution within 2 min in 8 calcium carbonate-based coating media. (A, C, E) Inks contains 12 wt% of calcium carbonate-based with 2.5, 5, 7.5 and 10 pph of three binders respectively. (B, D, F) Inks contains 15 wt% of calcium carbonate-based with 2.5, 5, 7.5 and 10 pph of three binders respectively.

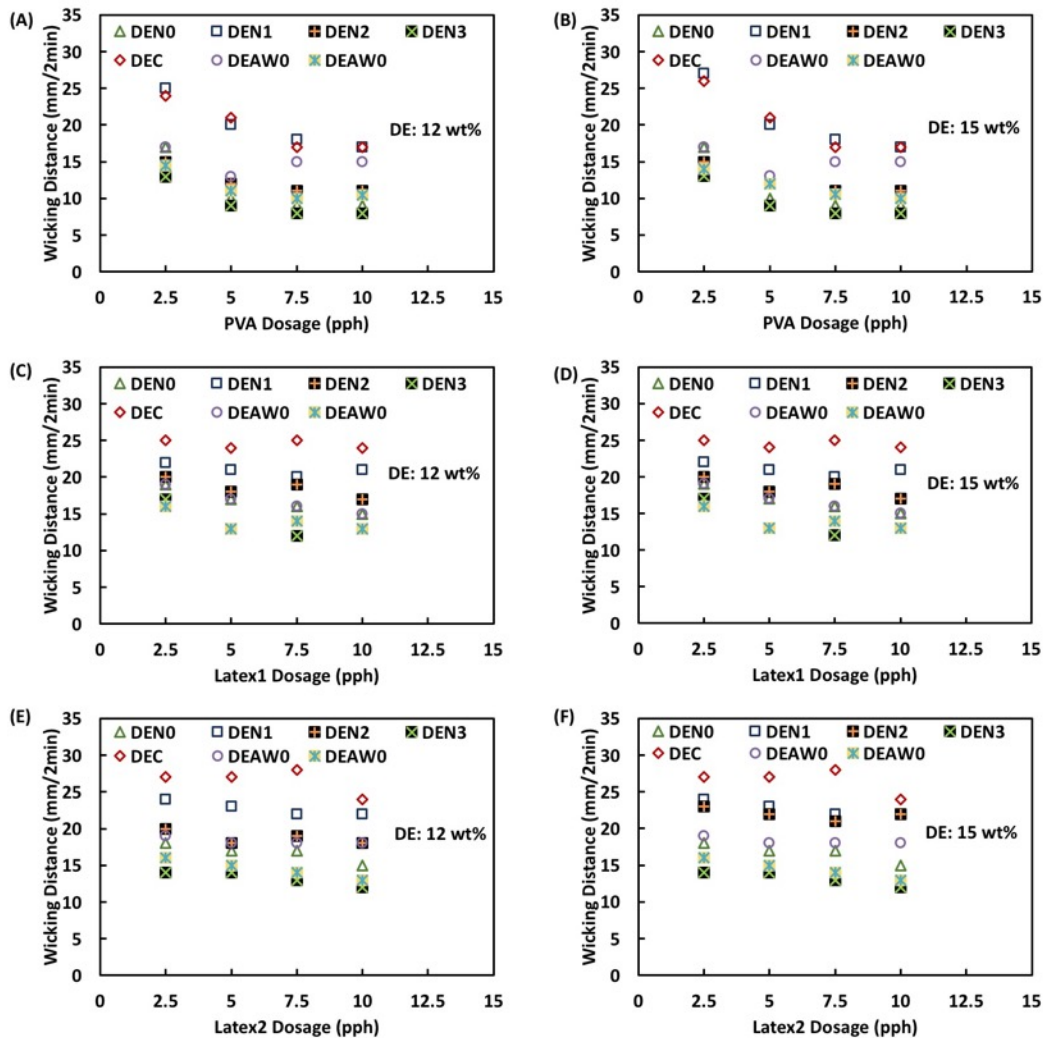


Figure S4 - 8. Wicking distances of 1 mM  $\text{NaHCO}_3$  solution within 2 min in 7 DE-based coating media. (A, C, E) Inks contains 12 wt% of DE-based with 2.5, 5, 7.5 and 10 pph of three binders respectively. (B, D, F) Inks contains 15 wt% of DE-based with 2.5, 5, 7.5 and 10 pph of three binders respectively.

## Acknowledgement

The authors thank Chris Butcher (Canadian Center for Electron Microscopy, McMaster University) and Marcia Reid (McMaster Health Sciences) for sample preparation and training. The authors thanks Dr. Charles de Lannoy for offering access to the BET- $\text{N}_2$  instrument (Chemical Engineering Department, McMaster University). The authors also thank the Natural Sciences and Engineering Research Council of Canada for funding through the *SENTINEL* Bioactive Paper Network. We also thank the Canadian Foundation for Innovation and the Ontario Ministry of Research and Innovation for Infrastructure funding to the Biointerfaces Institute.

YL acknowledges funding from the China Scholarship Council (CSC). JDB holds the Canada Research Chair in Bioanalytical Chemistry and Biointerfaces. RP holds the Canada Research Chair in Interfacial Technologies.

## References

- (1) Pelton, R. Bioactive paper provides a low-cost platform for diagnostics. *TrAC Trends in Analytical Chemistry* **2009**, *28*, 925-942.
- (2) Yager, P.; Domingo, G. J.; Gerdes, J. Point-of-Care Diagnostics for Global Health. *Annual Review of Biomedical Engineering* **2008**, *10*, 107-144.
- (3) Cate, D. M.; Adkins, J. A.; Mettakoonpitak, J.; Henry, C. S. Recent Developments in Paper-Based Microfluidic Devices. *Analytical Chemistry* **2015**, *87*, 19-41.
- (4) Yamada, K.; Shibata, H.; Suzuki, K.; Citterio, D. Toward practical application of paper-based microfluidics for medical diagnostics: state-of-the-art and challenges. *Lab on a Chip* **2017**, *17*, 1206-1249.
- (5) Martinez, A. W.; Phillips, S. T.; Butte, M. J.; Whitesides, G. M. Patterned paper as a platform for inexpensive, low-volume, portable bioassays. *Angewandte Chemie (International ed. in English)* **2007**, *46*, 1318-1320.
- (6) Millipore. Rapid Lateral Flow Test Strips Considerations for Product Development. *In Lit. No. TB500EN00EM Rev. C 12/13* **2013**.
- (7) Niskanen, K.; Yhdistys, S. P.-I.; Press, T.; Oy, F.: *Paper physics*; Fapet Oy, 1998.
- (8) Jahanshahi-Anbuhi, S.; Henry, A.; Leung, V.; Sicard, C.; Pennings, K.; Pelton, R.; Brennan, J. D.; Filipe, C. D. M. Paper-based microfluidics with an erodible polymeric bridge giving controlled release and timed flow shutoff. *Lab on a Chip* **2014**, *14*, 229-236.
- (9) Martinez, A. W.; Phillips, S. T.; Whitesides, G. M. Three-dimensional microfluidic devices fabricated in layered paper and tape. *Proceedings of the National Academy of Sciences* **2008**, *105*, 19606-19611.
- (10) Fu, E.; Ramsey, S. A.; Kauffman, P.; Lutz, B.; Yager, P. Transport in two-dimensional paper networks. *Microfluidics and nanofluidics* **2011**, *10*, 29-35.
- (11) Fardim, P. Paper and Surface Chemistry—Part 2-Coating and Printability. **2002**.
- (12) Jutila, E.; Koivunen, R.; Bollström, R.; Gane, P. Wicking and chromatographic properties of highly porous functionalised calcium carbonate coatings custom-designed for microfluidic devices. *Journal of Micromechanics and Microengineering* **2019**, *29*, 055004.
- (13) Jutila, E.; Koivunen, R.; Kiiski, I.; Bollström, R.; Sikanen, T.; Gane, P. Microfluidic Lateral Flow Cytochrome P450 Assay on a Novel Printed Functionalized Calcium Carbonate-Based Platform for Rapid Screening of Human Xenobiotic Metabolism. *Advanced Functional Materials* **2018**, *28*, 1802793.
- (14) Koivunen, R.; Jutila, E.; Bollström, R.; Gane, P. Hydrophobic patterning of functional porous pigment coatings by inkjet printing. *Microfluidics and Nanofluidics* **2016**, *20*, 83.
- (15) Shin, J. Y. The Recent Development of New Pigment Binders. **2016**.

(16) Lamminmaki, T. T.; Kettle, J. P.; Puukko, P. J. T.; Gane, P. A. C. Absorption Capability and Inkjet Ink Colorant Penetration into Binders Commonly Used in Pigmented Paper Coatings. *Ind Eng Chem Res* **2011**, *50*, 3287-3294.

## *Chapter 5*

### **Printable Porous Substrates for Lateral Flow Media**

---

In this chapter, printable porous media were developed for lateral flow strips. With inks of calcium carbonate pigments and latex binders, the media were directly printed into different patterns. Furthermore, the porous media provide different wicking velocity profiles, depending on the inks. To the best of our knowledge this work is the first document about printable porous medium targeting use in lateral flow devices.

The experiment designs and data collection were conducted by me with the assistance with my summer student Lisa Tran. I analyzed the data and wrote the draft. Dr. Robert Pelton, Dr. Carlos Filipe and Dr. John Brennan contributed with vital discussion. Dr. Robert Pelton also helped me re-write the draft as necessary.

This chapter has been submitted to *Industrial & Engineering Chemistry Research*.

## **Printed Thin Films with Controlled Porosity as Lateral Flow Media**

Yuanhua Li,<sup>a</sup> Lisa Tran,<sup>a</sup> Carlos D.M. Filipe,<sup>a</sup> John D. Brennan,<sup>b</sup> and Robert H. Pelton<sup>a\*</sup>

<sup>a</sup>Department of Chemical Engineering, <sup>b</sup>Biointerfaces Institute, McMaster University, Hamilton, Ontario, L8S 4L7, Canada

\*peltonrh@mcmaster.ca

Keywords: lateral flow devices, printing, porous media, precipitated calcium carbonate, latex binder

### **Abstract**

Traditional materials for lateral flow devices (cellulose, nitrocellulose) are typically produced in large batches with relatively thick membranes and a uniform pore size, making it challenging to develop devices with variable flow rates. With a view to the development of easily manufactured lateral flow media with variable porosity and flow rates, we investigated the ability to produce a fully printed porous media based on colloidal, precipitated calcium carbonate (PCC) dispersions containing latex binders. PCC dispersions with varying particle sizes were printed onto glass surfaces and it was observed that flow rates could be controlled by varying particle size. Based on this finding, a device with three zones, having distinctly different porosities and wicking behaviors, was printed with three calcium carbonate inks in a single printing operation. The printed media were ~10% the thickness of paper or nitrocellulose membranes, with lower porosities and wicking rates. We demonstrate that such PCC materials can adsorb enzymes such as alkaline phosphatase (ALP) with retention of activity, and show that a colorimetric ALP reaction giving a colored precipitate generated strong color signals on the printed PCC lateral flow media.

### **Introduction**

Laboratories around the world have focused on the development of inexpensive biosensors for point-of-care diagnostics.<sup>1, 2</sup> Many of these efforts involve lateral flow devices that use capillary-driven wicking to move fluid flow along a porous media strip, facilitating sequential reaction steps. Typically, a colored output gives either a yes/no result or a semi-quantitative output when coupled to a cellphone camera or other color sensor. Most commercial lateral flow devices (LFDs) employ porous nitrocellulose (NC)<sup>3, 4</sup> as the wicking membrane, whereas many academic publications use filter or chromatography paper (FP).<sup>2, 5, 6</sup>

Unfortunately, neither paper nor nitrocellulose are ideal media for lateral flow devices. For example, the high porosity and thickness of NC and FP media (for example, Whatman #1 is 180  $\mu\text{m}$  thick with a pore volume fraction of 0.7) requires a high volume of aqueous phase ( $\sim 130 \text{ mL/m}^2$ ), which can be costly with expensive reagents. The inherent opacity of FP and NC membranes also causes the color signal at the bottom of a membrane to be greatly attenuated compared to color originating near the viewing surface, with much of the measurable signal originating only from the top 10 micrometers.<sup>7</sup> In addition, the coarse nature of cellulose fibers or cotton linters ultimately limits uniformity of paper-based media.<sup>8</sup> Finally, FP and NC media generally have a single porosity and thus it is not possible to produce complex and multiplexed sensors which may require regions with both slow and fast wicking rate pathways,<sup>9</sup> hydrophobic regions,<sup>10-14</sup> or z-stacked 3-dimensional formats,<sup>15</sup> meaning that fabrication of more complex sensors involves many steps, some of which defy automation.

In this paper we explore an approach to fabricating lateral flow membranes based on printable porous media. The potential advantages include: the generation of complex sensor shapes without hydrophobic barriers; the ability to vary the media porosity along the length of a sensor; and, the possible manufacture of an “all-printed biosensor” in a continuous manufacturing line. To identify a suitable material for printing, we looked to paper coating technologies, as the highest quality printing substrates are coated papers, where ink penetration and spreading are controlled by the coating properties. Importantly, paper coating pigments and associated polymeric binders are readily available and can be tuned to give a wide range of porous media properties. In preliminary work to be reported elsewhere, we employed a novel accelerated screening procedure to evaluate over nine hundred ink formulations as potential lateral flow media. From that work we identified a family of precipitated calcium carbonate (PCC) pigments that showed the most promise.

A recent series of papers from Aalto University demonstrates the potential of pigment coated films as substrates for lateral flow biosensors. Their approach is to employ conventional coating operations to produce uniform coatings on substrates. These materials could ultimately offer advantages over conventional nitrocellulose or paper, distributed in rolls or sheets.<sup>16, 17</sup> In a very recent publication, they show that pigment-based media could give bimodal pore sized distribution that offers fast wicking and high surface areas.<sup>18</sup> Herein, we build upon the Aalto work by demonstrating that PCC-based media can be printed directly to give thin films with complex porous media shapes, with position dependent wicking characteristics in a single printing/drying step. Slow-speed and high-speed wicking zones can be printed in a single operation without hydrophobic barriers or other templates.

## Experimental

**Materials.** Four types of precipitated calcium carbonate (PCC) were provided as dry powders by Minerals Technologies. The latex binder, Acronal S 728 (BASF Canada) was a styrene/n-butyl acrylate copolymer with an average diameter of 200 nm and a glass transition temperature of 23 °C with a solids content of 50 wt%. Millipore HF18002 Nitrocellulose (NC) and Whatman #1 filter paper disks (18.5 cm diameter) were cut with a paper trimmer/cutter (Kutrimmer, Ideal, Germany) into 5 mm wide strips, with lengths of 8 cm.

Alkaline phosphatase (ALP) from bovine intestinal mucosa, *p*-nitrophenyl phosphate, disodium salt (pNPP), BCIP/NBT solution, (0.56 mM BCIP (5-bromo-4-chloro-3-indolyl hydrogen phosphate), 0.48 mM NBT (nitro-blue tetrazolium chloride), 59.3 mM MgCl<sub>2</sub> in 10 mM Tris HCl, pH ~9.2), diethanolamine (>99.5%), magnesium chloride hexahydrate and hydrochloric acid (37%) were purchased from Sigma Aldrich.

**PCC Particle Size Distribution.** The particle size distributions of the four PCC samples were measured with a Coulter Mastersizer 2000 (software version V5.1). 15 wt% PCC suspensions in 1 mM NaHCO<sub>3</sub> were dispersed with a vortex mixer. The PCC dispersions were slowly added to 100 mL of 1 mM NaHCO<sub>3</sub> until the signal of light obscuration reached to 15%. The concentration of the dilute sample was ~0.01 wt%.

**PCC Inks.** A typical ink dispersion was prepared by adding 2.25 g of dry PCC to 12.41 g of 1 mM NaHCO<sub>3</sub> solution in a 20 mL glass vial, followed by 0.34 g of wet (50 wt%) latex binder dispersion. The resulting mixture was stirred with a vortex mixer at speed 1 overnight. The wet mass fractions were 15% PCC and 1.1% polymeric binder. The resulting dry media consisted of 93 wt% PCC, and 7% polymeric binder.

Ink viscosities were measured with a Vibro Viscometer (SV-10, 30 Hz, A&D Company). Before measurement, the ink was mixed for 10 min on a vortex mixer at a speed setting of 7. Measurements were made with 10 mL of the ink dispersion at 23 °C, over a period of 1 minute. Experiments were performed in triplicate.

Ink surface tensions were measured by the pendant drop method with a Krüss Drop Shape Analysis System DSA 10 running DSA software (version 1.80.0.2). Drops were formed with a No.18 stainless steel needle (diameter 1.2 mm). Measurements were recorded after 2 min of drop aging time.

**Printing Porous Media.** The PCC-binder media were printed on glass microscope slide coverslips (VWR, Borosilicate glass, 24 x 60 mm, thickness 0.13-0.17 mm). The coverslips were first cleaned by a 5 min exposure to UV/Ozone (ProCleaner™ Bioforce Nanosciences, Inc.). The PCC inks were then printed with a XYZ3060

Dispense Platform (BioDot Inc.) – see photographs in Figure S1 in the supporting information. With this printer, the coverslips were supported on a moving platform. The inks were extruded through the dispensing tube with a disposable plastic tip (#15, OD = 1.8 mm) positioned 0.05 mm above the coverslip. In the printing process, the ink was ejected at a rate of 2  $\mu\text{L/s}$  and the coverslip is moved past the dispensing tip (1 cm/s), giving a line of wet ink about 2 mm wide and 20  $\mu\text{m}$  thick (see below). In the simplest case, printing resulted in a single strip of medium, parallel to the long axis of the coverslip. The printed strip started 5 mm from one end of the coverslip. Wider printed strips were produced by printing parallel lines of ink. After printing, the media strips were allowed to dry at room temperature ( $23 \pm 1$  °C) for at least an hour.

***Cross-sectional Profiles.*** The average thicknesses of the printed media were measured from images taken with an inverted microscope (Primo Vert, Carl Zeiss Microscopy, LLC) with a monochromatic camera. The media and glass coverslip support were cut with a diamond pen (VWR) and mounted for direct viewing. The cross-sectional profiles of the printed and dried PCC media were measured with a KLA Tencor D-100 stylus profilometer using AlphaStep D-100 Stylus Profiler software (Version 2.1.0.4) with a scan length was 3.5 mm and stylus load of 5 mg.

***Wicking Experiments.*** Vertical wicking measurements were used to characterize the printed porous media. 5.5 mL of 1 mM  $\text{NaHCO}_3$  solution was added to a cylindrical Drosophila vial (transparent polystyrene, 28.5 x 95 mm, VWR, 734-2265) giving a liquid depth of 8 mm. A graticule with 1 mm line spacing printed on polyester film, was fixed to the exterior surface of the cylinder to facilitate measuring the height of the wicking front. To initiate wicking, the coverslip supporting the printed PCC media was lowered into the  $\text{NaHCO}_3$  buffer oriented so that the capillary flow was the same direction that the media was originally printed. The vials were not sealed. The wicking was recorded with an iPhone and the wicking distance was extracted as a function of time from the video. In the case of wicking experiments with FP and NC, the strips were fixed to coverslips with Scotch Permanent Double-Sided Tape (3M 34-8518-7934-5) and tested as above.

***Alkaline Phosphatase (ALP) Solutions.*** An ALP enzyme stock solution of 500  $\mu\text{g/mL}$  was prepared by adding 5 mg of dry ALP powder to 10 mL of DEA buffer (1.0 M diethanolamine with 0.5 mM  $\text{MgCl}_2$ , pH 9.8) in a 15 mL Falcon tube. Further ALP dilutions were made with DEA buffer.

***PCC-bound ALP.*** 143 mg of dry PCC powder was added to 1.5 mL of the ALP solution in a 2 mL microcentrifuge tube and the suspension was mixed overnight on a microplate shaker at speed 3. The PCC-bound ALP was separated from free ALP by centrifugation with an Allegra 25R Centrifuge (Beckman Coulter Inc.) at 4000 rpm for 15 mins. The supernatants were isolated and saved for ALP analysis. The ALP treated PCC was redispersed in 1.5 mL of DEA buffer followed by

centrifugation at 4000 rpm for 15 min. The washing procedure was repeated a total of three times. The resulting PCC particles with adsorbed ALP were dispersed in 1.5 mL of DEA buffer and stored at 4 °C.

The ALP reaction with *p*-nitrophenol phosphate was used to: 1) estimate the amount of ALP bound to the PCC particles; 2) estimate the activity of PCC-bound ALP compared to the parent ALP solution. The chemical structures for the assay are shown in Figure S2 and a schematic summary of the assay in Figure S3. The two types of analysis are now described.

The quantity of ALP bound to the PCC was determined by measuring the residual ALP activity in the first supernatant from the washing procedure. 15 µL of the 1<sup>st</sup> supernatant was pipetted into a Nunc™ 384-well clear polystyrene plate (Catalog number, 242765, 120 µL well, sterile, Thermo Scientific Inc.), followed by adding 60 µL of 0.27 M pNPP premixed solution. The resulting sample was incubated for 5 min at 25 °C, then stopped by adding 25 µL of 3 M NaOH solution. The absorbance at 405 nm of the 100 µL solution was determined with an Infinite M1000 microplate reader (Tecan Trading AG, Switzerland). The fraction of active enzyme adsorbed onto PCC was based on three measurements:  $A_s$  the absorbance of the supernatant,  $A_c$  the absorbance of a control ALP solution not exposed to PCC and  $A_o$ , the background absorbance of an ALP-free solution (15 µL of DEA buffer, 60 µL of pNPP and 25 µL of 3 M NaOH). The fraction of active ALP adsorbed onto PCC was calculated with the following equation where the sample volumes for all measurement types were equal (100 µL):

$$f_a = (A_c - A_s)/(A_c - A_o). \quad \text{Eq. 1}$$

The activity of PCC-bound ALP, relative to an ALP solution was estimated as follows. Washed PCC (see above) with adsorbed ALP was added to 1.5 mL of DEA buffer, followed by mixing for 10 min on a vortex mixer with speed setting of 6. 15 µL of the mixture was transferred into a 384-well plate, followed by 60 µL of pNPP solution which was incubated for 5 min at 25 °C. The reaction was stopped by adding 3 M NaOH. The resulting mixture was centrifuged at 4000 rpm for 15 mins. 80 µL of the supernatant was transferred to a clean well for absorbance measurements. The relative activity of the PCC-bound ALP was calculated from the following equation where:  $A_{pcc}$  is the absorbance generated by PCC-bound ALP;  $A_o$  is the blank;  $A_c$  is the absorbance of 15 µL of the ALP solution;  $f_a$  is the fraction of ALP adsorbed onto PCC (Eq. 1); and the total sample volume of each absorbance solution was 80 µL.

$$R_{alp} = \frac{A_{pcc} - A_o}{f_a(A_c - A_o)} \quad \text{Eq. 2}$$

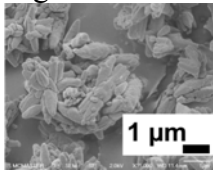
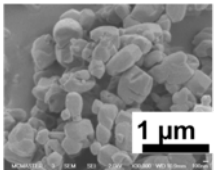
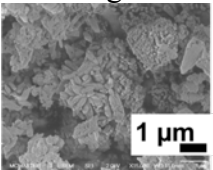
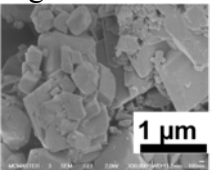
***ALP Catalyzed Color Generation on PCC Media.*** The ALP catalyzed conversion of yellow, soluble NBT to NBTF, a purple precipitate, was performed on 2 mm wide printed PCC1 media strips, as well as on 5 mm wide FP and NC strips. For more details of the color forming reaction see Figure S4. ALP solution (20  $\mu\text{g}/\text{mL}$ ) was printed as a strip across the three FP, NC, and PCC1 media with the BioDot dispenser at a rate of 0.2  $\mu\text{L}$  per mm at a position 10 mm beyond the beginning of the media strips. The PCC3-bound ALP dispersion (19  $\mu\text{g}/\text{mL}$  of adsorbed ALP and 95  $\text{mg}/\text{mL}$  of PCC3) was printed also at 0.2  $\mu\text{L}$  per mm. The coverage (mass/projected area) of ALP was approximately the same for the three media types, however, the filter paper and NC strips had more ALP because the strips were wider than the PCC1 strips.

5.5 mL of BCIP/NBT solution (see above) was added to a 65 mL cylindrical Drosophila vial (transparent polystyrene, 28.5 x 95 mm, VWR, 734-2265). The ALP spotted media was placed in the BCIP/NBT solution and left for two hours allowing the wicking solution to move past the ALP zone, to the end of test strips.

## Results

**PCC Ink Properties.** The inks consisted of three components, 15 wt% PCC, 1.1 wt% latex binder and 1 mM NaHCO<sub>3</sub> aqueous phase, giving a dry composition of 93% wt% PCC and 7 wt% latex binder. Four PCC types were employed to obtain a range of properties. SEM images, specific surfaces area and particle size measurements of PCC particles used in this work are shown in Table 1. The mean agglomerate sizes were similar and the particle size distributions were broad for each of the four PCC types. The specific surfaces areas ranged from 3 to 9 m<sup>2</sup>/g, reflecting the variation in the shapes of the particles.

Table 1 Some properties of the precipitated calcium carbonate (PCC).

	PCC1	PCC2	PCC3	PCC4
Product Name	ViCALity Light	ViCALity ALBAFIL	ViCALity Extra Light	ViCALity Light
SEM				
Shape*	Scalenohedral	Prismatic	Scalenohedral	Cubic
SSA (m <sup>2</sup> /g)*	7.8	7	8.5	3.3
Diameter (µm)**	10%:2.3, 50%:5.2, 90%:9.9	10%:2.2, 50%:4.9, 90%:9.6	10%:2.1, 50%:4.5, 90%:8.4	10%:1.8, 50%:5.7, 90%:12

\* information provided by supplier. \*\* percentile values from particle size distribution.

The surface tension and viscosity values for the liquid inks are summarized in Table S1. The surface tensions ranged between 42 and 47 mN/m, suggesting the presence of some surface-active agents presumably from the latex binder. The viscosities were about 10 times higher than that of water, and in the range typically required for printing with the BioDot printer.

**Printing of PCC Media.** Media printing was performed with a BioDot XYZ3060. Figure 1 shows a drawing of the printing process and a photograph of a PCC ink being printed onto a clean glass coverslip. The translation stage, supporting the coverslip, moves as ink is extruded from the dispensing tube tip. Additional photographs of a printed PCC2 strip and a cross-section of PCC1, both after drying, are shown in Figure S5.

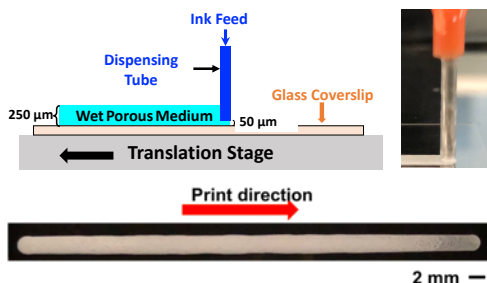


Figure 1 Schematic and a photograph of media dispersion being printed on a glass coverslip using the BioDot XYZ3060. The photograph along the bottom shows a dry strip of PCC1 media on glass sitting on a black background.

The quality of the printed media was sensitive to the PCC concentration in the ink. Above PCC contents of 15 wt%, the cross-sectional profiles developed lobes along the edges and the buffer wicking fronts were not uniform – see Figure S6. Glass was chosen for the supporting surface because it gave good adhesion to the PCC/latex composite without excessive spreading. The glass was non-porous and thus did not support independent capillary flow, and was rigid and uniform, a requirement for the BioDot printer.

**Media Characterization.** Vertical wicking experiments with buffer and dodecane were used to characterize the porous media. The vertical wicking behaviors of the three PCC inks are compared with Whatman No. 1 filter paper (FP) and Millipore HF18002 Nitrocellulose (NC) in Figure 2. Note PCC3 results were not plotted as they superimposed on the PCC1 data. The NC gave the fastest wicking, followed by the filter paper. The wicking rate for PCC1 was a little slower than the filter paper, whereas PCC2 and PCC4 based media gave much lower wicking rates. Thus, the wicking kinetics can be controlled by varying the type of PCC.

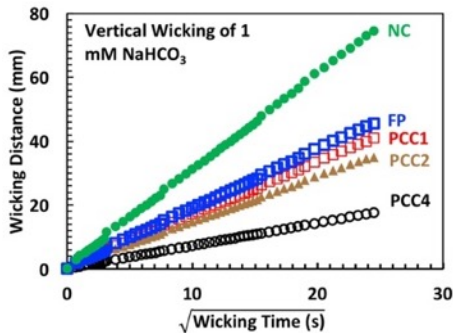


Figure 2. Vertical wicking behaviors of three printed PCC media, Whatman No. 1 filter paper (FP) and a commercial nitrocellulose membrane (NC).

The experimental wicking heights were linear functions of the square root of wicking time, a relationship predicted by the Washburn equation for wicking in capillaries.<sup>19</sup> The slopes of the time<sup>1/2</sup> plots, which we call “Washburn slopes ( $S_w$ )” serve as a measure of wicking rates. Eq. 3 gives the expression for the Washburn slopes which are functions of the surface tension of the wicking fluid,  $\gamma$ , the capillary radius,  $r$ , the contact angle,  $\theta$ , and the viscosity of the wicking fluid,  $\eta$ . The slopes of the experimental curves in Figure 2, as well as PCC3, are tabulated in Table 2.

$$S_w = \sqrt{\frac{\gamma \cdot r \cdot \cos \theta}{2 \cdot \eta}} \quad \text{Eq. 3}$$

Table 2 Properties of PCC-based media compared to filter paper and a nitrocellulose.\*.

Porous Medium	Basis Weight (g/m <sup>2</sup> )	Thickness (μm)	Void Fraction	Average Pore Diameter (nm)	Water Contact Angle (deg)	Reagent Capacity (mL/m <sup>2</sup> )	Washburn Slope, $S_w$ $\frac{dh}{d\sqrt{t}}$ ( $\frac{mm}{\sqrt{s}}$ )
PCC1	43.8	23	0.214	670	79	4.92	1.69
PCC2	41	18	0.060	640	81	1.07	1.46
PCC3	41.3	20	0.148	460	75	2.95	1.66
PCC4	34.7	15	0.045	170	82	0.67	0.72
FP	87	180	0.705	-	22 <sup>20</sup>	127	1.89
NC	56*	134 <sup>21</sup>	0.7 <sup>7</sup>	-	68 <sup>22</sup> 50 <sup>23</sup>	93	3.08

\* PCC media includes 7 wt% latex binder. FP is Whatman No.1 filter paper and NC is HF18002 Nitrocellulose. “Basis Weight” is the dry mass per projected surface

area covered by the coating or paper sheet. “Reagent Capacity” is the total pore volume per projected surface area. The Washburn Slopes,  $S_w$ , were extracted from buffer wicking results in Figure 2.

\*\* based on the thickness, the void fraction and assuming the nitrocellulose density was 1.4 g/mL.

Dodecane wicking experiments were also performed with PCC media (see Figure S7 in the supporting information). Because dodecane is a low surface energy fluid, we assumed the contact angle on calcium carbonate was zero and Eq. 3 was used to calculate the equivalent capillary diameter which represents an average pore diameter. The results, summarized in Table 2, show the average pore diameters varied from 170 nm to 670 nm for the PCC media. The pore diameters from dodecane experiments and the water wicking rates were used to calculate the corresponding water contact angles on the PCC media, using Eq. 3. The results in Table 2 showed contact angles varying over the narrow range of 75-82°. These water contact angles on PCC media are much higher than published values for cellulose but are only a little greater than nitrocellulose – see Table 2.

Other properties of the four PCC media are compared to filter paper and nitrocellulose in Table 2. The “Basis Weight” is a paper technology term and is defined as the dry mass per projected surface area covered by the coating or paper sheet. The “Reagent Capacity” is pore volume per projected surface area. The NC and FP media were ten times thicker than our printed PCC-based media. Thick media is not necessarily an advantage as most visible colored products are in the first 10  $\mu\text{m}$  (see page 9 in reference <sup>7</sup>).

The void fractions of the FP and NC substrates were also substantially greater than those obtained with the PCC media. Taken together the high thickness and void volumes of the NC and FP media result in very high reagent capacities (i.e. the total pore volume per projected surface area) compared to the PCC media. For situations with limited sample volumes or expensive reagents, high reagent capacities are not desired.

Wicking experiments are also good indicators of reproducibility. Triplicate wicking experiments for PCC1, FP, and NC were performed and the results are shown in Figure S8. The slopes,  $\text{mm}/(\text{time}^{1/2})$ , for the curves are PCC1 (1.81, 1.56, and 1.51), FP (1.74, 1.92, and 1.83), and NC (2.97, 2.98, 2.95). The NC media showed the least variation in slopes, with FP and PCC1 showing more variability.

One of the most promising aspects of printed media is the ability to print devices with both high and low permeability zones in a single printing operation. Figure 3 shows a photograph of the three-zone device during a buffer wicking experiment. Also shown are the corresponding wicking heights as a function of the square root of the wicking time. Each media type gave linear segments, which is consistent with

the Washburn equation for laminar flow in capillary tubes.<sup>19,24</sup> However, slopes of the three linear segments do not correspond to the values in Table 2, which were determined with 2 mm wide strips of constant composition. The first zone in contact with the reservoir was PCC1, and the Washburn slope for the first linear segment in Figure 3 was  $2.48 \text{ mm/s}^{0.5}$ , much higher than  $1.69 \text{ mm/s}^{0.5}$  in Table 2, and close to that of nitrocellulose. The wide zone was prepared by printing multiple 2 mm wide strips. We suspect that the accelerated wicking is an artifact of the BioDot printing process. The photograph in Figure 3 suggests corrugations corresponding to the contact zones between parallel strips.

The PCC2 slope in Figure 3 was  $1.22 \text{ mm/s}^{0.5}$ , which is a little less than  $1.46 \text{ mm/s}^{0.5}$ , the value in Table 2. Going from the PCC2 to the PCC4 zone, there was an expansion in the device width. In this case Fu's<sup>25</sup> results with chromatography paper predict a decrease in the PCC4 wicking slope as flow through the narrow section becomes rate limiting. The PCC4 wicking slope for 2 mm wide strips was  $0.72 \text{ mm/s}^{0.5}$ , whereas the slope for the PCC4 segment in Figure 3 was only  $0.39 \text{ mm/s}^{0.5}$ . Thus, device geometry, plus the low intrinsic wicking characteristic of PCC4 medium, contribute to the very slow wicking for the PCC4 zone in Figure 3. In summary, a large range of wicking speeds can be obtained by coupling complex geometries with multiple ink types in a single device.

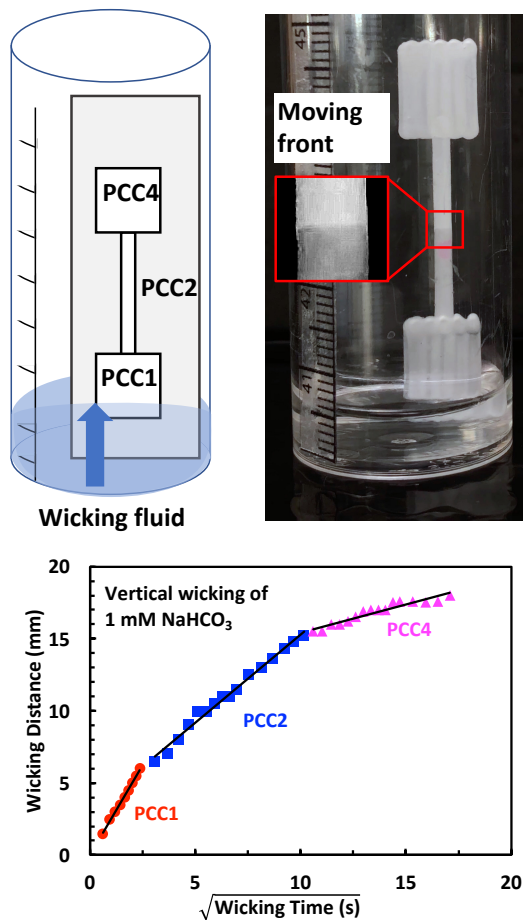


Figure 3 Illustration of a wicking experiment with a device fabricated with three media types in a single printing operation. The media are supported on a thin glass coverslip (24 mm x 60 mm) that is invisible in the photograph.

**Demonstration Devices.** The alkaline phosphatase (ALP) catalyzed reaction of BICP with NBT to give a purple precipitate was used to illustrate a color producing reaction on the PCC media. The reaction chemistry is summarized in Figure S4. The mixture of BICP + NBT was introduced by vertical wicking. Figure 4 compares the resulting PCC1 media to filter paper and nitrocellulose test strips. ALP solution (20  $\mu\text{g}/\text{mL}$ ) was printed as a strip across the three FP, NC, and PCC1 media with the BioDot dispenser at a rate of 0.2  $\mu\text{L}$  per mm at a position 10 mm beyond the beginning of the media strips. If the ALP was immobilized in the media, a blue precipitate should be deposited near the ALP zone, whereas unreacted yellow NBT will be transported up the test strip. Filter paper gave a purple/blue band near the ALP zone. The nitrocellulose performed poorly with both yellow unreacted NBT and the blue product appearing at the top, suggesting that the ALP was not

immobilized on the nitrocellulose and/or was substantially denatured after printing. The PCC1 image in Figure 4 shows that in spite of being a thin, low porosity coating (see Table 2), the PCC1 gave a purple deposit that was similar to the deposit formed on the filter paper. The colour intensity on PCC1 media was impressive because the reagent capacity of the filter paper was 200 times greater than the PCC1 media (see Table 2), putting much more BCIP + NBT reagent in the ALP zone.

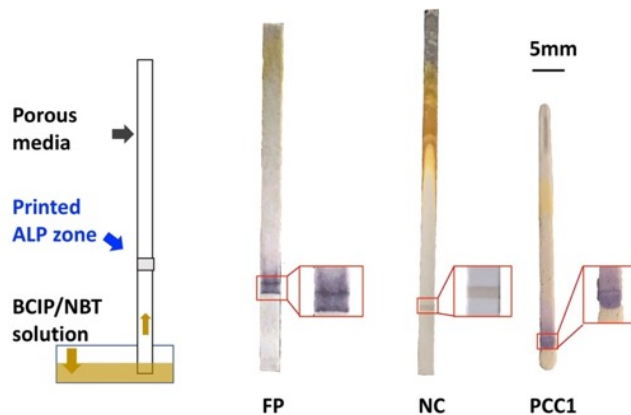


Figure 4 Images of dried media strips after performing the ALP catalyzed reaction of BCIP+NBT. The purple zones are the precipitated product of the ALP catalyzed reaction (for chemical structures see Figure S4) and the yellow color is due to unreacted BCIP.

The high affinity binding of ALP to PCC was confirmed by adsorption measurements. Figure 5 shows the adsorption isotherm with all but one point falling in the initial linear part of the isotherm. Taking PCC1 as an example, the maximum initial concentration of ALP was 20  $\mu\text{g/mL}$  whereas after adsorption, the equilibrium residual solution ALP concentration was 1  $\mu\text{g/mL}$ , indicating the surfaces bound strongly to ALP, but were not saturated with adsorbed ALP when using this initial ALP concentration.

The activities of PCC1-bound ALP compared to ALP solutions of the same concentration were measured with the p-nitrophenol phosphate assay (chemistry shown in Figure S2) and activity, relative to the equivalent ALP solution, was  $94 \pm 4\%$ . We can therefore conclude that adsorption of ALP on PCC surfaces did not denature the enzyme.

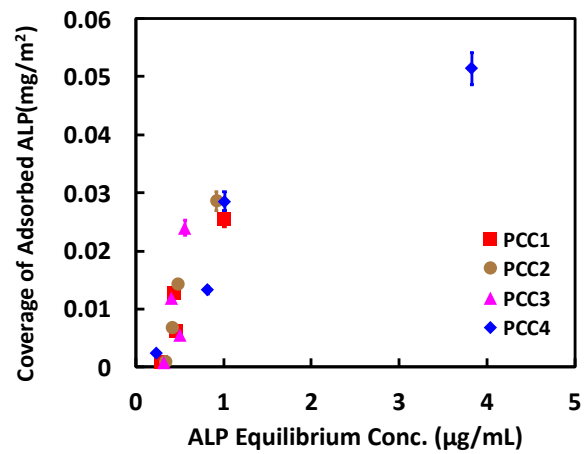


Figure 5      The adsorption of ALP in DEA buffer onto four PCC samples. The error bars depict the standard deviation of triplicate measurements.

**PCC-Immobilized ALP.** The ability of PCC to immobilize ALP with little loss in activity suggested that instead of spotting ALP solution on media, the enzyme could be better fixed in place by spotting or printing a dispersion of PCC-immobilized ALP. Figure 6 shows examples of the ALP color generation reaction when the ALP zone was obtained by printing ALP coated PCC3 (with no binder). Comparing the images in Figure 6 with the corresponding images in Figure 4, reveals the purple zones were more intense when the ALP zones were printed with PCC-treated ALP. Presumably the ALP was better immobilized when pre-adsorbed on PCC3. Also, the PCC-bound ALP should be more concentrated near the media surfaces compared to printing an ALP solution.

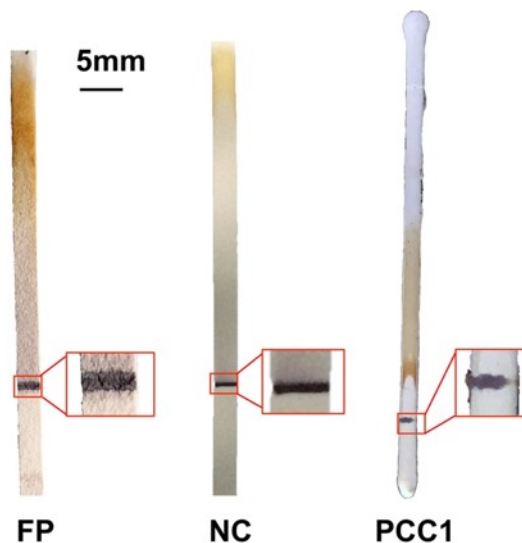


Figure 6      The ALP assay on FP, NC and PCC1 media. ALP was pre-adsorbed onto PCC3 particles dispersed in buffer (no latex binder). The PCC3-ALP dispersion was printed across the FP, NC and PCC1 media strips to create the ALP zones.

## Discussion

The ultimate goal of our research is to develop printed lateral flow media as a technology platform that can be integrated into the continuous, automated manufacture of lateral flow devices. Mixtures of commercial, colloidal PCC and latex binders gave inks that dried to form reproducible porous media whose wicking properties depended upon the colloidal PCC particle packing characteristics which, in turn, were determined by the shapes of the particles.

PCC is a particularly attractive material for biosensor applications because PCC materials form a family of synthetic, uniform, calcium carbonate products widely

available because of their widespread use, including as paper fillers and food additives. Comparing PCC with FP and NC, PCC surfaces are negatively charged<sup>26</sup> as are FP<sup>27</sup> and NC.<sup>28</sup> Published surface energies of calcium carbonate span a wide range (e.g. 28<sup>29</sup> to 45<sup>30</sup> mJ/m<sup>2</sup>) which suggests the PCC media surface energies could be close to nitrocellulose, 38 mJ/m<sup>2</sup><sup>22</sup>, but less than cellulose (50<sup>31</sup>, 59 mJ/m<sup>2</sup><sup>20</sup>). Calcium carbonate has two limitations as a porous medium for lateral flow: 1) calcium carbonate dissolves under acidic conditions, limiting applications to pH values above 7; and, 2) phosphate ions interact strongly with calcium carbonate. For assays requiring acidic conditions or phosphate buffers, printed porous media based upon silica, titanium dioxide or surface coated PCC<sup>32</sup> may be more appropriate.

Our printed media were prepared with a XYZ3060 Dispense Platform (BioDot Inc.), an excellent device for laboratory prototyping. Figure 1 shows the BioDot dispensing the PCC/binder suspension through a needle onto a moving glass surface. It is debatable as whether or not this was a printing process. As printable media move towards commercialization, we anticipate more conventional printing processes, such as screen, gravure, or flexography, could be used to manufacture complex shapes, with two or more inks giving variable wicking zones. Ultimately 3D printing could provide Z-directional control of media properties.

***Towards Biosensor Prototypes.*** Herein we have shown that reproducible media spanning a range of lateral flow characteristics can be printed with PCC inks giving flat wicking fronts and good color presentation. The capability of using multiple inks giving multiple wicking rates in a single device is particularly promising. On the other hand, a number of issues have to be resolved or optimized before printed media are viable for lateral flow sensors. These issues include blocking, bioconjugation, printable wicking pads, and mechanical strength optimization. These are now briefly discussed.

There is much literature describing the binding interactions of amino acids, proteins and DNA<sup>33,34</sup> to calcium carbonate. Furthermore, the PCC surface characteristics and our ALP adsorption studies suggest that many biomacromolecules and reagents will display nonspecific physical binding to PCC. Non-specific adsorption is also an issue with nitrocellulose and cellulose. Blocking strategies will have to be developed for PCC media. One interesting possibility is to adsorb blocking agents onto the PCC surfaces before printing the media. This could facilitate varying the presence or nature of the blocking spatially along the sensor.

The bioconjugation chemistries used to fix reagents to nitrocellulose or cellulose are unlikely to be suitable for PCC or other inorganic surfaces. Other approaches do exist. For example, calcium carbonate treatment with titanium chloride complexes with acrylamide or with 6-aminohexyl phosphate have been used for bioconjugation.<sup>35</sup>

Lateral flow devices often have highly porous sample addition pads and wicking pads to drive flow. The goal of a completely printable biosensor requires that such zones should also be printable. Thus, printable hydrogel or high void fraction printable porous media need to be developed in order to produce a fully printed LFD.

Finally, filter paper and nitrocellulose membranes are robust. Our printed porous media supported on rigid glass were sufficiently strengthened with binder to perform our experiments. However, stronger PCC media may be required if the supporting material is a flexible film. If necessary, we propose that stronger PCC media can be achieved by optimizing the binder type and content.

## **Conclusions**

To the best of our knowledge this work is the first example of a printed porous medium targeting use in lateral flow devices. Our results show that effective lateral flow media can be printed using a suspension of calcium carbonate particles and a latex binder, and that the lateral flow characteristics of the printed media can be varied within a specific device by using different types of calcium carbonate particles in different zones of the device. The final printed media are thin ( $\sim 20 \mu\text{m}$ ) layers that can strongly adsorb proteins such as ALP, and the adsorbed protein retains high activity to give strong color signals, while using less reagent compared to conventional paper or nitrocellulose media. Finally, we demonstrate that PCC can act as carrier particles for bioactive proteins (ALP), giving enhanced immobilization when spotted or printed on porous media, with no loss in activity. Taken together, this initial proof-of-concept work lays the foundation for the development of a range of biosensor prototypes, although significant work remains to address issues such as non-specific binding, bioconjugation and the currently limited operational pH range. Work in these areas will be reported in future manuscripts.

## **Acknowledgements**

The authors thank Chris Butcher (Canadian Center for Electron Microscopy, McMaster University) and Marcia Reid (McMaster Health Sciences) for sample preparation and training, and Prof. A. Kitai for access to the stylus profilometer. We thank Dr. Mehdi Keramane for helping with the printing experiments and Dr. Xiaogang Li for help with the profilometer experiments. Dr. Nigel Saunders and Dr. Philip Jones are acknowledged for useful discussions. The authors also acknowledge the Natural Sciences and Engineering Research Council of Canada for funding through the *SENTINEL* Bioactive Paper Network. We also thank the Canadian Foundation for Innovation and the Ontario Ministry of Research and Innovation for Infrastructure funding to the Biointerfaces Institute. YL acknowledges funding from the China Scholarship Council (CSC). JDB holds the

Canada Research Chair in Point-of-Care Diagnostics. RP holds the Canada Research Chair in Interfacial Technologies. Finally, we are delighted to contribute this special issue in honour of the fabulous Professor Mohamed El-Aasser.

## Supporting Information

Table S1 Some properties of the liquid PCC inks (PCCs + latex)

Inks	Surface tension (mN/m)	Viscosity (mPa·s)
PCC1	43±0.2	7.5±0.5
PCC2	47±0.1	8.4±0.4
PCC3	42±0.1	6.5±0.6
PCC4	45±0.1	9.0±0.7

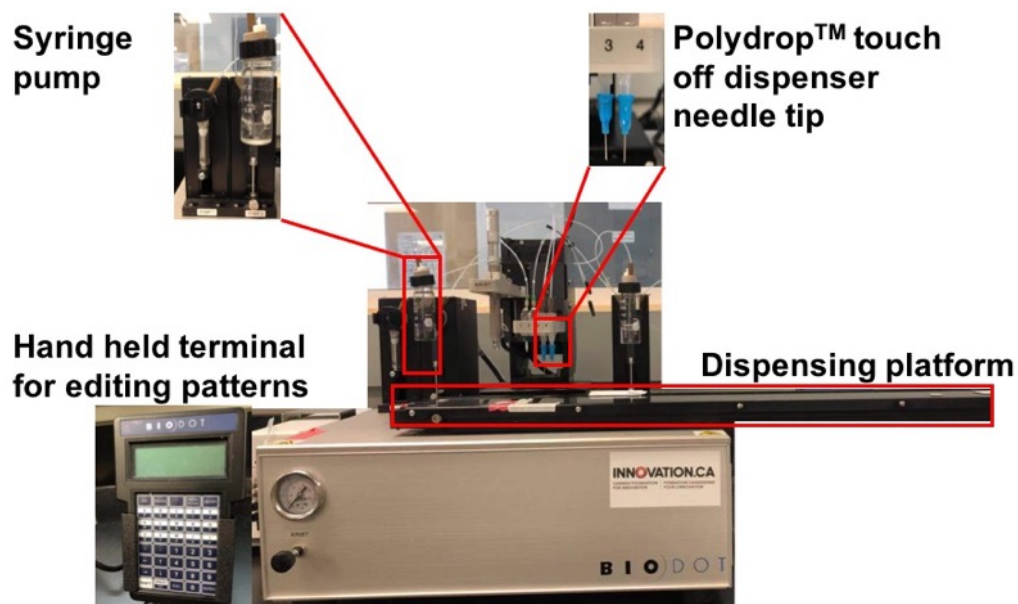


Figure S1      Photographs of the XYZ3060 Dispense Platform, Biodot Inc.

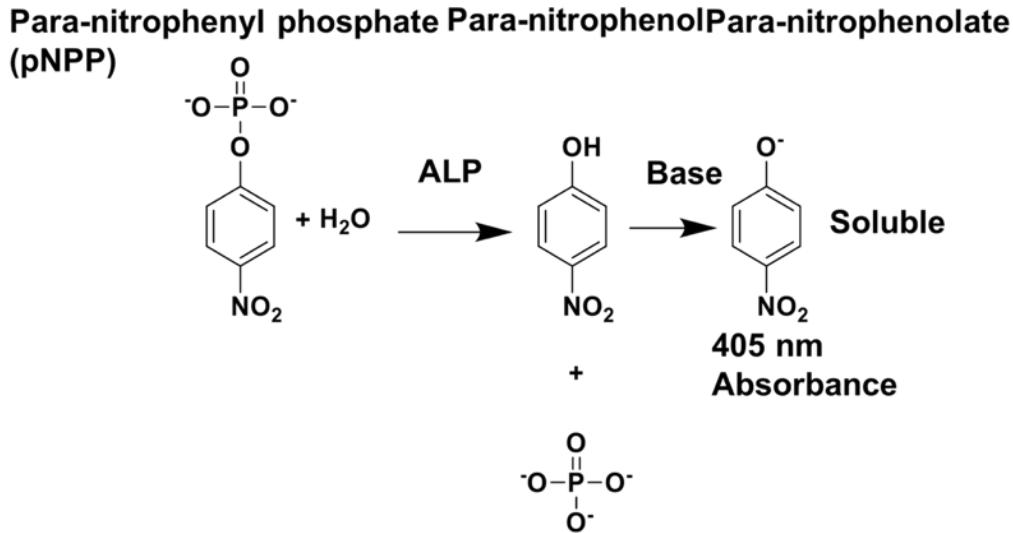


Figure S2 The p-nitrophenol phosphate assay for measuring the relative concentrations of active ALP

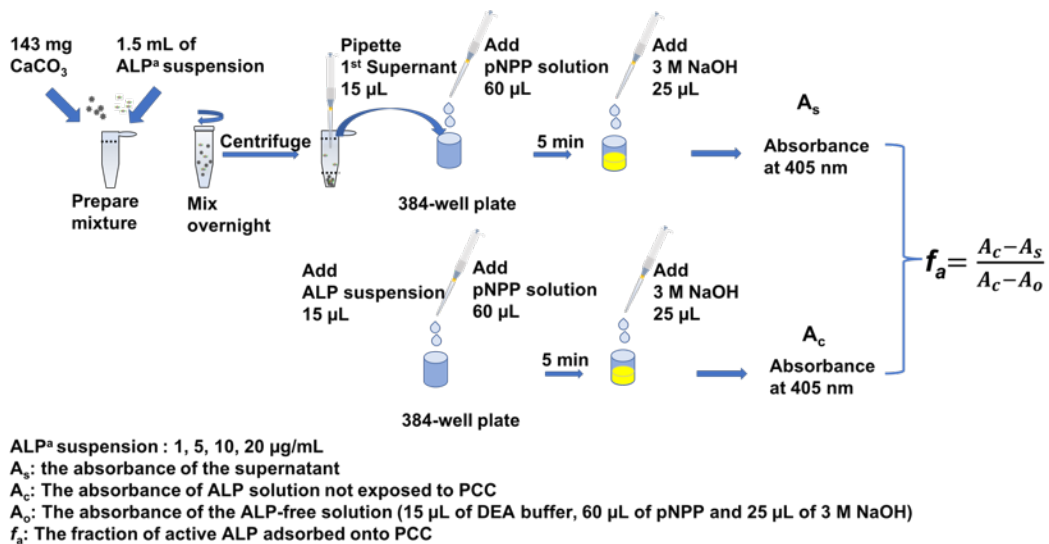


Figure S3 A schematic summary of the p-nitrophenol phosphate determination of ALP.

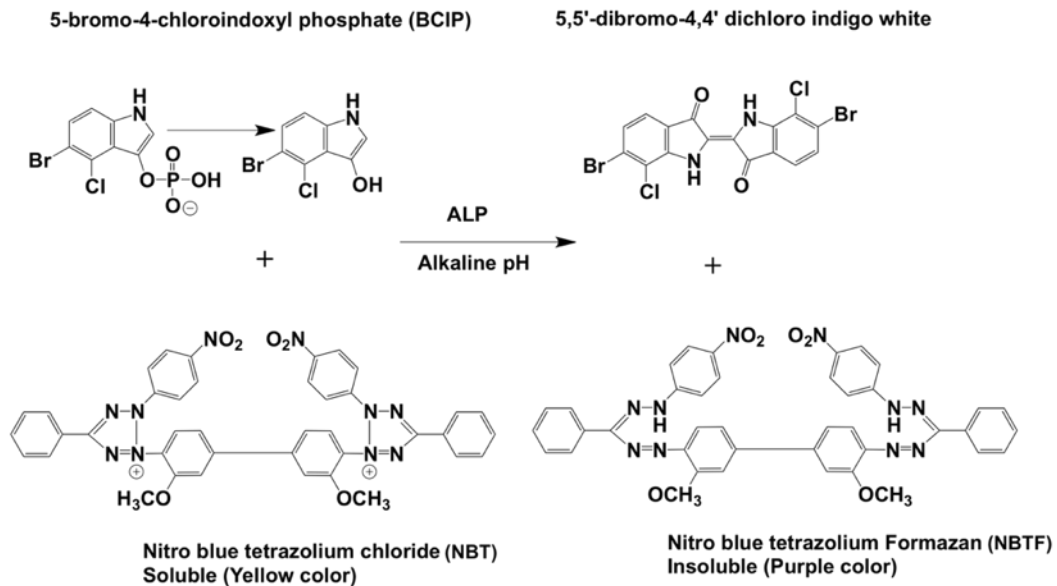


Figure S4 The ALP catalyzed reaction of BICP with NBT to give a purple precipitate (i.e. the ALP assay). Note NBT is yellow.

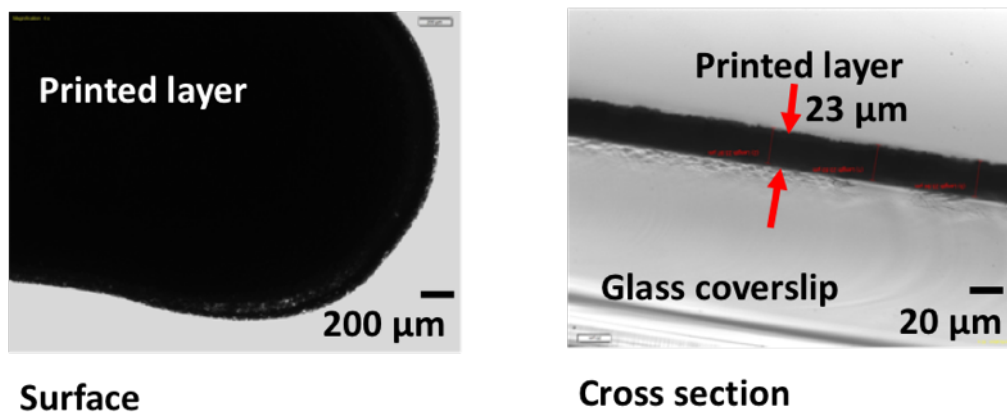


Figure S5 Left - top view, transmission optical micrograph of the starting end of the media sensor. Right - optical micrograph of media cross section.

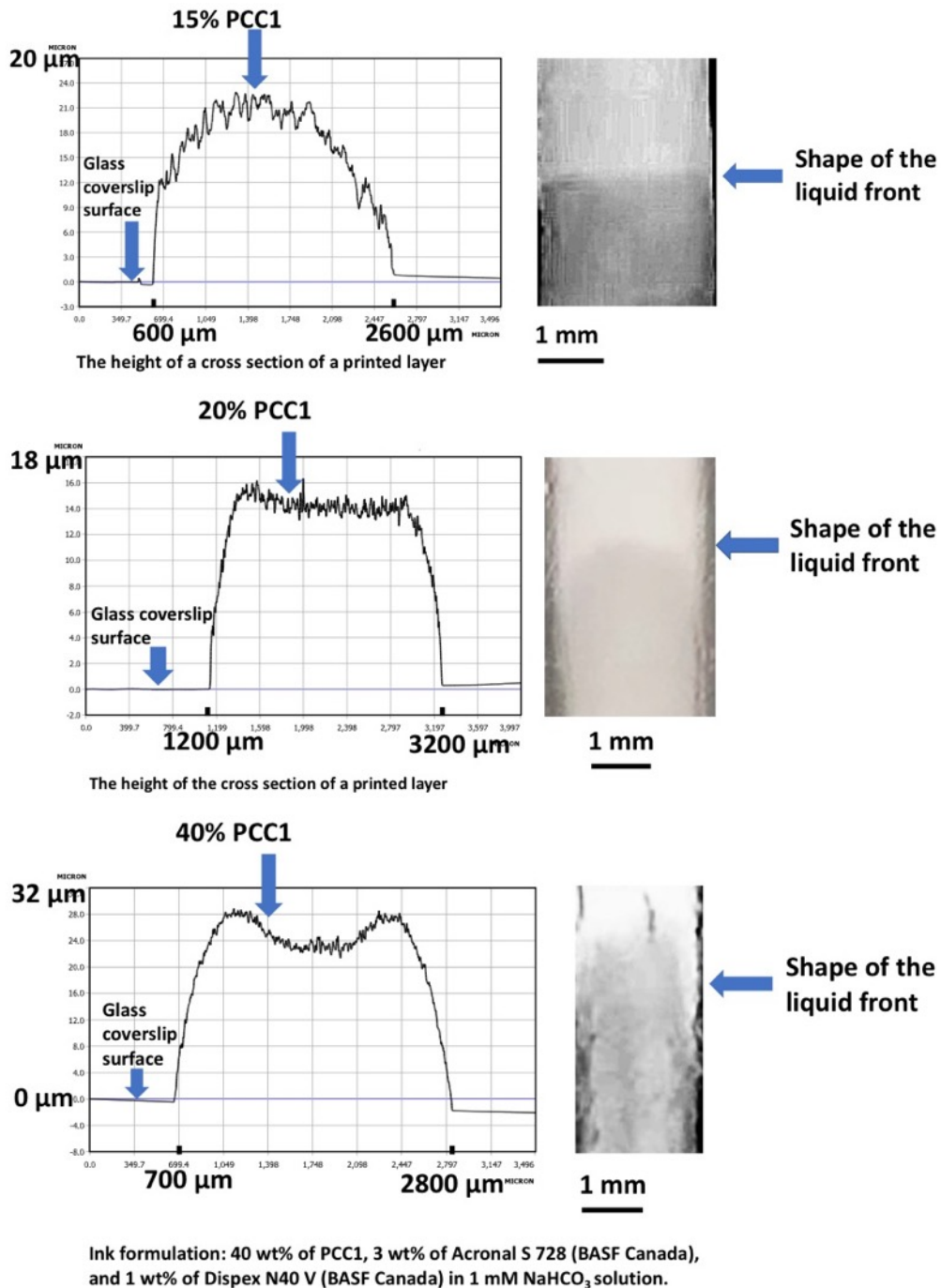


Figure S6 The influence of ink solids contents on profile shape and wicking behaviors.

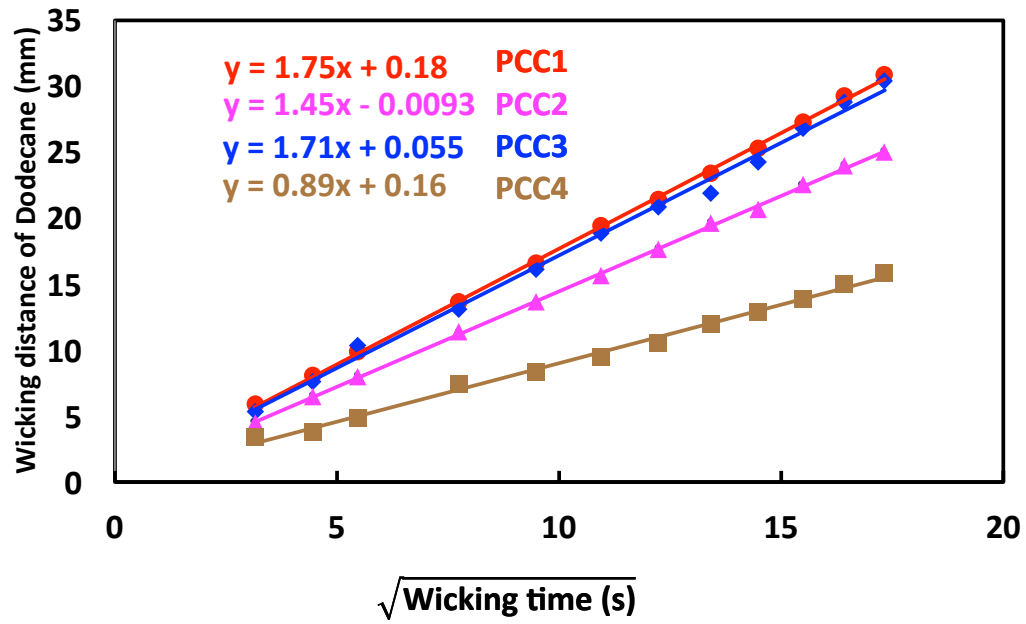


Figure S7      Dodecane wicking results for the four PCC-based media.

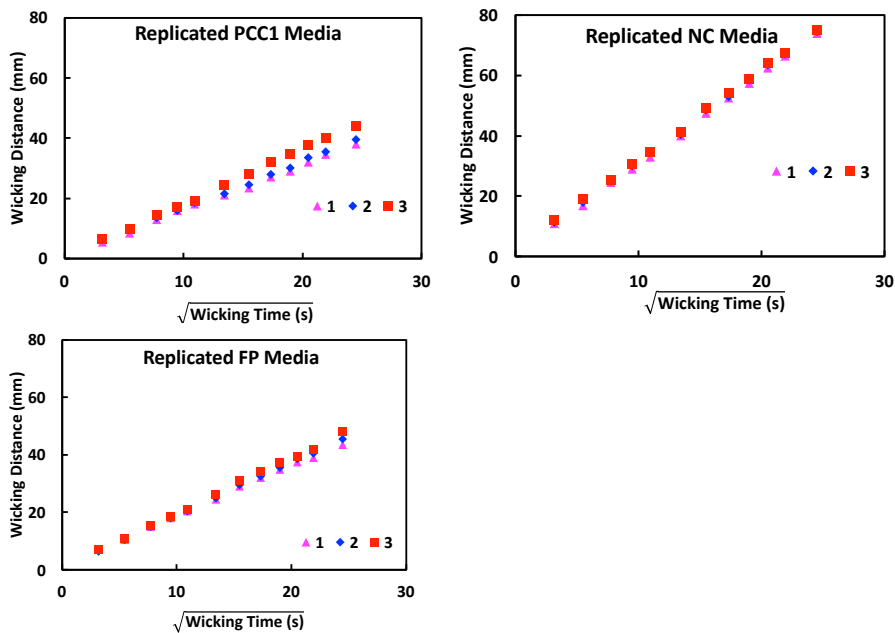
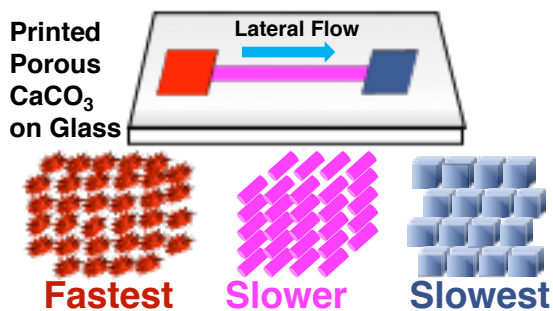


Figure S8 Illustrating the reproducibility of the printable media in comparison with FP and NC porous membranes.

## Index Graphic



## References

- (1) Yager, P.; Domingo, G. J.; Gerdes, J. Point-of-Care Diagnostics for Global Health. *Annu. Rev. Biomed. Eng.* **2008**, *10*, 107-144. <https://doi.org/10.1146/annurev.bioeng.10.061807.160524>
- (2) Yamada, K.; Shibata, H.; Suzuki, K.; Citterio, D. Toward Practical Application of Paper-Based Microfluidics for Medical Diagnostics: State-of-the-Art and Challenges. *Lab Chip* **2017**, *17*, 1206-1249. <https://doi.org/10.1039/C6LC01577H>
- (3) Tonkinson, J. L.; Stillman, B. A. Nitrocellulose: A Tried and True Polymer Finds Utility as a Post-Genomic Substrate. *Frontiers in Bioscience* **2002**, *7*, c1-12.

- (4) Fridley, G. E.; Holstein, C. A.; Oza, S. B.; Yager, P. The Evolution of Nitrocellulose as a Material for Bioassays. *MRS Bulletin* **2013**, 38, 326-330. <https://doi.org/10.1557/mrs.2013.60>
- (5) Pelton, R. Bioactive Paper - a Low Cost Platform for Diagnostics. *Trends Anal. Chem.* **2009**, 28, 925-942. <https://doi.org/10.1016/j.trac.2009.05.005>
- (6) Su, J.; Al-Tamimi, M.; Garnier, G. Engineering Paper as a Substrate for Blood Typing Bio-Diagnostics. *Cellulose* **2012**, 1-10. <https://doi.org/10.1007/s10570-012-9748-7>
- (7) Millipore, Rapid Lateral Flow Test Strips Considerations for Product Development. In *Lit. No. TB500EN00EM Rev. C 12/13*, 2013.
- (8) Niskanen, K., *Paper Physics*. Fapet Oy: Helsinki, 1998; Vol. 16, p 324.
- (9) Jahanshahi-Anbuhi, S.; Chavan, P.; Sicard, C.; Leung, V.; Hossain, S. M. Z.; Pelton, R.; Brennan, J. D.; Filipe, C. D. M. Creating Fast Flow Channels in Paper Fluidic Devices to Control Timing of Sequential Reactions. *Lab Chip* **2012**, 12, 5079-5085. <https://doi.org/10.1039/C2LC41005B>
- (10) Carrilho, E.; Martinez, A. W.; Whitesides, G. M. Understanding Wax Printing: A Simple Micropatterning Process for Paper-Based Microfluidics. *Anal. Chem.* **2009**, 81, 7091-7095. <https://doi.org/10.1021/ac901071p>
- (11) Abe, K.; Kotera, K.; Suzuki, K.; Citterio, D. Inkjet-Printed Paperfluidic Immuno-Chemical Sensing Device. *Anal. Bioanal. Chem.* **2010**, 398, 885-893. <https://doi.org/10.1007/s00216-010-4011-2>
- (12) Li, X.; Tian, J.; Shen, W. Progress in Patterned Paper Sizing for Fabrication of Paper-Based Microfluidic Sensors. *Cellulose* **2010**, 17, 649-659. <https://doi.org/10.1007/s10570-010-9401-2>
- (13) Olkkonen, J.; Lehtinen, K.; Erho, T. Flexographically Printed Fluidic Structures in Paper. *Anal. Chem.* **2010**, 82, 10246–10250. <https://doi.org/10.1021/ac1027066>
- (14) Dungchai, W.; Chailapakul, O.; Henry, C. S. A Low-Cost, Simple, and Rapid Fabrication Method for Paper-Based Microfluidics Using Wax Screen-Printing. *Analyst* **2011**, 136, 77-82. <https://doi.org/10.1039/c0an00406e>
- (15) Martinez, A. W.; Phillips, S. T.; Whitesides, G. M. Three-Dimensional Microfluidic Devices Fabricated in Layered Paper and Tape. *Proc. Natl. Acad. Sci. U. S. A.* **2008**, 105, 19606-19611. <https://doi.org/10.1073/pnas.0810903105>
- (16) Jutila, E.; Koivunen, R.; Kiiski, I.; Bollström, R.; Sikanen, T.; Gane, P. Microfluidic Lateral Flow Cytochrome P450 Assay on a Novel Printed Functionalized Calcium Carbonate-Based Platform for Rapid Screening of Human Xenobiotic Metabolism. *Advanced Functional Materials* **2018**, 28, 1802793. <https://doi.org/10.1002/adfm.201802793>
- (17) Koivunen, R.; Jutila, E.; Bollström, R.; Gane, P. Hydrophobic Patterning of Functional Porous Pigment Coatings by Inkjet Printing. *Microfluidics Nanofluidics* **2016**, 20, 83. <https://doi.org/10.1007/s10404-016-1747-9>
- (18) Jutila, E.; Koivunen, R.; Bollström, R.; Gane, P. Wicking and Chromatographic Properties of Highly Porous Functionalised Calcium Carbonate Coatings Custom-Designed for Microfluidic Devices. *Journal of Micromechanics and Microengineering* **2019**, 29, 055004. <https://doi.org/10.1088/1361-6439/ab0941>
- (19) Washburn, E. W. The Dynamics of Capillary Flow. *Physical Review* **1921**, 17, 273-283. <https://doi.org/10.1103/PhysRev.17.273>
- (20) Forsstrom, J.; Eriksson, M.; Wagberg, L. A New Technique for Evaluating Ink-Cellulose Interactions: Initial Studies of the Influence of Surface Energy and Surface

- Roughness. *J. Adhes. Sci. Technol.* **2005**, *19*, 783-798. <https://doi.org/10.1163/1568561054867846>
- (21) Millipore, Hi-Flow™ Plus Membranes and Surewick® Pad Materials. In *Lit. No. PB1267EN00*, 2008
- (22) Van Oss, C. J.; Good, R. J.; Chaudhury, M. K. Mechanism of DNA (Southern) and Protein (Western) Blotting on Cellulose Nitrate and Other Membranes. *J. Chromatogr. A* **1987**, *391*, 53-65. [https://doi.org/10.1016/S0021-9673\(01\)94304-3](https://doi.org/10.1016/S0021-9673(01)94304-3)
- (23) Zhdanov, S. A.; Starov, V. M.; Sobolev, V. D.; Velarde, M. G. Spreading of Aqueous SDS Solutions over Nitrocellulose Membranes. *J. Colloid Interface Sci.* **2003**, *264*, 481-489. [https://doi.org/10.1016/S0021-9797\(03\)00520-4](https://doi.org/10.1016/S0021-9797(03)00520-4)
- (24) De Gennes, P. G.; Brochard-Wyart, F.; Quéré, D., *Capillarity and Wetting Phenomena: Drops, Bubbles, Pearls, Waves*. Springer Verlag: New York, 2004.
- (25) Fu, E. L.; Ramsey, S.; Kauffman, P.; Lutz, B.; Yager, P. Transport in Two-Dimensional Paper Networks. *Microfluid. Nanofluid.* **2011**, *10*, 29-35. <https://doi.org/10.1007/s10404-010-0643-y>
- (26) Thompson, D. W.; Pownall, P. G. Surface Electrical-Properties of Calcite. *J. Colloid Interface Sci.* **1989**, *131*, 74-82. [https://doi.org/10.1016/0021-9797\(89\)90147-1](https://doi.org/10.1016/0021-9797(89)90147-1)
- (27) Goring, D. a. I.; Mason, S. G. Electrokinetic Properties of Cellulose Fibers: II. Zeta-Potential Measurements by the Stream-Compression Method. *Can. J. Res.* **1950**, *28b*, 323-338. <https://doi.org/10.1139/cjr50b-040>
- (28) Low, S. C.; Shaimi, R.; Thandaithabany, Y.; Lim, J. K.; Ahmad, A. L.; Ismail, A. Electrophoretic Interactions between Nitrocellulose Membranes and Proteins: Biointerface Analysis and Protein Adhesion Properties. *Colloids and Surfaces B: Biointerfaces* **2013**, *110*, 248-253. <https://doi.org/10.1016/j.colsurfb.2013.05.001>
- (29) Ulusoy, U.; Hiçyılmaz, C.; Yekeler, M. Role of Shape Properties of Calcite and Barite Particles on Apparent Hydrophobicity. *Chemical Engineering and Processing: Process Intensification* **2004**, *43*, 1047-1053. <https://doi.org/10.1016/j.cep.2003.10.003>
- (30) Bargir, S.; Dunn, S.; Jefferson, B.; Macadam, J.; Parsons, S. The Use of Contact Angle Measurements to Estimate the Adhesion Propensity of Calcium Carbonate to Solid Substrates in Water. *Appl. Surf. Sci.* **2009**, *255*, 4873-4879. <https://doi.org/10.1016/j.apsusc.2008.12.017>
- (31) Dourado, F.; Gama, F. M.; Chibowski, E.; Mota, M. Characterization of Cellulose Surface Free Energy. *J. Adhes. Sci. Technol.* **1998**, *12*, 1081-1090. <https://doi.org/10.1163/156856198X00740>
- (32) Bollström, R.; Jutila, E.; Koivunen, R.; Ridgway, C.; Gane, P. In *Porous Liquid Driving Channels on Coated Paper for Use in Printed Microfluidic Diagnostics*, PaperCon, Atlanta, April 19-22; TAPPI Press: 2015; pp 73-83.
- (33) Bezanilla, M.; Manne, S.; Laney, D. E.; Lyubchenko, Y. L.; Hansma, H. G. Adsorption of DNA to Mica, Silylated Mica, and Minerals: Characterization by Atomic-Force Microscopy. *Langmuir* **1995**, *11*, 655-659. <https://doi.org/10.1021/la00002a050>
- (34) Lukeman, P. S.; Stevenson, M. L.; Seeman, N. C. Morphology Change of Calcium Carbonate in the Presence of Polynucleotides. *Cryst. Growth Des.* **2008**, *8*, 1200-1202. <https://doi.org/10.1021/cg700656r>
- (35) Denisov, N. N.; Chitchevlova, L. A.; Sekatskii, S. K.; Diefler, G. Covalent Attachment of Proteins to Calcite Surface for the Single Molecule Experiments. *Colloids Surf., B* **2008**, *63*, 282-286. <https://doi.org/10.1016/j.colsurfb.2007.12.011>

## *Chapter 6*

### **My Contributions**

---

Many of the traditional lateral flow biosensor manufacturing processes are manual: membranes must be cut from rolls, treated, and assembled using a step-by-step process. Thus, there is a pressing need for a more accelerated production method. To address this need, this research has developed the first lateral flow biosensor to use printable porous media as a substrate. Furthermore, this work also investigated and elucidated the clogging mechanisms that tend to arise when attempting to print expensive reagents onto substrates. Overall, this work's major contribution is the development of a promising automated production process for lateral flow biosensors:

1. A rapid process for screening potential pigments and polymer binders for printing was developed. This process included: (1) using a robot dispenser to prepare all formulations; (2) coating different inks on wax-patterned and plasma treated films in parallel; and (3) measuring the wicking distance in all formulations. Based on the coating coverage results from nine hundred samples, inks with a pigment content of at least 12 wt% were found to be able to fully cover the surface. In addition, the wicking experiment results showed that polyvinyl alcohol's swelling ability allowed it to reduce the liquid wicking distance to a greater degree than the non-swelling latex binders.
2. This research is the first to document the use of printable porous media as substrates in lateral flow devices. The porous media can be printed using inks consisting of different types of calcium carbonate particles and a latex binder, which provides various lateral flow characteristics. Furthermore, complex patterns can be obtained through direct printing without printing barriers. The final printed media were thin ( $\sim 20 \mu\text{m}$ ) layers that were able to effectively adsorb proteins such as alkaline phosphatase (ALP). Meanwhile, compared to conventional membranes, the adsorbed proteins retained a high level of activity. This research also demonstrates that precipitated calcium carbonates can act as carrier particles for bioactive

proteins (ALP). This provides enhanced immobilization when spotted or printed onto porous media, while ensuring no loss in activity.

3. This research also provides the first demonstration that colloidally stable ink particles can induce air clogging in inkjet printheads. This finding was supported by the novel observation that clogging did not occur when ink was pumped using a steady flow but did occur when normal piezoelectric jetting. These nanoparticles, which varied in terms of particle size, surface charge, and softness, were regarded as models for many biomaterials. During the inkjet printing process, hydrophobic cationic polystyrene nanoparticles adhered on printhead surfaces as a sub-monolayer, which caused and promoted air entrainment within interior printhead surfaces. As a result, the trapped air bubbles clogged the nozzles. Thus, alternate surface chemistries for the printhead and ink particle surfaces may be required to print hydrophobic ink materials.

4. Finally, this research identified the conditions under which silica sol inks can be printed with minimal inkjet clogging. Silica sols are reactive under acidic conditions, which causes the formation of multilayer deposits on the internal surfaces of the printhead that continue to grow throughout with printing period. As this work showed, the vibration of the piezoelectric layer causes the deposited silica sols to detach from the surface, which leads to nozzle clogging when the size of silica particles exceeds the size of the nozzle. To mitigate this issue, an optimal printing pH of 3.1 is recommended for silica sol, as this pH level should enable reduced nozzle clogging while still allowing enzymes to be immobilized onto the media in the lateral flow biosensor.